Study of radiative properties : application to fast determination of temperature and iron concentration for MAG-P Arc (Ar-CO2-Fe mixtures) and to estimation of photobiological hazards for argon GTAW Arc

Fei Wang

Université Fédérale
Toulouse Midi-Pyrénées

THÈSE

En vue de l'obtention du

DOCTORAT DE L'UNIVERSITÉ DE TOULOUSE

Délivré par :

Université Toulouse 3 Paul Sabatier (UT3 Paul Sabatier)

Cotutelle internationale avec l'Université de Tianjin (Chine)

Présentée et soutenue par :
Fei Wang
le jeudi 21 juin 2018

Titre :

Study of Radiative Properties: Application to Fast determination of Temperature and Iron concentration for MAG-P Arc (Ar-CO2-Fe mixtures) and to Estimation of Photobiological Hazards for argon GTAW Arc

---

École doctorale et discipline ou spécialité :
ED GEET : Ingénierie des PLASMAS

Unité de recherche :
LAPLACE, UMR 5213

Directeur/trice(s) de Thèse :

Yann CRESSAULT, Maître de Conférences, Université Paul Sabatier Toulouse
Huan LI, Professeur, Université de Tianjin, Chine

Jury :
Jean-Marc BAUCHIRE, Professeur, Université d'Orléans, rapporteur
Yuntao LI , Maître de Conférence, Université Technologique de Tianjin, Chine, rapporteur
Philippe TEULET, Professeur, Université Paul Sabatier Toulouse, examinateur
Zhentai ZHENG, Maître de Conférences, Université Technologique de Hebei, Chine, examinateur
Yann CRESSAULT, Maître de Conférences, Université Paul Sabatier Toulouse
Huan LI, Professeur, Université de Tianjin, Chine

AUTOR: Fei WANG

TITLE: Study of Radiative Properties: Application to Fast Determination of Temperature and Iron Concentration for MAG-P Arc (Ar-CO2-Fe mixtures) and to Evaluation of Photobiological Hazards for Argon GTAW Arc.

THESIS DIRECTORS: Yann CRESSAULT, Philippe TEULET, Huan LI

LABORATORY: LAPLACE UMR 5213 CNRS, Université Paul Sabatier, 118 route de Narbonne, Bât. 3R3, 31062 Toulouse Cedex 9

Summary:

This PhD thesis introduces a method that allows the fast determination of temperature and iron concentration for MAG-P Arc. The MAG-P Arc is in fact [Ar-CO_2]-Fe mixtures, with a constant molar ratio between Ar and CO_2 [82%Ar-18%CO_2]. In a second time, this thesis presents a study of the optical radiation associated to photobiological hazards for argon GTAW Arc.

In chapter 1, the background and motivation of this work is introduced. The previous works published in this field are reviewed.

In chapter 2, the equilibrium compositions are calculated firstly using the minimization of Gibbs free energy. Then the radiative properties of [Ar-CO_2]-Fe plasmas are obtained in the frame of the net emission coefficient (NEC) approach, using the accurate “line by line” method. All significant radiative contribution mechanisms are taken into account in the calculation. This study will constitute groundwork to build the diagnostic method that allows determination of temperature and iron concentration profiles in welding arc.

In chapter 3, spectroscopic investigation of the LTE hypothesis across the MAG-P Arc is made. Excitation temperature is obtained with Boltzmann plot method while iron and argon lines Stark broadening measurements are used to get electron temperature and electron density. LTE hypothesis validity across the arc is discussed considering the agreement between the two temperatures, the electron density and iron content. Results show supporting evidence for the main part of the plasma, along radial and axial directions. Discrepancies occur only at the fringe of the arc, where the two temperatures differ by more than 2000 K.

In chapter 4, a method allowing a fast determination of space- and time-resolved plasma temperature and iron concentration in MAG arcs during the high-current phase is introduced. This method consists in measuring the plasma spectral radiation of the arc with iron vapours using a high-speed camera filtered by narrow band filters in the spectral intervals of 570-590 nm and 606-627 nm respectively; calculating theoretically the dependence of the absolute

emissivity $\varepsilon_{570\text{-}590\ nm}$ and relative emissivity $\varepsilon_{570\text{-}590\ nm}/\varepsilon_{607\text{-}627\ nm}$ versus the plasma temperature and the iron concentration. This method has also been validated for a layer of plasma by adopting other existing diagnostics such as Stark broadening, which demonstrates the effectiveness of this new method.

In chapter 5, a theoretical investigation of the UV (180-400 nm), UVA (315-400 nm) and blue light (300-700 nm) radiation associated with the photobiological hazards to workers for argon GTAW arcs is presented. The radiative properties of argon plasma are calculated for the three spectral regions, and a two-dimensional model of a GTAW arc is then developed to determine the local emissions in the arc, the total radiation escaping from the arc and corresponding effective irradiances. This study clearly supports the importance of undertaking an effective protection strategy for workers, particularly for skin and eyes, in the welding environment.

Finally, a general conclusion is given in chapter 6.

AUTEUR: Fei WANG

TITRE: Etude des propriétés radiatives: application à la determination rapide de la temperature et de la concentration de fer pour un plasma d'arc MAG (mélanges Ar-CO_2-Fe) et estimation des risques photobiologiques pour un arc GTAW dans l'argon.

DIRECTEURS DE THESE: Yann CRESSAULT, Philippe TEULET, Huan LI

LABORATOIRE: LAPLACE UMR 5213 CNRS, Université Paul Sabatier, 118 route de Narbonne, Bât. 3R3, 31062 Toulouse Cedex 9

Résumé:

La première partie de ce travail présente une nouvelle méthode qui permet de déterminer rapidement la température et la concentration en fer d'un plasma d'arc MAG [82%Ar-18%CO_2] utilisé dans la technologie de soudage par plasma. La seconde partie s'intéresse au rayonnement d'un plasma d'argon utilisé dans la technologie soudage GTAW et pouvant conduire à des dangers photobiologiques.

Dans le chapitre 1, le contexte et la motivation de ce travail sont présentés. Les travaux déjà effectués et publiés dans ces deux axes scientifiques sont passés en revue.

Dans le chapitre 2, les compositions à l'équilibre sont calculées par la méthode de la minimisation de l'énergie libre de Gibbs. Les densités et fonctions de partitions obtenues pour chaque espèce présente dans le plasma sont ensuite utilisées pour déterminer les pertes radiatives des plasmas [Ar-CO_2]-Fe via la méthode du coefficient d'émission net (CEN). Cette estimation des pertes ne peut se faire sans le calcul préalable du coefficient d'absorption spectral obtenu par la méthode « raie par raie ». Tous les mécanismes radiatifs prédominants dans le plasma ont été pris en compte: continua atomique et moléculaire, raies atomiques et moléculaires. Cette partie constitue la base de cette étude sur laquelle se fonde la nouvelle méthode de diagnostic destinée à déterminer à la fois la température et la concentration en fer d'un plasma d'arc de soudage.

Le chapitre 3 est dédié à l'étude expérimentale d'un plasma d'arc MAG composée d'une analyse spectroscopique permettant de remonter au profil de température et d'une vérification de l'Équilibre Thermodynamique Local. La température d'excitation est obtenue par la méthode de Boltzmann tandis que la mesure d'élargissements Stark pour les raies de fer et d'argon permet de remonter à la température et la densité des électrons. La validité de l'hypothèse ETL est réalisée par comparaisons des profils de températures, des densités électroniques et des concentrations de fer obtenus. Les résultats conduisent à la présence d'un ETL dans le cœur du plasma, et le long des directions radiale et axiale. Les écarts à l'équilibre

se produisent seulement sur les bords de l'arc où les deux températures diffèrent de plus de 2000 K.

Au chapitre 4, nous présentons une méthode permettant de déterminer rapidement, temporellement et spatialement, à la température et la concentration en fer d'un plasma d'arc MAG pendant sa phase de haute intensité. Cette méthode consiste à mesurer le rayonnement spectral du plasma en présence de vapeur de fer à partir d'une caméra haute vitesse filtrée par des filtres à bande étroite dans les intervalles spectraux respectivement de 570-590nm et 606-627nm; intervalles déduits de l'étude théorique menée au chapitre 2 et montrant la dépendance des émissivités absolues ε(570-590nm) et relatives ε(570-590nm)/ε(607-627nm) en fonction de la température du plasma et de la concentration en fer. Les résultats de cette méthode sont validés par pour une couche de plasma par comparaison avec les valeurs déduites des autres méthodes de diagnostics tel que l'élargissement Stark, montrant l'efficacité de cette nouvelle méthode.

Le chapitre 5 présente une étude théorique des rayonnements UV (180-400nm), UVA (315-400nm) et lumière bleue (300-700nm) associée aux dangers photobiologiques pour les utilisateurs des arcs GTAW avec argon. Les propriétés radiatives du plasma d'argon sont calculées pour les trois régions spectrales, puis utilisées dans un modèle bidimensionnel d'arc de GTAW pour déterminer les émissions locales dans l'arc, le rayonnement total s'échappant de l'arc et les irradiations efficaces correspondantes. Cette étude montre clairement l'importance de mettre en place une stratégie de protection efficace pour les travailleurs, en particulier pour la peau et les yeux, dans l'environnement des applications liées au soudage par plasmas.

Une conclusion de ce travail ainsi que ses perspectives sont présentés au chapitre 6.

Contents

General introduction

Arc welding is an important industry process for joining metals. In the atmosphere of shielding gas, an electrical arc is created between two electrodes, one of which is the workpiece, i.e. the pieces of metal that are being joined. The other is a consumable electrode or tungsten electrode. The high energy flux from the arc melts a region of the workpiece, forming the weld pool. Gas metal arc welding (GMAW) and gas tungsten arc welding (GTAW) are two most widely used arc welding processes. The GMAW process uses a consumable metal wire as another electrode except the workpiece, while the GTAW process uses a refractory material (usually tungsten) that does not melt as the electrode. GMAW is also referred to as metal inert gas welding (MIG) or metal active gas (MAG) welding, depending if the shielding gas is either inert (e.g. Ar or He) or active (containing CO_2 or/and O_2). The addition of a certain proportion of active gas in argon (e.g. 82%Ar-18%CO_2 mixture) is beneficial to improve the arc stability and the mobility of molten metal[1], reason why this mixture is popular in welding of mild steel.

This thesis work has been devoted to two main subjects: (1) the introduction of a new method that allows a fast determination of space- and time-resolved plasma temperature and iron concentration in a MAG arc (Ar-CO_2-Fe mixtures); (2) the study of the optical radiation associated with photobiological hazards posed by argon GTAW arc. Obviously, the former subject has focus on GMAW (more particularly MAG welding), while the latter one on GTAW. Both of these subjects are based on the study of plasma radiative properties.

In general, the majority of studies of welding processes concern the weld quality and the influences of welding parameters on it. Main relations and mechanisms have been systematically studied in early works (see e.g. [2, 3]) and are well known. Take GMAW as an example, the melting rate is mainly dependent on current and wire diameter and to a low extent on the stick-out. The droplet transfer mode changes with increasing current from globular transfer to spray transfer and at higher current to rotating arc spray transfer. By using a pulsed current, it is possible to obtain a one drop per pulse (ODDP) mode, which is characterized by a stable, periodical and controllable metal transfer to the workpiece[4, 5]. Due to its good performance, the pulsed GMAW (GMAW-P; MIG-P or MAG-P welding) has been favoured in industry.

A smaller number of studies were aimed in the detailed determination of physics properties of GMAW arcs. Early examples are the spectroscopic study of plasma-MIG arc by Ton[6] and of argon MIG arc by Smars et al[7, 8]. However, in the last 10 years a growing number of diagnostic studies can be found together with increasing interest in modelling of GMAW arc processes. This is related to the fact that researchers realized the great influence of metal vapour in arc welding, and thermal plasmas generally.

It is well known that large amounts of metal vapour are produced at the wire electrode, droplets and the weld pool in GMAW. According to Murphy's review[9], the presence of metal vapor has major influences on arc welding. It can markedly increase the radiative emission[10, 11] and the electrical conductivity[11, 12] at low temperature with small proportions (<1% by mole). It also can change other plasma properties, such as the viscosity or the thermal conductivity, with proportions more than 20% by mole[12]. All of these effects can result in the changes of current and energy transfer to the workpiece, and thus the profile of the weld pool.

The measurements of metal vapour concentration as well as plasma temperature are vital for the study of arc welding, in part due to the major influences of metal vapour. Besides, the determination of these two parameters is helpful to deduce physical properties and to understand the physical mechanisms involved. All plasmas properties, such as thermophysical and radiative properties and transport coefficients, depend on these two parameters (see e.g. [11]). It is possible to further obtain the heat, mass and current transfer in arcs from them based on the theory of magnetohydrodynamics[1, 13]. Furthermore, the measurement of the two parameters is critical in validating the computational model.

To determine arc properties, there exists numerous experimental methods, such as Thomson scattering[14-16], Langmuir probe[17, 18] or optical emission spectroscopy which is the most commonly used method for diagnosing arc plasmas. It has been widely used to measure some steady arcs, e.g. GTAW arcs[19-22]. However, there are still many difficulties for the measurement of GMAW arcs because the arc is highly dynamic due to the fact that metal droplets are continually forming at the wire tip, then detaching and falling through the arc. As consequences, the radiative properties used for plasma diagnosis are not always available. In recent years, researchers have addressed several measurements of temperature and metal vapor concentration for

GMAW arcs[23-31], but it is still far from optimal. First, there is a large variation in the measured metal vapor concentration : Goecke et al[30] found a maximum concentration of 30%, Rouffet et al[23] up to 60%, while Valensi et al[25] measured less than 1% iron concentration. In despite of the use of different welding conditions, such a large difference is surprising and needs further studies. Moreover, the previous methods, which are based on the principle of line emission and the instruments of spectroscopy or intensified charge coupled device (ICCD), can only instantaneously record the data for one spatial position or one layer of the arc, while the arc is highly unsteady. It means that it is hard to diagnose the entire arc. Also, most of previous measurements have focused on MIG arcs, but no work for MAG arcs in pulse mode, although MAG-P welding is widely used. As a consequence, there remains a need for an alternative method that can precisely and quickly determine the temperature and the metal vapor concentration for GMAW arcs, especially for the MAG-P arc.

One purpose of this thesis is to introduce a method allowing a fast determination of plasma temperature and iron concentration in MAG-P arcs. The shielding gas of 82% Ar-18% CO_2 mixture is used due to its good performance and wide use in the welding of mild steel. Since iron vapour evaporated from the wire electrode and droplets will enter the arc, the MAG-P arc can be regarded as a mixture of [82%Ar-18%CO_2]-Fe. The method adopts a high-speed CCD camera coupled with narrow bandpass filters as a diagnostic tool and it can quickly collect the integrated radiation within a spectral interval for the entire arc. The plasma temperature and iron concentration can be deduced by comparing the measured absolute or relative local emission with the theoretical emission. In fact, similar method has been tested and validated in measuring the temperature for some plasmas with fixed components, e.g. pure Ar[32-34], Ar-H_2 and Ar-He-H_2[35] in the case of a stabilized torch or Air[36] in steady or unsteady conditions by Laboratoire Plasma et Conversion d'énergie (Laplace) laboratory and other laboratories. However, little attention has been paid to the determination of both temperature and metal vapour concentration for plasmas with unfixed component (e.g. the MAG arc).

The most critical challenge of this method is to select appropriate diagnostic spectral intervals, which require the prerequisite knowledge of radiative properties of plasmas. The radiative properties have already been reported for pure gases, binary gas mixtures or more complex mixtures containing argon, carbon dioxide or iron:

Ar[10, 37], CO_2[38], Fe[39], Ar-Fe[10], CO_2-Cu[40], Ar-H_2-Fe[41], CO_2-N_2-Cu[42]. But, there are no available data for Ar-CO_2-Fe plasmas.

Besides the arc diagnostics, this thesis has another subject: the evaluation of photobiological hazards posted by optical radiation for argon GTAW arcs. It is estimated that there are more than three million welders worldwide, and the welding arc is still the main source of occipital radiation exposure[43, 44]. In this case, the GTAW process is chosen since it is usually used manually. The radiative spectra of welding processes are extremely widened but the radiation energy is essentially transported in ultraviolet (UV), visible, and near infrared ranges. The exposure to excessive welding UV radiation can cause acute health effects: erythema (skin reddening) and photokeratitis (arc eye)[43, 44]. Chronic welding UV exposure may increase the risk of skin aging and skin cancer[43, 45]. Also, the blue light radiation is an important factor for the development of ocular diseases (e.g. retinal/corneal burn). Due to these adverse photobiological effects, the welding radiation has received much attention in occupation health and safety.

In the welding process, workers are protected from radiation by the use of welding helmets, safety spectacles and industrial clothing, welding curtain and other screening measures. However, studies have shown that welders are regularly exposed to doses of radiation that exceed the permissible exposure limit at positions that are thought to be protected (e.g. eyes and face)[46]. Unprotected exposure typically occurs due to the failure of protection procedures, such as mistiming the arc striking or exposure to nearby arcs. Moreover, it has been reported that reflected radiation may infiltrate welding helmets from the rear and into the welders' eyes and faces[47, 48]. Therefore, it is imperative to implement a comprehensive protection strategy for welders. As a basis for developing such protective measures, it is essential to acquire a full and quantitative understanding of the optical radiation that may cause photobiological hazards.

There is an extensive literature on the experimental measurement of the effective irradiances (mainly on UV and blue light) for various welding processes, such as gas metal arc welding (GMAW)[49-52], gas tungsten arc welding (GTAW)[51-53], fluxed-cored arc welding[54] and CO_2 arc welding[51, 55]. The radiation hazards can be further evaluated by comparing the measured effective irradiances with corresponding exposure limits proposed by the Directive 2006/25/EC[56] or the American conference

of governmental industrial hygienists[57]. However, the experimental measurements are far from optimal, because it is hard to give an insight into the radiative properties of plasma sources only from effective irradiance. Also, there are still two problems with experimental measurements: the costs of the studies and the risk for testers. Therefore, it is necessary to perform a theoretical study of the optical radiations within different spectral intervals and to evaluate their hazard degrees for welding arc. In this thesis, the UV (180-400 nm), UVA (315-400 nm) and blue light (300-700 nm) radiation that may cause severe photobiological hazards is theoretically investigated for argon GTAW arcs.

This thesis is organised in five chapters:

- The first chapter is dedicated to the presentation of the research background and basic concepts involved. The arc welding processes, thermodynamic states in plasmas, plasma radiation, and the optical photobiological hazards are described.
- Chapter 2 is dedicated to the calculation of the composition and radiative properties of 82%Ar-18%CO_2 thermal plasmas with the addition of metallic vapours (iron in the present case due to workpiece and wire erosion), this mixture being representative of metal active gas (MAG) arc welding processes. These radiative properties are obtained in the frame of the net emission coefficient (NEC) theory, using the recent and accurate "line by line" method. The results calculated will be used to select the spectral intervals for the development of the new diagnostic method (chapter 4). Also, it can provide a data base of radiative properties for the modelling of MAG process.
- Chapter 3 reports the spectroscopic investigation of a pulsed welding arc with 82%Ar-18%CO_2 shielding gas. Excitation temperature is obtained with Boltzmann plot method while iron and argon lines Stark broadening measurements are used to get electron temperature and electron number density. Iron mole fraction in the plasma is calculated by solving the conservation equations. LTE hypothesis validity across the arc is discussed considering the agreement between the two temperatures, the electron density and iron content. Results show supporting evidence for the main part of the plasma, along radial and axial directions.
- Chapter 4 introduces the method that allows to a fast determination of space- and time-resolved plasma temperature and iron concentration in a typical MAG-P arc.

The selection of diagnostic spectral intervals is emphasized. The experimental results are presented for the evolution of the plasma temperature and the iron concentration fields in the arc during the high current period. This method has also been validated for a layer of plasma at the position of 1.5 mm above the workpiece by using a high-resolution spectrometer and adopting other existing diagnostics such as Stark broadening. The plasma temperature and iron concentration show good agreement throughout the different methods, which demonstrates the effectiveness of this new method.

- Chapter 5 presents a theoretical investigation of the UV (180-400 nm), UVA (315-400 nm) and blue light (300-700 nm) radiation associated with the photobiological hazards to workers for argon GTAW arcs. The radiative properties of argon plasma are calculated for the three spectral regions of interest at temperatures from 5000 K to 25000 K and atmospheric pressure. A two-dimensional model of a GTAW arc is then introduced to determine the local emissions in the arc, the total radiation escaping from the arc and corresponding effective irradiances. The photobiological hazards are further evaluated for the three spectral intervals by estimating the permissible exposure durations according to the Directive 2006/25/EC.
- Finally, a general conculsion is given in chapter 6.

Chapter 1 Introduction of arc processes and plasma radiation

In this chapter, the research background and some basic concepts are introduced to better understand related subjects of this thesis. The arc welding is first introduced. The concepts of complete thermodynamic equilibrium (CTE), local thermodynamic equilibrium (LTE) and partial LTE (pLTE) in thermal plasmas are given. Physical quantities and processes concerning the radiation of plasmas are also presented. Finally, optical radiation photobiological hazards on human being are introduced.

1.1 Arc welding

Arc welding is a process that utilizes arc plasmas to melt and join metals. Arc welding processes are widely used in many industrial fields, e.g. in the construction of buildings, vehicles, ships, pipelines and pressure vessels. While there are many arc welding processes, such as flux-core arc welding and manual metal arc welding, gas metal arc welding (GMAW) and gas tungsten arc welding (GTAW) are two most popular variants, which are also the research focus of present thesis.

1.1.1 Gas metal arc welding (GMAW)

Figure 1.1 shows the schematic diagram of GMAW process. The GMAW arc is a high-temperature, ionized column of gas (or plasma) that spans between the continuously fed consumable electrode (typically 0.89–1.60 mm in diameter) and the workpiece, and the arc is sustained by high current (typically 100 to 450 A) provided by a welding power supply offering an electrical potential (typically 15 to 35 V). The standard polarity for GMAW is electrode positive, i.e. the wire is the anode, and the workpiece is the cathode. Due to the heat flux from the arc, a region of the workpiece is melt to form the weld pool. The wire, which is continuously fed to maintain an approximately constant arc length, melts to form droplets that fall through the arc to the weld pool. Upon solidification, the weld pool is permanently fused.

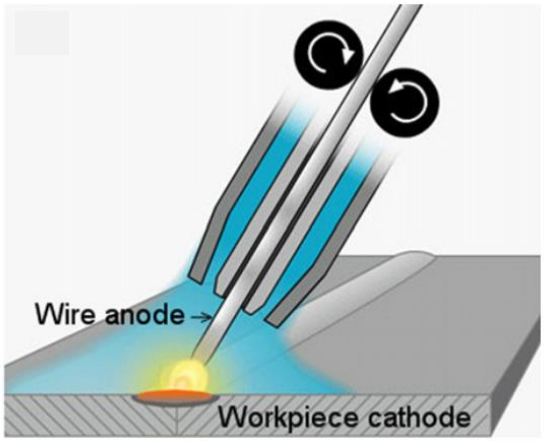

Figure 1.1. Schematic diagram illustrating the GMAW process.

GMAW is also known as metal–inert-gas (MIG) welding or metal–active-gas (MAG) welding, depending on whether the shielding gas is inert (e.g. Ar or He) or active (containing O_2 or CO_2). The shield gas is used to form and stabilize the arc, as well as to shield the molten weld pool from oxidation with the atmosphere and from other atmospheric contaminants. The addition of a certain proportion of O_2 or CO_2 (typically, 18%CO_2 or 2%O_2) in argon (Ar) improves the molten metal mobility and arc stability, reason why the mixtures are favoured in industry. Nevertheless, the selection of an appropriate shield gas for a given weld application should involve a delicate balance between conflicting requirements, and welding equipment, material, and gas characteristics.

Historically, constant voltage power supplies have been employed in the majority of GMAW applications. With this type of power supply, there are three primary modes of metal transfer from the wire to the weld pool: dip transfer, globular transfer and spray transfer. In dip transfer, the wire is fed at a rate faster than it is melted by the arc, so that it eventually bridges the arc gap and reaches the weld pool. The resistive heating of the short circuit heats and ruptures the thin filament of metal bridging the gap, and the arc is re-established until the cycle is repeated. Although the current is high (200 to 400 A) when the short circuit is established, the mean current is typically below 100 A, and the heat transfer is low. In other modes of transfer, there is always a gap between the wire and weld pool. At lower currents, large droplets form at the end of the wire, and subsequently detach and fall through the arc; this is a typical globular transfer. As the current increases, there is a transition to spray transfer, in which

smaller droplets are formed and detach more frequently, up to a few hundred times per second. The transition current depends on the diameter and composition of the wire and the shielding gas composition, but it is typically between 140 and 280 A[5].

As power supplies advanced, it became possible to modify the voltage waveform to effectively overcome some of the drawbacks of purely constant voltage welding systems. Welding current can be cycled at a specified rate from a high peak current to a low background current. In this manner, the metal droplets can be expelled in a stable and spatter-free manner during the high current portion of the pulse, thus approaching the stability found with a standard spray transfer mode. Complete weld fusion is also ensured through the high current pulse, but the drop to a lower background current level serves to limit overall heat input, thus limiting distortion and enabling out-of-position welding. Due to its good performances, the pulsed GMAW (GMAW-P; also known as MIG-P or MAG-P) has been widely used in automated processes.

Nowadays, the GMAW process is also used for hardfacing and repair welding besides joining. The potential of GMAW processes for low-cost additive manufacturing with high deposition rates was studied (see e.g. [58]).

1.1.2 Gas tungsten arc welding (GTAW)

Figure 1.2 shows the schematic diagram of GTAW process. The GTAW uses a refractory material, usually tungsten, as the upper electrode. The tungsten cathode is usually doped with a rare-earth oxide, such as thoria, to decrease the work function and thereby increase the current density at a given temperature. If reinforcement of the weld is required, a metal filler rod is inserted in the arc close to the workpiece. Direct current with electrode negative and workpiece positive is typically used, though use of electric positive or high frequency alternating current, up to 50000 cycles per second (typically less than 500 Hz), is common in aluminum welding to aid in breaking down the thermally stable aluminum oxide layer. Arc currents range from around 100 to 400A relatively low electrical potentials (typically 8 to 12 V for Argon), welding speeds can be up to around 10 mm s^{-1}, depending on the current, and arc lengths are typically 1.5 to 4mm[5]. Various shield gases are used, though typically inert Argon or Helium are used, with the higher ionization energy of He leading to a more constricted and deeper penetrating arc and higher electrical potential.

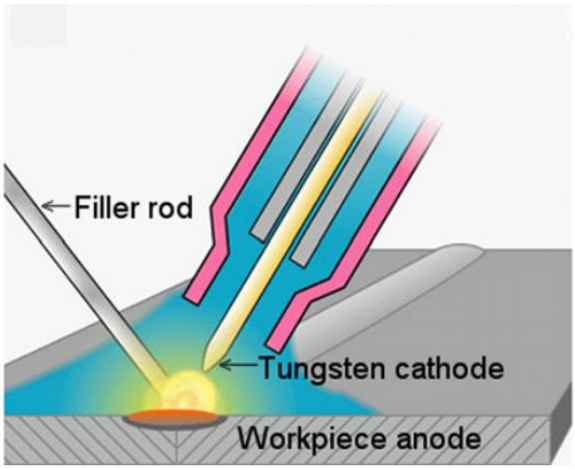

Figure 1.2. Schematic diagram illustrating the GTAW process.

1.2 Thermodynamic state of thermal plasmas

Thermal plasmas are partially or strongly ionized gases, and the welding arc is a typical thermal plasma that is generated by electrical discharges at currents from tens A of to hundreds A. Since the characteristics of plasmas, e.g. electron density, are related to their thermodynamic state, two important thermodynamic concepts in thermal plasma are introduced: complete thermodynamic equilibrium (CTE) and local thermodynamic equilibrium (LTE).

1.2.1 Complete thermodynamic equilibrium (CTE)

Plasmas consist of a large number of particles. These particles with some kinetic and potential energy move in space and collide with neighbouring particles. If there is no exchange of matter or energy with the external environment, a state of micro-reversibility is reached: any mechanism that tends to lose energy to a particle is instantly compensated by the reverse mechanism that tends to make it gain the same energy. This is called complete thermodynamic equilibrium (CTE), where all plasma particles have the same average energy, and all collisional and radiative processes conform to microscopic reversibility.

Indeed, the CTE exists in only plasmas in astrophysics, in particular in stars, where the exchanges of matter and energy with the surrounding environment are

negligible. Take the sun as an example, there are 10^{12} photos emitted inside the sun, and only 1 photo will not be reabsorbed and will come out the sun to go into space. For plasmas in CTE, the following conditions must be met:

* *Maxwell distribution:* the velocity for particles of every species r that existing in plasma, including electrons, must follow a Maxwell distribution

$$f(v_r)=\frac{4v_r^2}{\sqrt{\pi}\left(\frac{2k_BT}{m_r}\right)^{3/2}}\exp\left(-\frac{m_rv_r^2}{2k_BT}\right) \tag{1.1}$$

where v_r is the velocity of particles of species r, m_r is their mass, k_B is the Boltzmann constant, and T is the temperature, which is the same for every species r, is identical to the plasma temperature.

** Boltzmann distribution:* the population density of the excited states of every species r must follow a Boltzmann distribution

$$n_{r,k}=n_r\frac{g_{r,k}}{Q_r}\exp\left(-\frac{E_{r,k}}{kT}\right) \tag{1.2}$$

where n_r is the total number densities of ions of species r, Q_r is their internal partition function, $E_{r,k}$ is the energy of the k^{th} quantum state, and $g_{r,k}$ is the statistical weight of this state. The excitation temperature T is identical to the plasma temperature.

** Mass action law: laws of Saha and Guldberg-Waage*

Saha law: the Saha equation is useful for determining the ratio of particle densities for two different ionization levels

$$\frac{n_{k+1}n_e}{n_k}=\frac{2Q_{r+1}}{Q_r}\frac{(2\pi m_ekT)^{3/2}}{h^3}\exp\left(-\frac{E_{k+1}}{kT}\right) \tag{1.3}$$

Where n_e are the number densities of electrons, m_e is the mass of electron, E_{k+1} is the energy required to produce an (r+1)-times ionized atom from an r-times ionized atom (ionization energy). The ionization temperature T in this equation is identical to the plasma temperature.

Guldberg-Waage law: this law reflects the equilibrium state of dissociation that exists between the densities of the starting species and the species formed.

$$\frac{n_an_b}{n_{ab}}=\frac{Q_a\ Q_b}{Q_{ab}}\left[\frac{2\pi kTM_aM_b}{(M_a+M_b)h^2}\right]^{3/2}\exp\left(-\frac{D_{ab}}{kT}\right) \tag{1.4}$$

Where n_a, n_b and n_{ab} are respectively the number densities of the a, b and ab species, and, Q_a , Q_b and Q_{ab} are respectively their internal partition functions. M_a and M_b are the atomic masses of the a and b species, and D_{ab} is the dissociation energy of the molecule ab.

* *Planck law*: in CTE state, the radiative energy absorbed by a volume element of the plasma is equal to that emitted by this volume element. The electromagnetic radiation field is that of blackbody radiation intensity B_λ as described by the Planck function

$$B_\lambda = \frac{2hc^2}{\lambda^5}\left[\exp\left(\frac{hc}{\lambda kT}\right)-1\right]^{-1} \tag{1.5}$$

The relation between the monochromatic emission coefficient ε_λ and the monochromatic absorption coefficient K'_λ conforms to Kirchhoff's law

$$\varepsilon_\lambda = K'_\lambda \cdot B_\lambda \tag{1.6}$$

1.2.2 Local thermodynamic equilibrium (LTE)

For plasmas used in laboratory, it is impossible to meet the CTE state due to the presence of gradients of temperature, pressure and/or concentration. However, for a dense, collision-dominated and high temperature plasma, in the presence of electric field or moderate external forces, the velocity distribution of the electrons is almost Maxwellian. The average travel distance of the electrons between two collisions is so small that only very small disturbances in the distribution function can occur in time and space. There is micro-reversibility of processes due to collisions, and the plasma is thought to be in local thermodynamic equilibrium (LTE) state.

In LTE, populations of all species and their excited levels are well described by the laws of Maxwell, Boltzmann, Saha and Guldberg-Waage. However, there is no micro-reversibility of processes in radiation and absorption, which implies that Planck's law is no longer valid. Nevertheless, Kirchhoff's law is still valid.

Many thermal plasmas do not meet all requirements for LTE, in other words, they are not in complete local thermodynamic equilibrium (CLTE) due to the lack of the excitation equilibrium (Boltzmann distribution). In particular, the lower-lying energy levels of atoms may be underpopulated due to the high radiative transition probabilities of these levels, resulting in a corresponding overpopulation of the ground

state. Because of the small contribution of excited species to the enthalpy of a plasma, this type of deviation from CLTE is immaterial for most engineering applications. For this reason, such plasmas are still treated as thermal plasmas or, more accurately, as plasmas in partial local thermodynamic equilibrium (PLTE).

Over the past years, numerous analytical and experimental studies demonstrate that LTE (CLTE or PLTE) in high-intensity arcs is the exception rather than the rule. Several studies have shown that, besides the underpopulation of lower-lying energy levels, deviations from LTE can frequently be attributed to strong gradients in the plasma and the associated diffusion effects. More details on LTE and deviations from LTE are discussed in the books of Griem[59, 60] and Boulos *et al*[61].

1.3 Plasma radiation

In this thesis, the main research subjects concerning arc diagnostics and the evaluation of photobiologic hazards are based on the plasma radiation. Therefore, the basic concepts, physical quantities, and physical processes of plasma radiation are presented.

1.3.1 Radiation and emission spectrum

According to the wave theory, any radiation can be considered as the superposition of electromagnetic waves. As for corpuscular theory, it is based on the idea that light is composed of particles, photons, which propagate along light rays. It is considered that each photon is associated with an electromagnetic wave. This is called the wave-particle duality. Each photon that composes the light carries an individual energy, E, proportional to the frequency of its associated wave, v, according to Planck's relation:

$$E=hv \tag{1.7}$$

where h is the Planck constant (h = 6.6260755×10^{34} J.s), E is expressed in Joule (J), and v is expressed in Hertz (Hz or s^{-1}).

The frequency v associated with the wavelength λ is given by:

$$\lambda=\frac{c}{v} \tag{1.8}$$

where λ is the wavelength of the photon, c is the speed of light in the plasma, which is

related to the speed of light in vacuum, c_0 (c_0 = 2.9799×10^8 m.s^{-1}), and the absolute refractive index of the plasma at wavelength, n_λ, by the following expression:

$$c=\frac{c_0}{n_\lambda} \tag{1.9}$$

Each emitted photon corresponds to a wavelength. If we represent the quantity of photons generated for each emission wavelengths, we obtain the emission spectrum of the plasma. To illustrate this, two spectra of argon plasmas at 10000 K and at 20000 K depending on the wavelength are presented in Figure 1.3. The differences that we can observe highlight that radiated energy strongly depends on the wavelength and the temperature of the plasma. More generally, the spectra depend on the experimental conditions: the composition, the pressure, the temperature, the size and the state of the plasma.

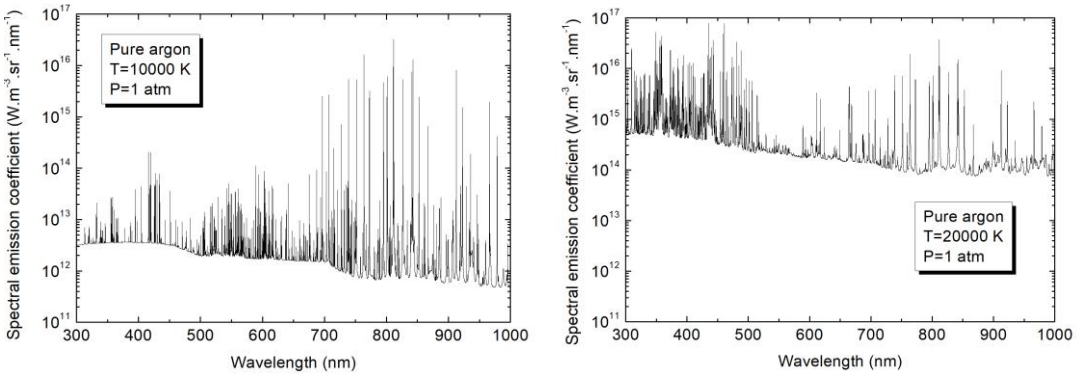

Figure 1.3 spectra of argon plasma ta 10000 K and 20000 K

There are mainly two types of spectra. The first type, called "line spectrum", corresponds to radiation whose energy is concentrated in an extremely narrow range of the spectrum. These are the peaks that can be observed on the spectra of Figure 1.3, and which are generated by transitions of electrons in the bound states of atoms, ions or molecules. These peaks are called emission lines. They are superimposed on the second type of spectrum, called “continuous spectrum”, which comes from radiation whose energy is distributed over an extended range of wavelength. It is generally produced by interactions of the free electrons of the plasma with the other particles.

The emission spectrum is therefore an indicator of the physical phenomena that take place within the plasma. The analysis of the spectrum allows obtaining the

characteristic quantities such as the nature and the density of the species, the pressure, the temperature, the size of the plasma according to its conditions and hypotheses done.

1.3.2 Quantities of optical radiation and radiometry

* *Radiant flux:* as mentioned in the previous paragraph, each of the photons constituting the light moves by carrying energy. The resulting energy flow in unit time is called energetic flux. It is noted as Φ_e, which is expressed in Watt.

* *Radiant intensity:* the radiant intensity I is introduced to characterize the radiation emitted in a direction of space. Expressed in W. sr^{-1}, it is defined as the radiant flux per unit of solid angle $d\Omega$ in the direction considered.

$$I(\theta, \phi)=\frac{d\Phi_e(\theta, \phi, d\Omega)}{d\Omega} \tag{1.10}$$

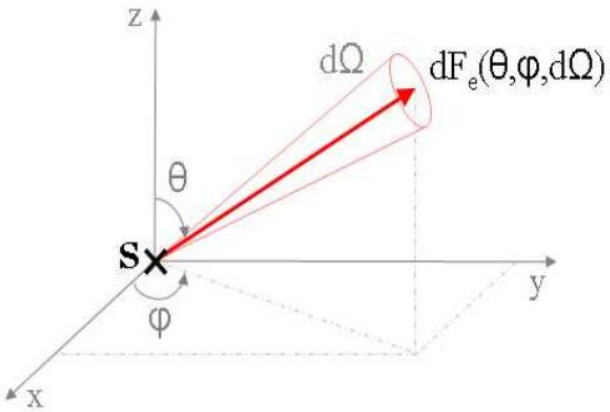

Figure 1.4 Radiant intensity of a light source S

* *Luminance:* the luminance L at a point $\vec{r}$ is the radiant intensity emitted per unit area dA, expressed in W. m^{-2}. sr^{-1}. It is therefore the energy flux radiated by a unit of surface, per unit of solid angle.

$$L(\theta, \phi)=\frac{dI_e(\theta, \phi)}{dA\ cos\theta_A}=\frac{d\Phi_e(\theta, \phi, d\Omega)}{d\Omega\ dA\ \cos\theta_A} \tag{1.11}$$

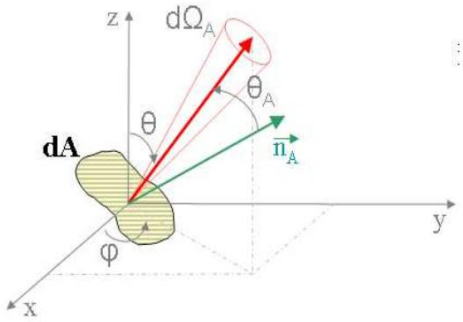

Figure 1.5 Parameters for defining the luminance of an extended radiation source.

The spectral luminance at a given wavelength is given by

$$L_\lambda(\theta, \phi)=\frac{\mathrm{d}L(\theta, \phi)}{\mathrm{d}\lambda} \tag{1.12}$$

We can also introduce the spectral luminance according to the frequency, using the relation:

$$L_\nu \mathrm{d}\nu = L_\lambda \mathrm{d}\lambda \tag{1.13}$$

* *Volumetric Emission Coefficient:* the volumetric monochromatic emission coefficient is the radiant energy dE emitted by a volume element dV in a wavelength interval between λ and λ+ dλ into a solid angle dΩ per unit time dt

$$\varepsilon_\lambda=\frac{\mathrm{d}E}{\mathrm{d}\lambda dt dV d\Omega} \tag{1.13}$$

The unit of ε_λ is W.m^{-4}.sr^{-1}. The volume element dV should be so small that absorption and induced emission processes occurring within it are negligible.

The integrated volumetrie emission coefficient ε_V is

$$\varepsilon_V = \int \varepsilon_\lambda \, \mathrm{d}\lambda \tag{1.13}$$

* *Radiant exposure:* the radiant exposure H is the radiant energy received by a surface per unit area, expressed in J. m^{-2}. Its spectral radiant exposure H_λ or H_ν is expressed in J.m^{-3} or J·m^{-2}·Hz^{-1}, respectively.

* *Irradiance:* the irradiance E is the radiant power incident per unit area upon a surface, expressed in W. m^{-2}. The irradiance of a surface integrated over time of irradiation is equivalently the radiant exposure H. The spectral irradiance, E_λ or E_ν, is the spectral irradiance unit wavelength or frequency.

1.3.3 Emission and absorption

In a plasma, when the radiation emitted by a volume element travels through the plasma, the observations of the radiation may be affected by the absorption during transmission. Hence, the problem of absorption shouldn't be ignored in arc diagnostics. To describe the absorption phenomenon, the absorption coefficient is introduced. If the spectral luminance L_λ passes through an absorbing medium of thickness dr, then K_λ, the absorption coefficient per unit length at wavelength λ, is given by

$$K_\lambda(r)=-\frac{\mathrm{d}L_\lambda(r)}{L_\lambda(r)\mathrm{d}r} \tag{1.14}$$

As shown in Figure 1.6, assuming that the radiation travels homogeneous and isothermal plasma from the point r to r+dr, the variation of the luminance in the direction of r is $\mathrm{d}L_\lambda(\mathrm{r})$. The energy balance becomes:

$$\frac{\mathrm{d}L_\lambda(r)}{\mathrm{d}x}=\varepsilon_\lambda-K_\lambda(r)L_\lambda(r) \tag{1.15}$$

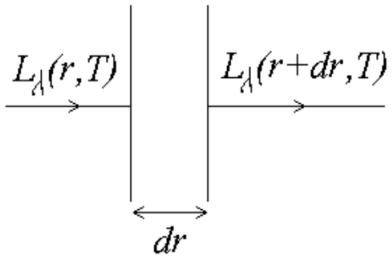

Fig.1.6 Variation of the luminance along a luminous path

Solving equation (1.15) leads to

$$L_\lambda(\mathrm{r})=L_\lambda(0)\exp\left(-\int_0^{\mathrm{r}_0}\kappa_\lambda(\mathrm{r})\mathrm{d}\mathrm{r}\right)+\int_0^{\mathrm{r}_0}B_\lambda(\mathrm{r})\exp\left(-\int_0^{\mathrm{r}_0}\kappa_\lambda(\mathrm{r})\mathrm{d}\mathrm{r}\right)\mathrm{d}\mathrm{r} \tag{1.16}$$

1.4 Photobiological hazards from optical radiation

1.4.1 Optical radiation

Optical radiation, which is part of electromagnetic spectrum, refers to the group of ultraviolet (UV), visible, and infrared (IR) radiation. The term “optical radiation” is used because the radiation obeys the laws of optics, and it has effects on eyes. The

boundaries between these spectral regions are not definitive and may vary in applications (physical or biological). Biologically, the spectrum of optical radiation is usually divided into wavelength intervals, as shown in table 1.1[44]:

Table 1.1 Photobiological schemes for dividing the optical radiation spectrum

Wavelength regions	Wavelength range
UVC	100–280 nm
UVB	280–315 nm
UVA	315–400 nm
Visible	380–780 nm
IRA	780–1 400 nm
IRB	1400–3000 nm
IRC	3000–1×10^6 nm

Note: the UV radiation in the wavelength range below 180 nm (vacuum UV) is strongly absorbed by the oxygen in air and therefore does not travel in the air.

The wavelength is related to the amount of radiative energy. The shorter the wavelength, the more energetic the radiation is. Blue light is more energetic than green light which, in turn, is more energetic than red light. Ultraviolet radiation is more energetic than any visible wavelength. It is convenient to consider optical radiation as a stream of massless particles, called photons.

Optical radiation can be produced by various sources, which may be simply classified into inartificial and artificial sources. The primary representative of the former is the sun, which gives off solar radiation and bring light for human being. The sources of artificial optical radiation involve a wide range of aspects, from daily life (e.g. lighting by the use of incandescent and fluorescent lamps) to industry applications (hot industries, such as glass and metal working, where furnaces emit IR radiation; non-destructive testing, which is used to reveal fluorescent dyes with ultraviolet radiation; cosmetic treatment, which makes use of lasers and flash lamps, as well as ultraviolet and infrared sources; material processes utilizing welding arc or laser, etc). For most individuals, the sun is the main optical radiation source, but in occupation environment the welding arc is the predominant and the most intense radiation source[43, 44].

1.4.2 Photobiological effects at different wavelengths

When optical radiation interacts with the body, it is probable to deposit some energy at the contact point and cause some biological effects. For example, visible light arriving at the retina with enough energy can trigger biological reactions which produce a visual signal in the brain. Since optical radiation is absorbed in the outer surfaces of the body, its biological effects are mainly confined to the eye and the skin.

The biological effects depend on not only the quantity of radiation and radiation time but also the wavelength of radiation, because different wavelengths can be absorbed by different part of the eye and the skin and the types of interaction involved also vary (photochemical effects dominate in the UV region, and thermal effects in the IR region). Also, the biological effects can be broadly divided into acute (rapidly occurring) and chronic (occurring as a result of prolonged and repeated exposures over a long time).

The structure of the eye and the skin and the photobiological effects of different wavelengths on them are presented as follows.

The eye

Light entering the eye passes through the cornea, aqueous humour, then through a variable aperture (pupil), and through the lens and vitreous humour to be focused on the retina. The optic nerve carries signals from the photoreceptors of the retina to the brain. The anatomy of the eye is shown in Figure 1.7. The main components of the eye involved in the light transmission are briefly described in the following text.

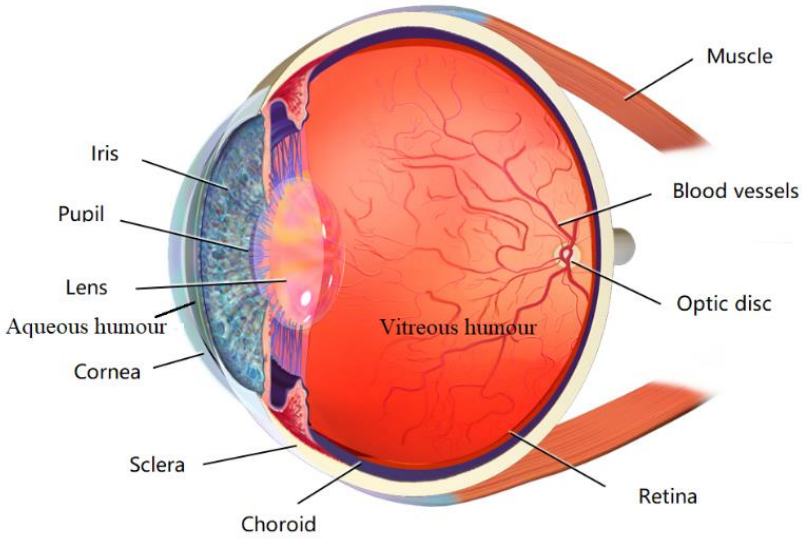

Figure 1.7 Anatomy of the eye[44]

The cornea, an about 1 mm thick film, is the transparent front of the eye, accounting for one sixth of the outer area. It covers the iris, pupil, and anterior chamber and provides most of refractive power for the eye. Together with the lens, the light can be accurately focused on the retina to form images. Since cornea is rich in sensory nerve endings, any minor irritation, injury or inflammation may cause pain and lacrimation.

The iris is a circular structure with pigment film, containing connective tissue cells, muscle fibres. The colour of the eyeball is determined by the pigment contained. The iris's centre is a circular opening, called the pupil. The iris contains two opposite layers of smooth muscle, causing the pupil to magnify under low light (increasing the amount of the light) and to contract under intense light (decreasing the amount of the light).

The lens, located behind the iris and before the vitreous humour, is a transparent double-convex oblate. It is the main refractive structure of the eye. The periphery of the lens is anchored to the surrounding ciliary body with a lens suspension (ciliary band). The dioptre of the lens is regulated by the ciliary muscle, i.e. the lens suspension is relaxed, and the degree of lens convexity increases; the lens suspension is tightened, and the convexity of the lens decreases.

The retina is a transparent light-sensitive layer of tissue behind the eyeball. The

visible light falling in the retina forms a visual nerve impulse, which is then transmitted to the visual centre along the visual pathway to establish the image in our mind. The retina is composed of the pigment epithelium and retinal sensory layer. The pigment epithelium consists of pigmented epithelial cells that are responsible for supporting and nourishing photoreceptor cells, radiating heat, shading, and regenerating and repairing. The sensory layer on the retina consists of three neurons. The first neuron is the visual cell layer, which includes cone and rod cells and is specialized in sensitization. The second layer, called double cells, connects a two-node cells and a ganglion cells with about 10 to hundreds of visual cells and is responsible for liaison. The third layer, called the cell layer, is responsible for conducting information.

Prior study has illustrated that the penetration of optical radiation through the eye varies depending on wavelength[43, 44]. As shown in Figure 1.8, UVC is absorbed in the superficial layers of the cornea, UVB is absorbed by the cornea and lens, UVA passes through the cornea and is absorbed in the lens, visible light and IRA are focused by the cornea and lens and transmitted to the retina, IRB is mainly absorbed by the aqueous humour and vitreous humour, and IRC is absorbed by the cornea.

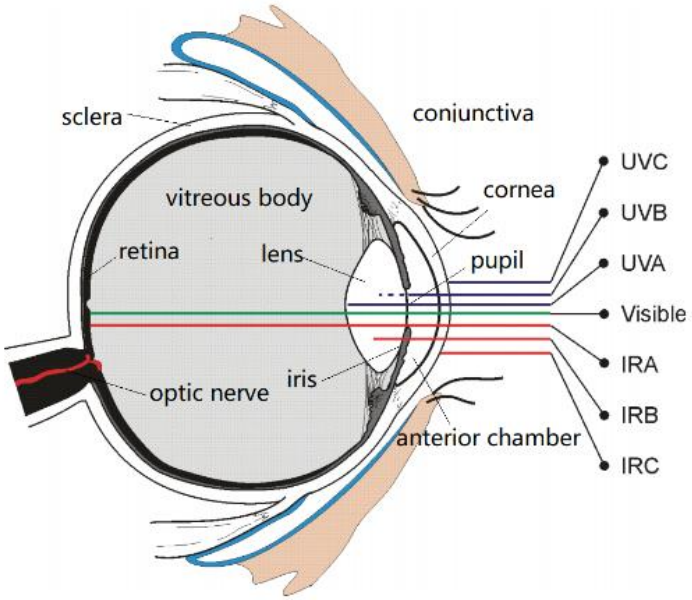

Figure 1.8 Penetration of different wavelength through the eye[44]

The acute biological effects from excessive UV exposure include photokeratitis and conjunctivitis (inflammation of the cornea and conjunctiva, respectively), more

commonly known as snow blindness or welder's flash. Acute symptoms, ranging from mild irritation, light sensitivity and tearing to severe pain, usually appear within thirty minutes to a day and disappear in a few days. Chronic exposure to UV (UVA and UVB) can cause corneal and conjunctival disorders (such as climatic droplet keratopathy, pterygium, and probably pinguecula) and lens disease (typically, cataracts).

Excessive exposure of visible radiation can cause retina damage. The retinal damage caused by thermal effects (denaturation of proteins appears if temperature increases 10–20 °C) may happen when heat is not shed quickly enough, although there are natural protective measures (such as the pupil contracts to reduce retinal irradiance; the head is turned involuntarily away). Visible radiation can also cause the same type of photochemically induced damage as ultraviolet radiation. This effect is most pronounced at wavelengths around 435–440 nm, and so it is sometimes called the 'Blue-Light hazard'. Chronic exposure to high ambient levels of visible light may be responsible for photochemical damage to the cells of the retina, resulting in poor colour and night vision.

IRA can cause the same sort of thermal damage as visible radiation can, since IRA is also focused by the cornea and lens and transmitted to the retina. However, the retina does not detect IRA, and so there is no natural aversion responses. The spectral region of 380 to 1400 nm (visible and IRA) is sometimes referred to as the "retinal hazard region". Chronic exposure to IRA may also induce cataracts. IRB can be absorbed by aqueous humour and vitreous humour; thus, the retina is protected. The thermal damage due to IRB can cause cataracts, which have been an important occupational disease for some groups, principally glass blowers and chain makers. IRC is absorbed by the cornea, and so the main hazard is corneal burns.

The skin

Figure 1.9 shows the anatomy of the skin. The skin, the outer covering of the body, is the body's largest integumentary organ. It consists of the epidermis, dermis and subcutaneous tissue. The epidermis contains mainly keratinocytes (squamous cells) which are produced in the basal layer and rise to the surface to be sloughed off.

The dermis is composed mainly of collagen fibres and contains nerve endings, sweat glands, hair follicles and blood vessels

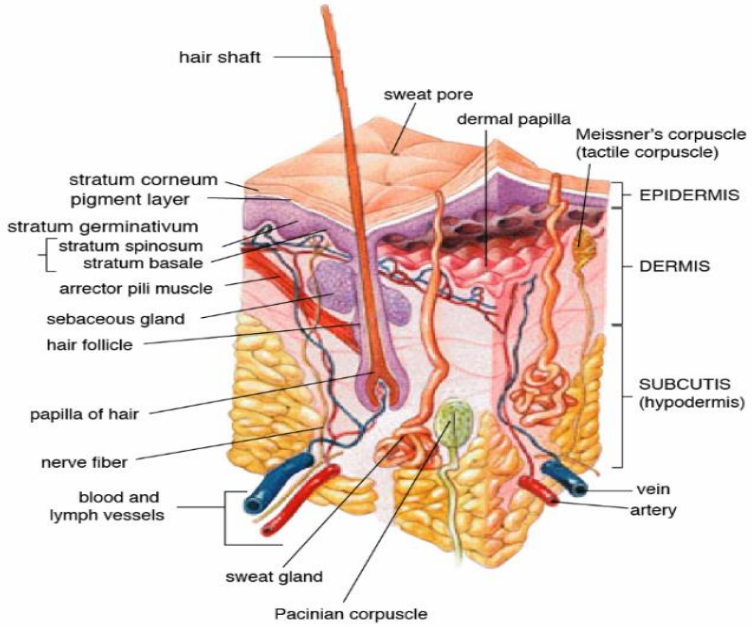

Fig. 1.9 Anatomy of the skin[44]

The radiation with different wavelength has different penetration through the skin, as shown in Fig. 1.10. For example, much of any UV radiation incident on the skin is absorbed in the epidermis, although penetration increases markedly for the longer UVA wavelengths.

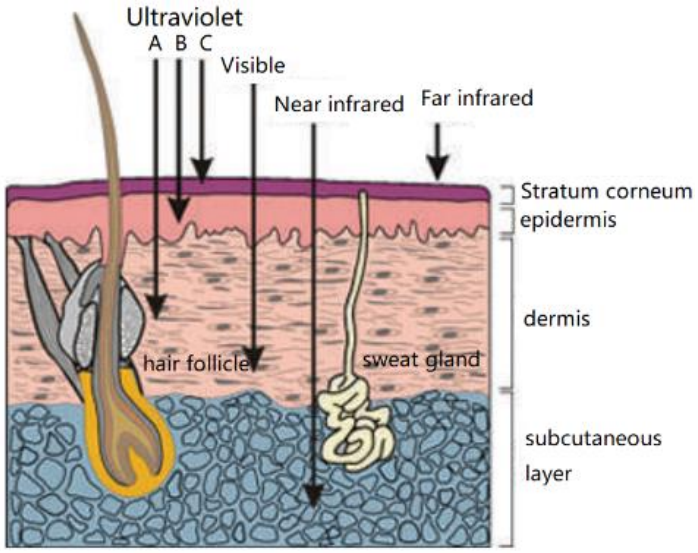

Fig. 1.10 Penetration of different wavelength through the skin[44]

Excessive short-term exposure to UV radiation causes erythema — a reddening of the skin and swelling. Symptoms can be severe, and the maximum effect occurs 8–24 hours after exposure, subsiding over 3–4 days with subsequent dryness and skin peeling. Chronic exposure to UV radiation can cause photoaging of the skin, which is characterised by a leathery wrinkled appearance and loss of elasticity: UVA wavelengths are the most effective as they can penetrate to the collagen and elastin fibres of the dermis. However, the most serious long-term effect of UV radiation is the induction of skin cancer, such as basal cell carcinomas, squamous cell carcinomas and malignant melanoma.

Visible and near IR (UVA and UVB) radiation penetrates into the skin and may raise the local temperature enough to cause burning. The body will adjust to gradual temperature rises by increasing blood flow (which carries heat away) and perspiration. For long exposure durations, heat strain from thermal stress (increased core body temperature) is the principal adverse effect. IRC penetrates only to the uppermost layer of dead skin cells (stratum corneum) and thus its effect is insignificant.

Chapter 2 Calculation of equilibrium composition and radiative property

The new method for diagnosting metal active gas (MAG) arcs (chapter 4) requires the prerequisite knowledge of radiative properties of plasmas. Hence, this chapter is dedicated to the calculation of the radiative properties of 82%Ar-18%CO_2 thermal plasmas with the addition of metallic vapours (iron in the present case due to workpiece and wire erosion), this mixture being representative of MAG arc welding processes. The radiative properties of plasmas depend on the compositions of [82%Ar-18%CO_2]-Fe plasmas that are also presented.

These radiative losses are obtained in the frame of the net emission coefficient (NEC) theory, using spectra deduced by the accurate line by line" method. All significant radiative contribution mechanisms are taken into account in the calculation. The spectra and NECs build an interesting and useful database for the new diagnostic method studied in chapter 4. Also, the NECs are essential and valuable data for the modelling of MAG arc, although the modelling work is not performed in this paper.

To obtain fine spectra, two special treatments were involved in the calculation: the "line by line" method and the consideration of the molecular radiation. Indeed, the emission of atomic lines is usually considered through the escape factor[62] by neglecting the overlapping of lines, which spare the calculation time but tend to overestimate the radiation[11]. Due to numerous iron lines (94920 lines) in plasmas, the line overlapping was taken into account by using the "line by line method"[37]. In addition, when the temperature is lower than 10 kK, the contribution of molecular species should not be neglected in presence of oxygen[63] and carbon[40]. Considering large area of GMAW arcs may be below 10 kK, the emission of the molecular systems of O_2, CO, CO^+, C_2, CO_2 and O_3 were taken into account. This calculation will provide a basis for the selection of spectral intervals needed for arc diagnostic. Also, it builds a numerical data bank of radiative properties for the modelling of the MAG arc

2.1 Plasma composition

Because the radiative properties of plasmas strongly depend on the chemical species in the mixture, the equilibrium composition was firstly calculated for the [Ar-CO_2]-Fe plasmas with different iron content in the temperature range 3 kK-30 kK and at atmospheric pressure. The molar ratio for the shielding gas is supposed to be constant as 82%Ar-18% CO_2. The computation was performed under the LTE assumption. The atmospheric pressure was chosen because MAG process is always undertaken at this pressure. 39 chemical species were taken into account, as listed in table 2.1.

Table 2.1. Chemical species at equilibrium state for [Ar-CO_2]-Fe plasmas.

Atoms, atomic ions and electron	Diatomic molecules and ions	Polyatomic molecules and ions
Ar, Ar^+, Ar^{2+}, Ar^{3+}, C, C^-, C^+, C^{2+}, C^{3+}, O, O^-, O^+, O^{2+}, O^{3+}, Fe, Fe^-, Fe^+, Fe^{2+}, Fe^{3+}, e^-	C_2, C_2^+, C_2^-, O_2, O_2^+, O_2^-, CO, CO^+, FeO, Fe_2	C_3, C_3^-, CO_2, CO_2^-, C_2O, O_3, C_4, C_3O_2, FeC_5O_5

2.1.1 System of Equations

The calculation of plasma composition was realized by solving the coupled equations that describe the conservation of atomic nucleus, electrical neutrality and particle density (pressure conservation) and the mass action law.

Conservation equations

** Conservation of atomic nucleus:* this equation concerns the ratios of chemical elements. In the case of the (1-Y_{Fe}) [82%Ar-18%CO_2]-Y_{Fe} Fe mixtures, in which the mole fraction of iron is Y_{Fe}, these ratios for Ar, C, O, and Fe are

$$\eta_{Ar}:\eta_C:\eta_O:\eta_{Fe}=(1-Y_{Fe})\times 0.82:(1-Y_{Fe})\times 0.18:(1-Y_{Fe})\times 0.18\times 2:Y_{Fe} \qquad (2.1)$$

Since the ratio of two chemical elements should be equal to the ratio of their atomic nucleus number densities. The above equation can be written as

$$\eta_{Ar}/\eta_{Fe}=\sum_{i=1}^{N} n_i C_{i,Ar}/\sum_{i=1}^{N} n_i C_{i,Fe} \qquad (2.2)$$

$$\eta_{Ar}/\eta_{C}=\sum_{i=1}^{N} n_i C_{i,Ar}/\sum_{i=1}^{N} n_i C_{i,C} \qquad (2.3)$$

$$\eta_{C}/\eta_{O}=\sum_{i=1}^{N} n_i C_{i,C}/\sum_{i=1}^{N} n_i C_{i,O} \qquad (2.4)$$

$\sum_{i=1}^{N} n_i C_{i,\mathrm{Ar}}$、$\sum_{i=1}^{N} n_i C_{i,\mathrm{C}}$、$\sum_{i=1}^{N} n_i C_{i,\mathrm{O}}$ and $\sum_{i=1}^{N} n_i C_{i,\mathrm{Fe}}$represent the number densities of the Ar, C, O and Fe atomic nucleus in the plasma, respectively. n_i is the particle number density relative to the gaseous species X_i, and N is the species number (N=39). $C_{i,\mathrm{Ar}}$, $C_{i,\mathrm{C}}$, $C_{i,\mathrm{O}}$ and $C_{i,\mathrm{Fe}}$ are the coefficients that each gaseous species contains the Ar, C, O and Fe atomic nucleuses, respectively. For example, $C_{i,\mathrm{Ar}}(\mathrm{Ar}^{+})$=1, $C_{i,\mathrm{C}}(CO_2)$=1, $C_{i,\mathrm{O}}(CO_2)$=2 and $C_{i,\mathrm{Fe}}$(FeO)=1.

** Electrical neutrality:* the electrical neutrality equation is given by

$$\sum_{i=1}^{N} n_i C_{i,\mathrm{charge}} = 0 \tag{2.5}$$

where $C_{i,\mathrm{charge}}$ is the charge number of each species. For example, $C_{i,\mathrm{charge}}$(Ar+)=1.

** Conservation of particle density:* the total particle number density in the plasma confirms to the gas state equation:

$$\sum_{i=1}^{N} n_i = \frac{P}{k_B T} \tag{2.6}$$

where P is the pressure and k_B is the Boltzmann constant.

Through an analysis of the conservation equations, one can write them as a linear equation involving the particle number density n_i:

$$\left\{\sum_{i=1}^{N} A_{l,i}\, n_i = A_l^{\circ}\right\}_{l=1}^{M} \tag{2.7}$$

where $A_{l,i}$ and A_l° refer to the coefficients of the conservation (see table 2.2) and the index l represents a given equation above. M and N are the numbers of conservation equations and unknowns respectively. In this case, M=5, and N=39.

Table 2.2. coefficients of conservation.

Equation type	$A_{l,i}$	A_l°	Number of equations
Conservation of atomic nucleus	$\eta_{\mathrm{Ar}} C_{i,\mathrm{Fe}} - \eta_{\mathrm{Fe}} C_{i,\mathrm{Ar}}$ $\eta_{\mathrm{Ar}} C_{i,\mathrm{C}} - \eta_{\mathrm{C}} C_{i,\mathrm{Ar}}$ $\eta_{\mathrm{C}} C_{i,\mathrm{O}} - \eta_{\mathrm{O}} C_{i,\mathrm{C}}$	0 0 0	3
Electrical neutrality	$C_{i,\mathrm{charge}}$	0	1
Conservation of particle density	1	$\frac{P}{k_B T}$	1

Chemical equations

For the mixture, the conservation equations above include M equations (M=5), while there are N chemical species needed to be solved (N=39). Hence, there still need 34 equations. These equations needed can be provided by chemical equations.

For a plasma mixture, the chemical reaction can be symbolized as:

$$\sum_{i=1}^{\text{species}} v_i \mathrm{X}_i \rightleftharpoons 0 \tag{2.8}$$

Where v_i is the reaction coefficient, specifying the stoichiometry of the reaction. As an example, the well-known reaction $2H_2+O_2 \rightleftharpoons 2H_2O$ would be simply specified by:

$$X_i = \{H_2, O_2, H_2O\}; \qquad v_i = \{2, 1, -2\};$$

For the [82%Ar-18%CO_2]- Fe plasmas, the chemical reactions are complicated because many chemical species have to be taken into account. To represent the chemical reaction involved, an efficient method proposed by Godin and trèpanier[64] was adopted. A subset of species $\boldsymbol{b}$ is regarded as the chemical basis. The chemical basis $\boldsymbol{b}$ contains M species and involves all chemical elements existing in the mixture. The other species $\boldsymbol{b}^*$ can be formed and represent by $\boldsymbol{b}$

$$\boldsymbol{b}^* \rightleftharpoons \boldsymbol{v}\boldsymbol{b} \;\Leftrightarrow\; b_j^* \rightleftharpoons \sum_{k=1}^{M} v_{j,k} b_k \tag{2.9}$$

where $\boldsymbol{v}$ is the coefficient matrix related to the reactions, and subscription $j \in (1, N\text{-}M)$. For example, $\boldsymbol{b}$= {Ar^{2+}, C^{2+}, O^{2+}, Fe^{2+}, Fe^{3+}}, $\boldsymbol{b}^*$= {Ar, CO_2, CO, Fe^+, Ar^+, Ar^{3+}, C, C^-, C^+, C^{3+}, O, O-, O+, O^{3+}, Fe, Fe^-, e, C_2, O_2, Fe_2, C_2^+, C_2^-, O_2^+, O_2^-, CO^+, C_3, C_3^-, CO_2^-, C_2O, O_3, C_4, C_3O_2, FeC_5O_5, FeO}. The non-basis $\boldsymbol{b}^*$ can be expressed by the chemical basis $\boldsymbol{b}$ as follows

$$\begin{pmatrix}
\mathrm{Ar} & 1\mathrm{Ar}^{2+} + 0\mathrm{C}^{2+} + 0\mathrm{O}^{2+} + 2\mathrm{Fe}^{2+} - 2\mathrm{Fe}^{3+} \\
\mathrm{CO_2} & 0\mathrm{Ar}^{2+} + 1\mathrm{C}^{2+} + 2\mathrm{O}^{2+} + 6\mathrm{Fe}^{2+} - 6\mathrm{Fe}^{3+} \\
\mathrm{CO} & 0\mathrm{Ar}^{2+} + 1\mathrm{C}^{2+} + 1\mathrm{O}^{2+} + 4\mathrm{Fe}^{2+} - 4\mathrm{Fe}^{3+} \\
\mathrm{Fe}^{+} & 0\mathrm{Ar}^{2+} + 0\mathrm{C}^{2+} + 0\mathrm{O}^{2+} + 2\mathrm{Fe}^{2+} - 1\mathrm{Fe}^{3+} \\
\mathrm{Ar}^{+} & 1\mathrm{Ar}^{2+} + 0\mathrm{C}^{2+} + 0\mathrm{O}^{2+} + 1\mathrm{Fe}^{2+} - 1\mathrm{Fe}^{3+} \\
\mathrm{Ar}^{3+} & 1\mathrm{Ar}^{2+} + 0\mathrm{C}^{2+} + 1\mathrm{O}^{2+} - 1\mathrm{Fe}^{2+} + 1\mathrm{Fe}^{3+} \\
\vdots & \\
\mathrm{FeO} & 0\mathrm{Ar}^{2+} + 0\mathrm{C}^{2+} + 1\mathrm{O}^{2+} + 5\mathrm{Fe}^{2+} - 4\mathrm{Fe}^{3+}
\end{pmatrix} \tag{2.10}$$

In an equilibrium system, the chemical equilibrium condition confirms to the minimization of Gibb's free energy, and the chemical reactions must obey the mass

action law[64]:

$$\prod_i^{\text{species}} n_i^{v_i} = \prod_i^{\text{species}} Q_i^{v_i} \tag{2.11}$$

Q_i is the partition function per unit volume for the species X_i.

$$Q_\text{i} = \left(\frac{2\pi m_i k_\text{B} T}{h^2}\right) Q_{\text{int},i} \exp\left(-\frac{\varepsilon_\text{i}}{k_\text{B} T}\right) \tag{2.12}$$

where m_i、$Q_{\text{int},i}$ and ε_i are the mass, the internal partition function (IPF) and the first energy level (eV) for the species X_i, respectively.

After applying Eqs. (2.8) and (2.11) to Eq. (2.9), each non-basis species can be written to this set of expressions:

$$\left\{ n_{b_j^*} = Q_{b_j^*} \prod_{i=1}^{M} \left(\frac{n_{b_i}}{Q_{b_i}}\right)^{v_{j,i}} \right\}_{j=1}^{N\text{-}M} \tag{2.13}$$

where n_{b_i} and $n_{b_j^*}$ are the particle number densities of the basis and non-basis species, respectively. Q_{b_i} and $Q_{b_j^*}$ are the IPFs of the basis and non-basis species, respectively.

The above expressions lead to *N-M* equations which represent the particle number densities for non-basis species by means of that for chemical basis. For example, the number densities of CO_2 corresponding to the reaction given in Eq. (2.10) can be written as:

$$n_{\text{CO}_2} = \frac{n_{\text{CO}_2}}{Q^0_{\text{Ar}^{2+}} Q^1_{\text{C}^{2+}} Q^2_{\text{O}^{2+}} Q^6_{\text{Fe}^{2+}} Q^{-6}_{\text{Fe}^{3+}}} n^0_{\text{Ar}^{2+}} n^1_{\text{C}^{2+}} n^2_{\text{O}^{2+}} n^6_{\text{Fe}^{2+}} n^{-6}_{\text{Fe}^{3+}} \tag{2.14}$$

2.1.2 Algorithm and essential data

Due to the introduction of the chemical basis, the conservation equations (2.7) can be written in a way that combines the basis with non-basis terms as follows:

$$\left\{ -A_l^\text{o} + \sum_{i=1}^{M} A_{l,b_i} n_{b_i} + \sum_{j=1}^{N\text{-}M} A_{l,b_j^*} n_{b_j^*} = 0 \right\}_{l=1}^{M} \tag{2.15}$$

By replacing the non-basis density with equation (2.13), one can further obtain the final expressions:

$$\left\{ -A_l^\text{o} + \sum_{i=1}^{M} A_{l,b_i} n_{b_i} + \sum_{i=1}^{N\text{-}M} A_{l,b_j^*} \left[Q_{b_j^*} \prod_{i=1}^{M} \left(\frac{n_{b_i}}{Q_{b_i}}\right)^{v_{j,i}} \right] = 0 \right\}_{l=1}^{M} \tag{2.16}$$

The above equation set contains only the number density of the basis. Since it is non-linear, newton's algorithm[65] is used to achieve a fast solution. In Newton's algorithm, the number density n_{b_i} of the basis is replaced iteratively by corrections $\delta_{n_{b_i}}$, and the solution become the iterative solution of a linear system of equations:

$$\sum_{i=1}^{M} J_{l,i}\delta_{n_{b_i}} = -R_l \;\Leftrightarrow\; \boldsymbol{J}\cdot\boldsymbol{\delta_n} = -\boldsymbol{R} \tag{2.17}$$

Where $\boldsymbol{J}$ and $\boldsymbol{R}$ are the Jacobin matrix and residual vector, respectively. They are expressed as follows:

$$R_l = -A_l^{o} + \sum_{i=1}^{M} A_{l,b_i} n_{b_i} + \sum_{j=1}^{N-M} A_{l,b_j^*} n_{b_j^*} \tag{2.18}$$

$$J_{l,i} = -A_{l,b_i} - \frac{1}{n_{b_i}} \sum_{i=1}^{M} A_{l,b_i} + \sum_{j=1}^{N-M} A_{l,b_j^*} n_{b_j^*} v_{j,i} \tag{2.19}$$

Internal partition functions (IPF) are essential data for the calculation of plasma composition. IPFs of atoms and their positive ions were calculated with the degeneracies and electronic level energies taken from the database of NIST[66]; these IPFs were systematically compared with Drawin and Felenbok's IPF complication[67]. For the negative ions, IFP were assumed to be equal to the degeneracy of the ground state. According to Herzberg[68], we adopted the Morse potential minimization method[69] to calculate the IPF of the diatomic molecules. For polyatomic molecules, IPF were calculated according to Herzberg[70] in the frame of the harmonic oscillator and the rigid rotator assumptions. The required spectroscopic data (Dunham coefficients, moments of inertia, degeneracies, vibrational frequencies and symmetry number) were taken from Huber and Herzberg[71] and Chase *et al*[72].

Figure 2.1 shows the composition of a 95% [Ar-CO_2]-5% Fe mixture at 1 atm, as an example. At low temperature (T< 4kK), the plasma is dominated by the neutral atoms (Ar, Fe, O) and the molecules (CO_2, CO, O_2 and FeO). Above 4 kK, the Fe^+ ions gradually increase, and then the ions C^+, Ar^+, O^+ successively appear and increase together with the electrons; this rise of the ions population is due to the lower ionization energy of iron (7.902 eV) compared with those of others (11.260 eV, 13.618 eV and 15.760 eV for C, O and Ar respectively). Above 15kK, plasma is mainly composed of charged particles. A complete data of the plasma compositions with various iron concentration are given in appendix I.

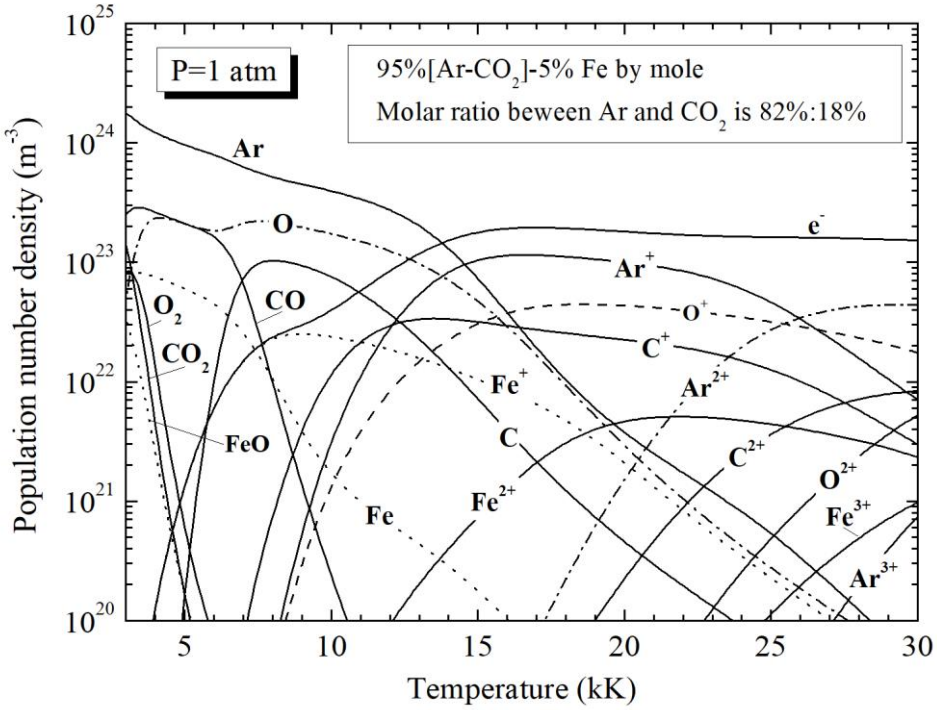

Figure 2.1. Equilibrium composition of 95% [82%Ar-18%CO_2]-5% Fe mixture (molar proportion) at 1 atm.

2.2 Net emission coefficient (NEC)

There are many methods to represent the spectral radiation from a given geometrical plasma, such as the NEC method[73], the Partial Characteristics method[74], the Discrete Ordinates Method[75], the k-distribution[76], the PN approximation[77] and the Monte Carlo method[78]. Some of these methods are detailed in works of Siegel and Howell[79] and Modest[80]. However, the most popular method used in modelling and spectral diagnostics is the NEC method. The NEC is defined as the divergence of the radiative flux at the center of a spherical, homogeneous and isothermal plasma[73]. The NEC can be interesting for plasma diagnostics using camera[36] since we can estimate the radiation of specific spectral intervals (we speak about "partial NEC") and compare the results with measurements. Moreover, the NEC calculated over the total spectrum is widely accepted in modelling the radiative losses in the hot zones of plasma[81-83]. However, the NEC is not useful for high temperature gradients, and in cold regions more particularly the edges of the plasma where absorption can be significant. The NEC is defined as follows:

$$\varepsilon_{\mathrm{N}}\left(T,R_{\mathrm{p}}\right)=\int_0^{\infty} B_{\lambda}(T)\cdot K^{'}(\lambda,T)\cdot\exp\left(-K^{'}(\lambda,T)\cdot R_{\mathrm{p}}\right)\cdot\mathrm{d}\lambda \tag{2.20}$$

where R_{p} is the plasma radius based upon the assumption of a plasma spherical, homogeneous and isothermal, $B_{\lambda}(T)$ is the Planck function and $K^{'}(\lambda,T)$ is the total monochromatic absorption coefficient correlated with the local emission coefficient by Kirchhoff's law: $\varepsilon_{\lambda}(T)=B_{\lambda}(T)\cdot K^{'}(\lambda,T)$. The NECs are quoted for a given plasma radius R_{p}. This radius is chosen to be the radius of high temperature region of arc where the absorption is mainly realized, and it is about 1 millimeter for a welding arc[84].

2.3 Radiative mechanisms

In order to calculate ε_{N} from equation (2.20), the first term to be determined is the monochromatic absorption or emission coefficient, as both are related according to Kirchhoff's law. The local emission of radiation includes contributions from the atomic lines, atomic continuum (radiative attachment, radiative recombination and bremsstrahlung), molecular bands for diatomic and polyatomic molecules, and molecular continuum.

2.3.1 Radiation from the atomic lines

The line emission results from the spontaneous transition of an excited electron from a high energy level E_i to a lower energy E_j. In the calculation, 117213 atomic lines (6672 lines for atomic carbon species, 6217 lines for atomic oxygen species, 9404 lines for atomic argon species, and 94920 lines for atomic iron species) are taken into account. The monochromatic emission coefficient is expressed as:

$$\varepsilon_{\lambda}^{\mathrm{lines}}(T)=\frac{hc}{4\pi\lambda_{ij}}\cdot A_{ij}\cdot N_{\mathrm{i}}(T)\cdot P_{ij}^{\mathrm{Voigt}}(\lambda) \tag{2.21}$$

where λ is the wavelength, h and c are the Planck constant and the speed of light respectively, λ_{ij} is the transition wavelength, A_{ij} is the spontaneous emission probability issued from the table of Moore[85], NIST table[66] and Kurucz and Peytremann[86], N_i is the population number density of the particles in their excited states, and $P_{ij}^{\mathrm{Voigt}}(\lambda)$ is the normalized profile of the line.

Usually, in order to simplify the treatment of the spectra, the line overlapping is

neglected, each line is treated separately through the escape factor proposed by Drawin and Emard[62]. This factor is defined for a line as the ratio of the radiative flux escaping from isothermal plasma with thickness R_p to the radiative flux escaping from optically thin plasma. Unfortunately, this treatment tends to overestimate the NEC. The final objectives of this global work being the determination of the plasma temperature based on a fine description of the spectrum, we chose to calculate the monochromatic emission coefficient of a line according to the "line by line" method[37, 87] since the escape factor does not allow a fine spectral description of the lines.

Assuming the "line by line" method, the main difficulty of the calculation is the determination of the line's profiles. In this work, we took the broadening phenomena resulting from Doppler and pressure effects (Van der Waals broadenings, resonance broadenings, and Stark broadenings) into account. Four types of interaction are considered, which are described by Gaussian and Lorentz profiles.

<u>* *Gaussian profile:*</u> The Doppler broadening is caused by the velocity of emitting atoms and ions relative to the observer. The line shape of Doppler broadening is assimilated to a Gaussian profile, and its full width at half maximum (FWHM), $\Delta\lambda_D$, is given by[88, 89].

$$\Delta\lambda_D = 2\lambda_0 \left(\frac{2k_B T \ln 2}{mc^2}\right)^{1/2} \text{ (nm)} \qquad (2.22)$$

Where m is the atomic weight (e.g. m=9.288×10^{-26} kg for Fe), and λ_0 is the central wavelength of the line (nm).

<u>* *Lorentz profiles:*</u> The pressure broadening, whose profile is Lorentzian as a first approximation[89], is caused by the interaction of an emitting atom with surrounding particles (atoms, irons and electrons). In thermal plasmas, the pressure broadening is due to resonance, van der Waals and Stark effects. The last phenomenon is not awalys considered as a pressure effect, but it is rather as a consequence of an electric field caused by charged particles and product a degeneracy of the energy level of the emiting atom.

The resonance broadening can be characterized by an interaction potential of the atoms (C_3/r^3), where C_3 is a constant characteristic of the radiative transition [30] and r is the distance between the particles. The full width at half maximums (FWHM) of the resonance broadening, $\Delta\lambda_R$, can be expressed in the 4th order approximation[30, 31]

$$\Delta\lambda_R=5.48\cdot\pi\cdot\left(\frac{g_n}{g_m}\right)^{1/2}\cdot\left(\frac{e^2}{4\pi\varepsilon_0}\right)\cdot\left(\frac{f_{nm}}{m_e}\right)\cdot\left(\frac{\lambda_0}{2\pi c}\right)^2\cdot\lambda_0\cdot n_0 \quad \text{(nm)} \qquad (2.23)$$

Where g_n and g_m are the degeneracies of the fundamental and resonant levels, e is the electron charge, ε_0 is the vacuum permittivity, f_{nm} is the oscillator strength of the resonant level, m_e is the electron mass, c is the speed of light and n_0 is the atom density in the fundamental state.

The van der Waals broadening, which is caused by the interaction of an emitting atom with its corresponding ions, is usually described with a Lennard-Jones potential (C_6/r^6), where C_6 is a constant calculated using the hydrogen-like approximation[30]. The FWHM is obtained according to Walkup *et al*[32]:

$$\Delta\lambda_V=8.16\cdot C_6^{2/5}\cdot\bar{v}^{3/5}\cdot n^*\cdot\frac{\lambda_0^2}{2\pi c} \quad \text{(nm)} \qquad (2.24)$$

Where $\bar{v}$ is the mean velocity of the radiating species, and n^* is the population number density of the perturbing particle.

The Stark broadening occurs when an emitting atom is perturbed the electrical field caused by the charged particles. In this case, the interaction is quadratic ($\sim 1/r^4$) and the collision approximation leads to[89, 90]

$$\text{Neutrals: } \Delta\lambda_S=11.37\cdot C_4^{2/3}v_e^{1/3}\cdot n_e\cdot\frac{\lambda_0^2}{2\pi c} \quad \text{(nm)} \qquad (2.25)$$

$$\text{Ions: } \Delta\lambda_S=200.824\cdot C_4^{2/5}\cdot\frac{Z^{4/5}n_e}{T^{1/2}}\cdot\frac{\lambda_0^2}{2\pi c} \quad \text{(nm)} \qquad (2.26)$$

where v_e is the mean speed of the electrons, i.e.

$$v_e=\sqrt{\frac{8k_BT}{\pi m_e}}$$

The Constant of C_4 is calculated taking into account all the lines connected to the lower and upper levels of the lines[89]. The influence of the irons the width is taken into account with the quasi-static method of Griem[59].

The total profile of these three effects is a Lorentzian profile, and the total FWHM, $\Delta\lambda_L$, is given by the sums of individual widths.

** Overall line profile:* The line's profile broadened by various effects is the convolution of a Gaussian function with a Lorenzian function, resulting in a Voigt profile. The analytical form is given by Whiting[91]:

$$P_{ij}^{\text{Voigt}}(\lambda)=\frac{2\ln 2}{\Delta\lambda_{\text{D}}^2}\cdot\frac{\Delta\lambda_{\text{L}}}{\pi^{3/2}}\int_{-\infty}^{+\infty}\frac{\exp\left(-x^2\right)}{\left(\sqrt{\ln 2}\,\frac{\Delta\lambda_{\text{L}}}{\Delta\lambda_{\text{D}}}\right)^2+(x-y)^2}\cdot\text{d}x \qquad (2.27)$$

$$\text{With } y=\frac{2\ln 2}{\Delta\lambda_{\text{D}}^2}\cdot\left(\lambda-\lambda_0\right).$$

2.3.2 Radiation from the atomic continuum

The radiation coming from the atomic continuum is produced by three mechanisms:

<u>* *Radiative attachment:*</u> even if the radiative attachment is often negligible, we nevertheless took into consideration this mechanism due to the presence of negatively charged particles (C^-, O^-, Fe^-) in the plasmas mixtures. Knowing the electronic affinity for the different species (C = 121.9 kJ/mol, O = 141 kJ/mol and Fe = 15 kJ/mol), the monochromatic emission coefficient (J/m3/ster) was calculated according to[92]:

$$\varepsilon_\lambda^{\text{att}}(T)=\left(\frac{2hc}{\lambda^3}\right)\cdot\left(\frac{c}{\lambda^2}\right)\cdot\exp\left(-\frac{hc}{\lambda k_{\text{B}}T}\right)\cdot n_{A^-}(T)\cdot\sigma_{\text{det}}(\lambda) \quad (\text{W. m}^{-3}.\text{sr}^{-1}.\text{ nm}^{-1}) \quad (2.28)$$

where k_{B} is the Boltzmann constant, $n_{A^-}(T)$ is the population number density of the negative charged particles, $\sigma_{\text{det}}(\lambda)$ is the photo-detachment cross section taken from Yachkov for carbon[93] and Robinson and Geltman for oxygen[94]. We did not find data to take into account the attachment of iron.

<u>* *Radiative recombination:*</u> the radiative recombination occurs when an electron and an atomic ion can recombine. This mechanism is often important in the continuum radiation of thermal plasmas. Its calculation requires the knowledge of the Biberman-Schluter factors, which are performed by summing the photoionization cross sections for all the considered energy levels, assuming a Thomas-Fermi shielded potential[95]. For carbon, oxygen and argon species, this factor has been calculated and tabulated by Hofsaess[96]. The corresponding monochromatic emission coefficient is defined by[92, 97]:

$$\varepsilon_\lambda^{\text{rec}}(T)=C_1\cdot\left(\frac{c}{\lambda^2}\right)\cdot\frac{n_{\text{e}}(T)\cdot n_{z^+}(T)}{Q_{z^+}^{\text{int}}(T)}\cdot\frac{Z_{z^+}^2}{\sqrt{T}}\cdot\left[1-\exp\left(-\frac{hc}{\lambda k_{\text{B}}T}\right)\right]\cdot g_1^{z^+}\cdot\xi_\lambda^{(z-1)}(T) \quad (\text{W. m}^{-3}.\text{sr}^{-1}.\text{ nm}^{-1}) \quad (2.29)$$

with

$$C_1=\frac{16\pi\left(e^2/4\pi\varepsilon_0\right)^3}{3c^3\sqrt{6k_{\text{B}}\pi m_e^3}}=5.44436\times10^{-52}\,\text{J.m}^3.\text{K}^{1/2}.\text{sr}^{-1}$$

where $n_e(T)$and $n_{z+}(T)$ are the population number densities of electron and ions respectively, Z_{z+} is the charge of the ion A^{z+}. $Q_{z+}^{int}(T)$ and g_1^{z+} are the internal partition function and the ground level degeneracy of the ion A^{z+} respectively, e is the charge of the electron respectively, ε_0 is the permittivity of vacuum and $\xi_\lambda^{(z-1)}$is Biberman-Schluter factor issued from Hofsaess[96, 98] for argon (Ar, Ar^+), carbon (C, C^+) and oxygen (O, O^+, O^{2+}). As the Biberman-Schluter factor was not available for iron species and multi-charged species (Ar^{2+}, Ar^{3+}, C^{2+}, C^{3+}, O^{3+}), we used the hydrogen-like atoms approximation developed by Okuda *et al*[99].

** Bremsstrahlung:* the bremsstrahlung radiation is produced by the deceleration of an electron due to the deflection by an electric field. The monochromatic emission coefficients for electron-ion and electron-atom interactions are given, respectively, by[10]

$$\varepsilon_\lambda^{ei,z+}(T)=C_1\cdot\left(\frac{c}{\lambda^2}\right)\cdot Z_{z+}^2\frac{n_e(T)\cdot n_{z+}(T)}{\sqrt{T}}\cdot\exp\left(-\frac{hc}{\lambda k_B T}\right)\cdot G_{ei,\lambda}^{z+}(T)\quad (W.\,m^{-3}.sr^{-1}.\,nm^{-1}) \quad (2.30)$$

$$\varepsilon_\lambda^{ea}(T)=C_2\cdot\left(\frac{c}{\lambda^2}\right)\cdot n_a(T)\cdot n_e(T)\cdot T^{3/2}\cdot\exp\left(-\frac{hc}{\lambda k_B T}\right)\cdot G_{ea,\lambda}(T)\quad (W.\,m^{-3}.sr^{-1}.nm^{-1}) \quad (2.31)$$

with

$$C_2=\frac{32}{3c^3}\cdot\left(\frac{e^2}{4\pi\varepsilon_0}\right)\cdot\left(\frac{k_B}{2\pi m_e}\right)^{3/2}=3.4218\times10^{-43}\,J.m.K^{-3/2}.\,sr^{-1}.$$

$n_a(T)$ is the neutral atom number density. For electron-ions interactions, the Gaunt factor $G_{ei,\lambda}^{z+}(T)$ is introduced to correct non-classical behavior using hydrogen-like approximation, and is issued from the table calculated by Grant[100, 101]. For electron-atoms interactions, the factor $G_{ea,\lambda}(T)$ is homogeneous to a surface and depends on the elastic cross-section which is taken from Neynaber *et al*[102] and Robinson and Geltman[94] for carbon and oxygen, and from Tanaka and Lowke[103] for argon.

2.3.3 Radiation from the molecular continuum

The molecular continuum can have an important impact in the surrounding regions where the radiation coming from the hottest regions can be strongly absorbed, especially the UV radiations. Consequently, we included this phenomenon in the calculation assuming its importance for temperatures lower than 10kK for plasmas at

atmospheric pressure. To take into account this radiative process, we have to consider the photodissociation corresponding to the dissociation of a molecule by photon absorption (AB + $h\nu \rightleftarrows$ A +B), the simple photoionisation corresponding to an electron loss by photon absorption $\left(\mathrm{AB} + h\nu \rightleftarrows \mathrm{AB}^{+} + \mathrm{e}^{-}\right)$, and the dissociative photoionisation corresponding to the dissociation of a molecule (AB + $h\nu \rightleftarrows$ A + B^{+} + e^{-}). As it is very difficult to calculate the cross-sections for all the rotational, vibrational or electronic levels, we preferred to use experimental data from the literature. Nevertheless, these data are often obtained in the Standard Temperature Conditions at atmospheric pressure. Based on this report, we applied two assumptions: (1) we only considered the fundamental energy levels which is a good approximation for the low temperatures where the population number densities of the molecules are significant; (2) the cross-sections of the various involved radiative mechanisms were supposed to be independent on the temperature, and only dependent on the wavelength:

$$\varepsilon_{\lambda}^{\mathrm{MC}}(T) = B_{\lambda}(T) \cdot N_{A_2}(T) \cdot \sum_i \sigma_{A_2}(\lambda, 300\mathrm{K}) \cdot \left(1\text{-}\exp\left(-\frac{hc}{\lambda k_{\mathrm{B}} T}\right)\right) \ (\mathrm{W.\,m^{-3}.sr^{-1}.\,nm^{-1}}) \quad (2.32)$$

Where $\varepsilon_{\lambda}^{\mathrm{MC}}(T)$ is the corresponding Molecular Continuum (MC) spectral emission, $B_{\lambda}(T)$ is the Planck function, $N_{A_2}(T)$ the total number density of the molecule A_2 at the temperature T (in $\mathrm{m^{-3}}$) and σ_{A_2} is the total photoabsorption cross-section of the same molecule (in $\mathrm{m^2}$). In this work, we considered the molecules C_2, O_2, CO, CO_2, O_3 already studied in the works of Jan *et al*[104] and Billoux *et al*[38]. All the references used for the photoabsorption cross-sections are reported in the table 2.2.

Table 2.2 refences used for photoabsorption cross-sections of major molecular species.

Molecule	References	Molecule	References
C_2	[105, 106]	O_2	[107]
CO	[108-110]	CO_2	[109, 111, 112]
O_3	[113-116]		

2.3.4 Radiation from the molecular bands

The consideration of the molecular bands in the radiative spectra is an important task of this work since it was rarely included in our previous works[117] except the last

works of Billoux *et al*[38, 118]. Here, we took in consideration the diatomic molecular systems of O_2, CO, CO^+, C_2 and the polyatomic molecular systems of CO_2 and O_3 (listed in table 2.3) even if some of them have a low contribution rate in the plasma composition such as CO^+ or O_3. They have been validated in Air and CO_2 by Babou *et al* (for CO, CO^+, C_2, O_2, CO_2)[119], Chauveau *et al* (for O_2, CO and C_2)[120], Lino Da Silva and Dudeck (for CO)[121], and Laux (for O_2)[88].

Table 2.3. Molecular band systems taken into account in the present work.

Molecule	Electronic system	Electronic Transition	$(v'_{max};v''_{max})$	$\sigma_{0,0}(cm^{-1})$
O_2	Schumann-Runge	$B^3\Sigma_u^- \rightarrow X^3\Sigma_g^-$	(19;21)	49358
CO	Infrared	$X^1\Sigma^+ \rightarrow X^1\Sigma^+$	(49;40)	-
	Fourth Positive	$A^1\Pi \rightarrow X^1\Sigma^+$	(22;35)	64748
	Hopfield-Birge	$B^1\Sigma^+ \rightarrow X^1\Sigma^+$	(2;50)	86916
	Angström	$B^1\Sigma^+ \rightarrow A^1\Pi$	(2;20)	22171
	Third Positive	$b^3\Sigma^+ \rightarrow a^3\Pi$	(2;18)	35358
CO^+	Comet-tail	$A^2\Pi \rightarrow X^2\Sigma^+$	(30;26)	20408
	First negative	$B^2\Sigma^+ \rightarrow X^2\Sigma^+$	(30;35)	45633
	Baldet-Johnson	$B^2\Sigma^+ \rightarrow A^2\Pi$	(30;26)	25226
C_2	Phillips	$A^1\Pi_u \rightarrow X^1\Sigma_g^+$	(35;21)	8268
	Mulliken	$D^1\Sigma_u^+ \rightarrow X^1\Sigma_g^+$	(22;21)	43668
	Deslandres-D'az.	$C^1\Pi_g \rightarrow A^1\Pi_u$	(9;32)	25969
	Ballik-Ramsay	$b^3\Sigma_g^- \rightarrow a^3\Pi_u$	(41;39)	5632
	Swan	$d^3\Pi_g \rightarrow a^3\Pi_u$	(18;33)	19378
	Fox-Herzberg	$e^3\Pi_g \rightarrow a^3\Pi_u$	(15;35)	39806
CO_2	CDSD-4000			
O_3	HITRAN			

* *Diatomic molecular systems:* the emission coefficient of each molecular line between two rotational levels J' and J'' is given by[118]:

$$\varepsilon_\lambda^{MB}(T)=\frac{hc}{4\pi\lambda}\cdot N_{A_2}\left(n',v',K',J',P'\right)\cdot A^{n',v',K',J'}_{n'',v'',K'',J''} \quad \text{(W. m}^{-3}\text{.sr}^{-1}\text{.nm)} \qquad (2.33)$$

where $N_{A_2}\left(n',v',K',J',P'\right)$ is the population number density of the emitting level, $A^{n',v',K',J'}_{n'',v'',K'',J''}$ is the transition probability, $N_{A_2}(T)$ is the number density of the molecule A_2, n' is the electronic level, and v', K', J' and P' are the vibrational, rotational, sub-rotational and symmetry quantum numbers respectively.

The transition probability of a radiative transfer is obtained by the expressions:

$$A_{n'',v'',K'',J''}^{n',v',K',J'} = A_{n'',v''}^{n',v'} \cdot A_{K'',J''}^{K',J'} \tag{2.34}$$

with

$$A_{K'',J''}^{K',J'} = \frac{S_{K'',J''}^{K',J'}}{2J'+1} \tag{2.35}$$

where $A_{n'',v''}^{n',v'}$ is the Einstein coefficient, $A_{K'',J''}^{K',J'}$ is the rotational transition probability and $S_{K'',J''}^{K',J'}$ is the Hönl-London factor calculated by Whiting *et al*[122]:

$$\sum S_{K'',J''}^{K',J'} = \left(2-\delta_{0,\Lambda'}\delta_{0,\Lambda''}\right)\left(2S'+1\right)\left(2J'+1\right) \tag{2.36}$$

$\delta_{0,\Lambda}$ is the Kronecker symbol, whose value is 1 if $\Lambda=0$ and 0 otherwise, $2S'+1$ is the spin multiplicity of the upper electronic state. $\Lambda = |M_L|$ is the quantum number, with value between 0 and L (state $\Sigma(\Lambda=0)$, $\Pi(\Lambda=1)$, $\Delta(\Lambda=2)$).

Concerning the broadenings phenomena of the diatomic lines, we took into consideration Doppler and collisional broadenings. For the Doppler effects, and in the case of molecules, we used the same formula as atomic case (2.22). For collisional broadenings, it is different since we did not have enough information for all the temperature range. Therefore, we systematically used a semi-empirical approximation law to determine the molecular collisional broadenings with a HWHM (Half widths at Half Maximum) γ_L as a function of the pressure P. Depending on the wavelength region, we used the recommendation of Breene[123]:

$$\gamma_L\left(\text{cm}^{-1}\right) = \gamma_0(T_{\text{ref}}) \cdot P \cdot \left(\frac{T_{\text{ref}}}{T}\right)^n \tag{2.37}$$

The relation (2.37) has been validated by Sick *et al*[124], Lewis *et al*[125] and Chauveau[120] for O_2 molecules. The work of Chauveau in air plasmas also indicated the low influence of this approximation on the radiative flux. The relation (2.37) can be applied because of the large broadenings of the molecular bands due to their high population number densities (leading to a less important role for the wings), because of the weak self-absorption of these molecular lines, and because of the strong importance of the Doppler effect in most cases (excepted in the Infrared). Due to these last remarks, we decided to apply it for all the diatomic molecules. We can find that

for visible and near IR (for O_2 SR for example), the values of γ_0, T_{ref} and n are 0.105, 273 and 0.7, respectively[124, 125]; in UV and for molecules in Hitran, their values are 0.265, 295 and 0.66, respectively[126]; in IR, they are 0.053, 296 and 0.75, respectively[127].

** Polyatomic molecular systems:* the radiation of the polyatomic species can be very important in the Infrared region. The radiation coming from CO_2 was calculated using the database CDSD-4000 of Tachkun and Perevelov[128] which seems to be the most complete in the literature with wavenumbers between 226 and 8310 cm^{-1}, and temperatures up to 4000K. As Billoux *et al*[118], we did not consider the radiation of CO_2 for higher temperatures due to a lower contribution to the radiative spectrum. For the O_3 molecule, we used the HITRAN 2012 database[129] even if these molecules are in few concentration in the plasma. The broadenings were described with a Voigt profile and collisional effects were defined by the relation (2.37). This last database gave us two kinds of broadenings: the broadenings parameters due to the perturbation of the species existing in air, and the broadenings parameters corresponding to the perturbation of the molecular energy levels by species of the same type (self-broadenings). As this work is not focused on air plasmas, we considered all the broadening phenomena of a molecular line due to molecules of the same type with a total self-broadening. Under this consideration, we did two strong assumptions, that we supposed not to be so far from the reality: (1) when the molecular species are important in the plasma's composition and the perturbation due to the other species can be neglected; (2) if the previous condition is not respected, all the perturbations caused by the other molecular species can be considered identically even if they are similar (or not) to the perturbed species. The second assumption can be discussed but we supposed that low temperatures tend to increase the molecular species and reduce the impact on the broadening coefficients.

2.3.5 Discretization and integration of the monochromatic emission coefficient

The most rigorous method to describe the spectra is the "line by line" method in order to take into account the broadenings of the atomic and molecular lines. According to previous works using this method[38, 104, 130], we need to find a compromise between a

very fine description and a reduced computing time. Consequently, in this work, we calculated high-resolution spectra with a variable wavelengths step, from 10^6 to 7×10^6 wavelengths, depending on the temperature (more wavelengths are needed at low temperature to take into account the molecular bands). The lines were integrated over ±50nm from the line centre which is sufficient at atmospheric pressure[104, 130] and lead to 0.5% of accuracy in this study compared to an integration on the total wavelength range. The algorithm of Drayson[131] was used to calculate the Voigt profile in order to reduce the computing time. With a station DELL Precision TS810, 3.2Ghz, 32GoRAM, a calculation for a given temperature needs maximum of 90 minutes at atmospheric pressure from 3kK to 30000K with a 100K step (depending on the composition, the temperature and the value of plasma radius R_p).

2.4 Results

2.4.1 Spectra of [82%Ar-18%CO_2]-Fe plasmas

In order to obtain the NEC (or "partial NEC") for [82%Ar-18%CO_2]-Fe plasmas, it is necessary to obtain their spectra prior to integrating them according to Eq. (20). Figures 2.2 (a) and (b) present the total absorption coefficient obtained at 5000K and 1 atm for 82%Ar-18%CO_2 and 95%[82%Ar-18%CO_2]-5%Fe plasmas (molar proportions) respectively, as examples. For the 82%Ar-18%CO_2 plasma, we can observe the presence of the molecular bands and molecular continuum at high wavelengths, and the major role of atomic continuum at low wavelengths. When 5%Fe is added in the plasma, more atomic lines appear in the spectrum due to the presence of numerous and emissive lines of iron.

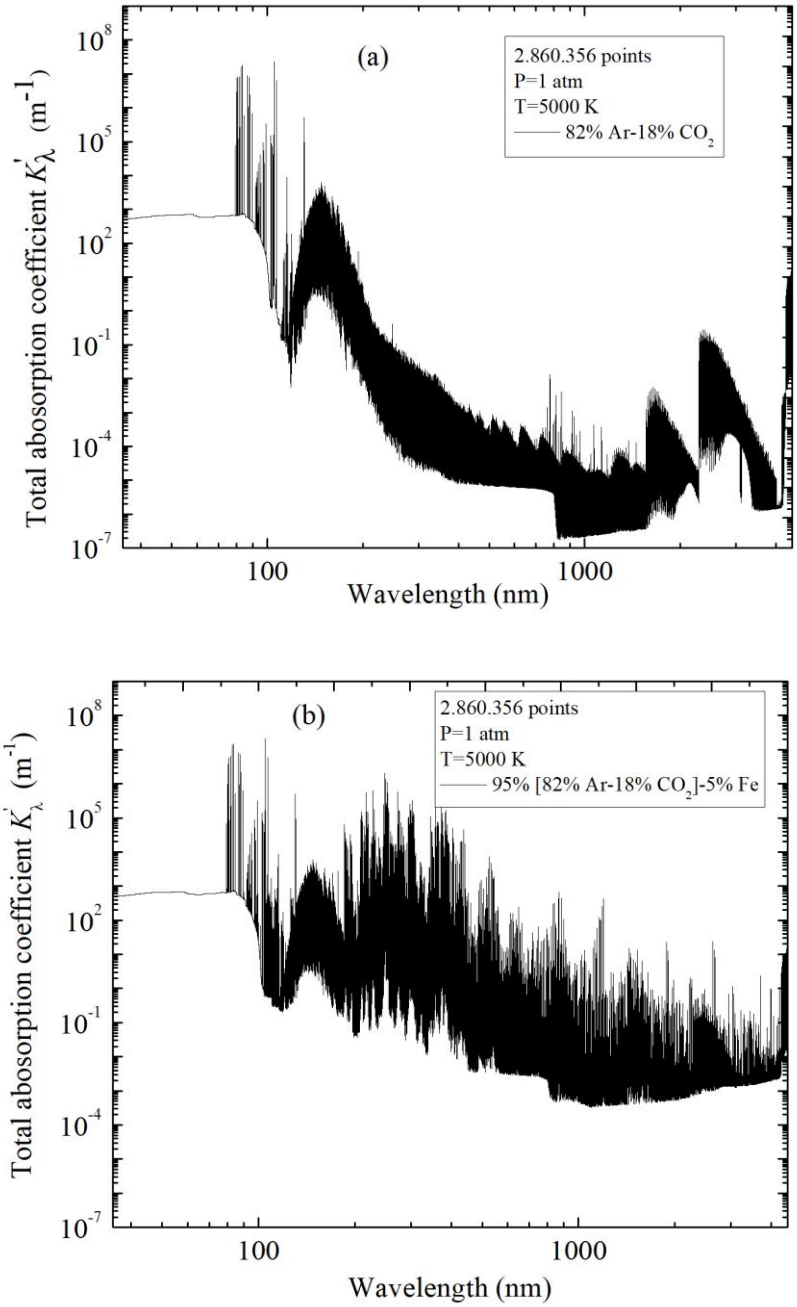

Figure 2.2. Total absorption coefficient at 1 atm and 5000 K for thermal plasmas (a) 82%Ar-18%CO_2 and (b) 95%[82%Ar-18%CO_2]-5%Fe (molar proportions).

2.4.2 Influence of temperature and R_p on the NEC

Figure 2.3 presents NEC values for 82%Ar-18%CO_2 plasma at 1 atm as a function of temperature and plasma radius R_p. The case R_p=0 mm corresponds to an optically thin plasma (without absorption). Below 4 kK, the NEC decreases with the temperature because the CO_2 molecule is the main contributor to the radiation and its number density decreases rapidly due to dissociation. Above 4 kK, the NEC increases with the

temperature because the radiation of CO begins to take effect at low temperatures, and the radiation of the atomic lines for higher temperatures.

The NEC decreases with R_p due to the absorption phenomena and more particularly the absorption of the resonance lines of the atomic species (this phenomenon is more pronounced in presence of iron). The absorption is very important in the first millimeter. For the plasma with a radius of R_p=1 mm, 91.5% of the total absorption is achieved for 1mm at 10 kK. Nevertheless, the absorption phenomenon is weak at very low temperature because the plasma is dominated by the molecular species and their radiation is weakly absorbed. These conclusions are the same for other mixtures with and without metallic vapours.

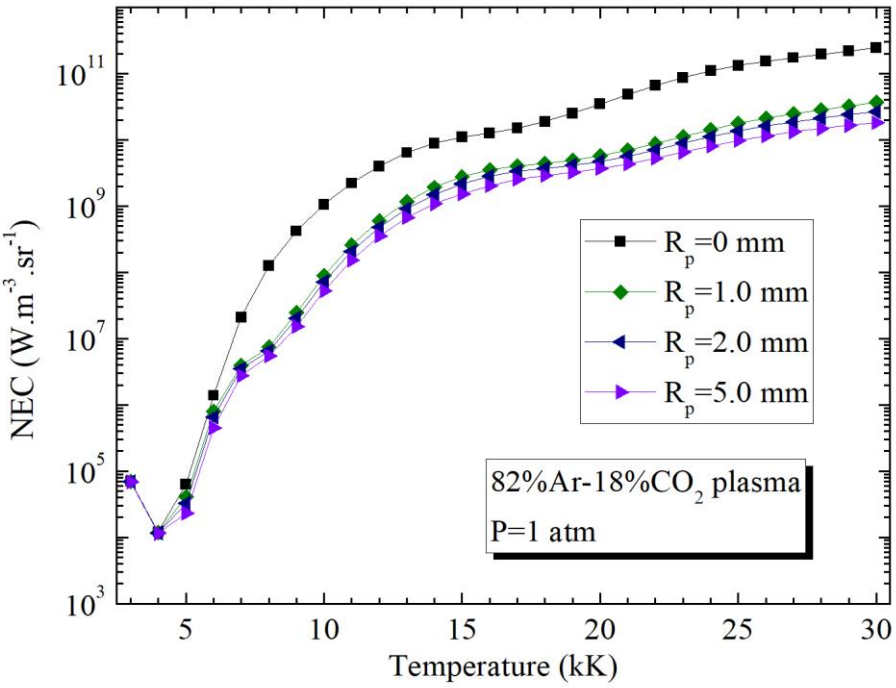

Figure 2.3. Influence of the plasma radius R_p on the NEC for 82%Ar-18%CO_2 mixture (molar proportion) at atmospheric pressure.

2.4.3 Influence of vapour concentration on the NEC

Figure 2.4 highlights the influence of vapours concentration on the NEC for R_p=1mm and [82%Ar-18%CO_2]-Fe plasmas. As it can be seen, it is evident that the strong influence of iron on the NEC occurs with a very low concentration especially at low temperature. This is caused by two phenomena: the increase of the electron number density because of the low ionisation potential of neutral iron compared to Ar, C, and O

(7.902 eV, 15.760 eV, 11.260 eV, 13.618 eV for Fe, Ar, C and O respectively); the rich spectrum of the atomic lines of neutral iron (more specifically, the resonance lines which are strongly emissive but also strongly absorbed). Similar behaviour has also been observed for other plasmas with iron vapour, for example Ar-Fe mixture[10].

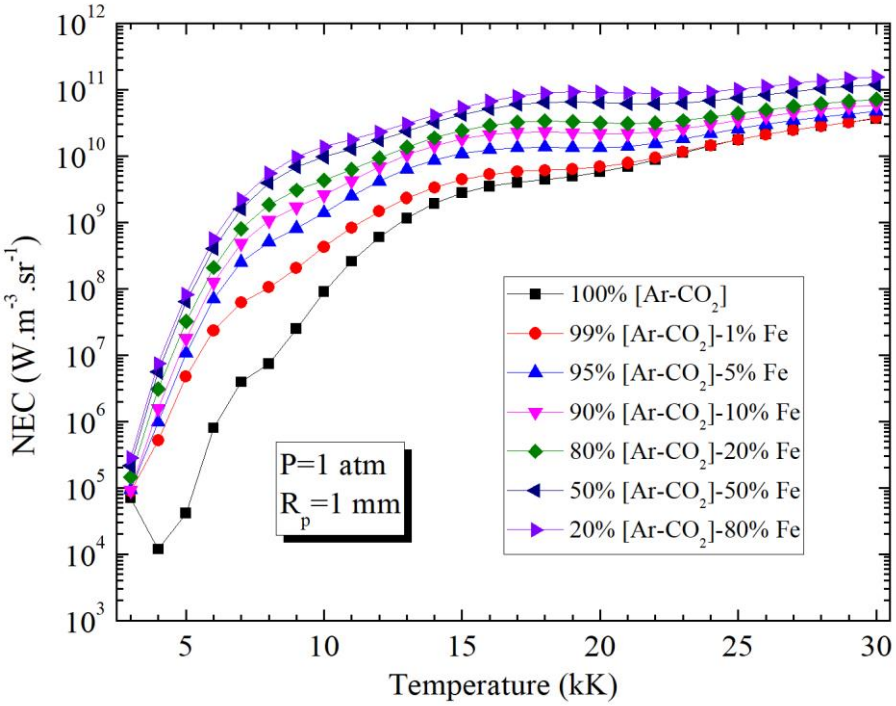

Figure 2.4. Influence of the iron vapour on the NEC for [82%Ar-18%CO_2]- Fe mixtures (molar proportions) at atmospheric pressure and R_p=1 mm.

2.4.4 Influence of the different contributions to the total radiation

For a better understanding of the influence of various radiative mechanisms, the contributions of atomic lines, continuum (atomic continuum and molecular continuum) and molecular bands to the NEC are presented in figure 2.5 for [82%Ar-18%CO_2]-Fe plasmas without iron vapours and with an iron fraction of 5% (R_p=1 mm, P=1 atm). In a previous works of the Laplace laboratory [28], we defined the spectral intervals for experiments by dividing the emission of the lines by the emission of the continuum in a specific spectral interval where the emission of the continuum did not really vary. Hence, it is important to know the variation of the different contributions to see the most important contributions as a function of the temperature range. It is also the occasion to valid our assumptions: the radiation for the molecules cannot be neglected at low temperatures for Ar-CO_2 plasmas.

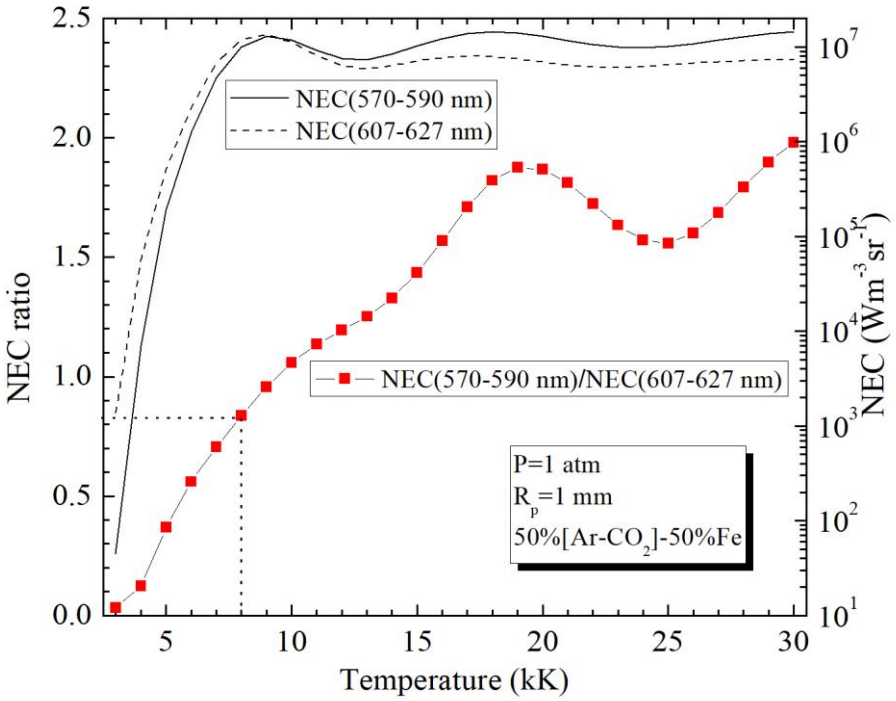

Figure 2.5. Contribution of the different radiative processes to the NEC for 82%Ar-18CO_2 and 95%[82%Ar-18CO_2]-5%Fe plasmas (molar proportions) at 0.1MPa and R_p=1 mm.

For the 82%Ar-18%CO_2 plasma, we see that the radiation of molecular bands is the dominant contributor (>97%) to the NEC below 6 kK, and it shares the NEC with lines and continuum till 10 kK with more than 50% at 7.5 kK. The radiation of the molecular bands is mainly produced by the CO_2 system for temperatures below 4 kK, CO IR for temperatures between 3.5kK and 5kK, and 4th CO for higher temperatures. When temperatures exceed 10 kK, the radiation of molecular bands becomes negligible, and the radiation of lines plays a leading role in the NEC while the continuum radiation also takes a considerable proportion, especially between 14 KK and 18 kK accounting for above 30%.

When the plasma contains a low concentration of iron (e.g. 5% Fe in this case), the radiation of the atomic lines is the most important part (>89%) for the total temperature range. This is because the intense radiation of iron lines drastically minimizes the influence of molecular bands and continuum.

2.4.5 NECs for certain spectral intervals

Because the NEC depends on the temperature T and the concentration of vapours Y_{Fe} for a given plasma size, it is possible to diagnose the T and Y_{Fe} in MAG arcs (with [82%Ar-18%CO_2]-Fe plasmas) based on the NEC. Since the experimental

instruments (CCD cameras) can only detect the radiation within certain spectral intervals (e.g. visible light), we actually need to find the NEC of spectral intervals (or "partial NEC"). By comparing the measured values with the theoretical ones, we can determine the T and Y_{Fe} in the arc. The theoretical determination of the spectral intervals can thus help us to perform diagnostics.

Let us consider the spectral intervals (570-590 nm) and (607-627 nm) for a 50%[82%Ar-18%CO_2]-50%Fe mixture at 0.1MPa and R_p=1mm. Figure 2.6 shows their corresponding NECs and the ratio of these two partial NECs. For a given position in the MAG arc where the NEC(570-590 nm) and NEC(607-627 nm) measured are 1.00×10^6 $Wm^{-3}sr^{-1}$ and 1.20×10^6 $Wm^{-3}sr^{-1}$ respectively (these values corresponding to the plasma with 50% Fe), we can observe that the ratio 0.836 corresponds to a temperature of 8 kK.

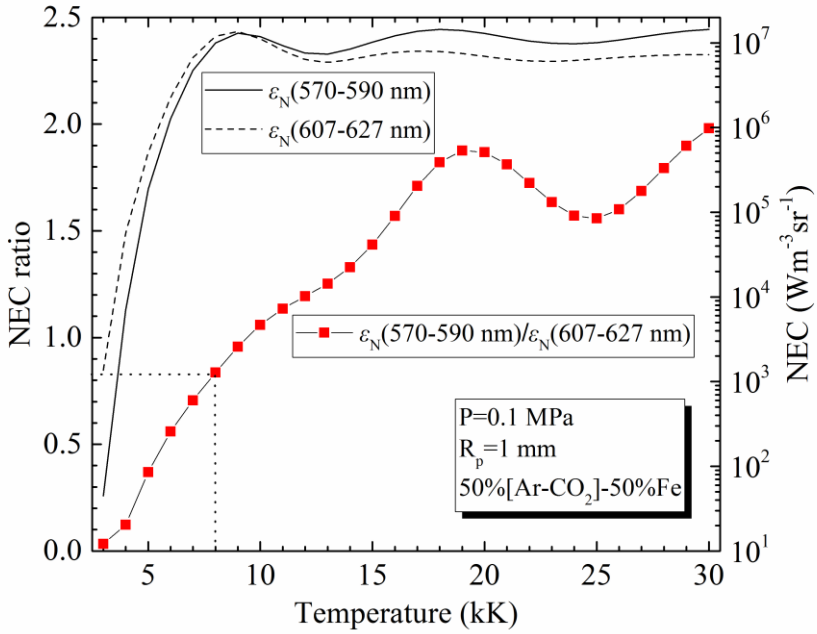

Figure 2.6. Net emission coefficients of the spectral intervals of 570-590 nm (line) and 607-627 nm (dash) and their emissivity ratio (line-square) at 1 atm and R_p=1 mm.

This method depends on the NECs of some certain spectral intervals, and thus the choice of the spectral intervals is a key issue. Since two parameters (T and Y_{Fe}) are expected to be solved, at least two spectral intervals are needed. The NECs of ideal intervals should be sensitive to the variation of the temperature and iron concentration. Also, the radiation in these spectral intervals must be weakly absorbed. This chapter focuses on the calculation of radiative properties of the [Ar-CO_2]-Fe plasmas and demonstrates its radiative characteristics, while Chapter 4 will be devoted to find two

ideal spectral intervals ($\Delta\lambda_1$ and $\Delta\lambda_2$) and to diagnose a pulsed MAG arcs according to $\varepsilon_{\Delta\lambda_1}(T,Y_{\mathrm{Fe}})$ and $\varepsilon_{\Delta\lambda_1}(T,Y_{\mathrm{Fe}})/\varepsilon_{\Delta\lambda_2}(T,Y_{\mathrm{Fe}})$.

2.5 Conclusion

This chapter is devoted to the determination of the radiative properties in the temperature range 3-30 kK at 1 atm for [82%Ar-18%CO_2]-Fe plasmas representative of MAG arcs. The spectra and the NEC were obtained by considering all radiative mechanisms. It has been demonstrated that for the 82%Ar-18%CO_2 plasma the radiation of molecular bands is important at low temperature (T<10 kK) and not self-absorbed in the plasma. At higher temperature, atomic lines contribute most to the radiation in spite of strong absorption, while the continuum radiation also assumes a considerable proportion. When a low iron concentration (e.g. 5%) exists in the plasma, the NEC is dramatically increased especially at low temperature. Atomic lines become the dominant contribution, thus causing continuum and molecular bands insignificant.

This study mainly presents the entire spectra and corresponding NEC for [82%Ar-18%CO_2]-Fe plasmas. It builds a foundation for the diagnostics of temperature and iron concentration in MAG arcs (chapter 4), which is based on the relation of the NEC of some particular spectral intervals, on temperature and iron concentration profiles, and on the use of a CCD camera with narrow-band filters.

Chapter 3 Spectroscopic investigation of pulsed MAG arc

The new diagnostic method studied in chapter 4 is based on the assumption that the plasmas is in local thermodynamic equilibrium (LTE). Many spectroscopic methods, e.g. Boltzmann plot method[132], have been used to diagnose GMAW arcs in previous work[23, 24, 28], under the assumption of LTE. However, few works are dedicated to its validation and none is focused on the case of MAG-P welding. Hence, the spectroscopic investigation of the thermodynamics state in a typical MAG-P arc ([82%Ar-18%CO_2]-Fe plasmas) is presented in this chapter.

In this case, the excitation temperature was obtained with Boltzmann plot method while the Stark broadening measurement was performed with iron and argon lines to get electron temperature and density. LTE hypothesis validity across the arc is discussed considering the agreement between the two temperatures, the electron density and iron concentration. Results show supporting evidence for the main part of the plasma, which facilitates the use of the new diagnostic method. Besides, the results of plasma temperature and iron concentration obtained provide comparative material for the new diagnostic method.

3.1 Diagnostic methods

3.1.1 Temperture measuments

** Boltzmann plot method:* In LTE, the plasma temperature (precisely, the excitation temperature) can be determined by the Boltzmann plot method, which has been used for the diagnostics of arc plasmas, such as MIG arcs[10, 12, 24] and free-burning arcs[25]. When LTE exists, the excitation temperature is equal to the electron temperature, and the population number density of the excited states follows a Boltzmann distribution. For the same atom in different energy level, the emissivities of the spectral lines conform to the relation [19]:

$$\ln\left(\frac{\varepsilon_{ul}\lambda_{ul}}{A_{ul}g_u}\right)=-\left(\frac{E_u}{k_{\mathrm{B}}T_{\mathrm{exc}}}\right)+C, \tag{3.1}$$

where T_{exc} is the excitation temperature, A_{ul} is the probability (s^{-1}) corresponding to

the transition from upper lever u to lower level l, ε_{ul} is the emissivity ($W.m^{-3}.sr^{-1}$) of the transitions, λ_{ul} is the transition wavelength, E_u and g_u are the energy level (eV) and the statistical weight of level u, respectively, k_B is the Boltzmann constant and C is a constant for a fixed temperature T_{exc}. The left term of the equation is called a Boltzmann function. By plotting the Boltzmann function for different energy E_u in a figure, one can deduce the excitation temperature T_{exc} from the slope of the line $(-1/k_B T_{exc})$.

Table 3.1. Spectroscopic data of iron lines used for the Boltzmann plot method[26].

Wavelength (nm)	A_{ul} (10^6 s^{-1})	Accuracy on A_{ul}	E_l (ev)	E_u (ev)	g_u
524.25	2.38E+06	≤ 18%	3.634	5.999	11
527.32	8.12E+06	≤ 18%	3.292	5.642	3
530.23	9.04E+06	≤ 18%	3.283	5.621	5
532.42	2.06E+07	≤ 18%	3.211	5.539	9
532.80	1.15E+06	≤ 7%	0.915	3.241	7
537.15	1.05E+06	≤ 7%	0.958	3.266	5
539.32	4.91E+06	≤ 18%	3.241	5.539	9
539.71	2.58E+05	≤ 7%	0.915	3.211	9

In this work, a very high current (500A) is adopted, which means a large amount of iron vapour would be evaporated from the electrodes and enter into the arc. Due to strong radiation of iron, tiny amounts of iron vapour can be detected by spectroscopy [10]. Here, eight Fe I lines with strong emissivities and wide energy ranges were used as diagnostic lines, as list in table 3.1. The error of the excitation temperature from the Boltzmann plot method is given by[12]:

$$\frac{\Delta T_{exc}}{T_{exc}} = \frac{k_B T_{exc}}{\left[\sum_{k=1}^{8} E_{uk}^2 - \frac{1}{8}\left(\sum_{k=1}^{8} E_{uk}\right)^2\right]^{1/2}} \times \left(\frac{\Delta \varepsilon_{ul}}{\varepsilon_{ul}} + \frac{\Delta A_{ul}}{A_{ul}}\right). \qquad (3.2)$$

The term in right bracket considers the upper energy E_{uk} of the eight spectral lines, which gives a value of $2.60\times10^{-5} T_{exc}$. The term in parentheses is the error of emissivities ε_{ul}, which is caused by the limited measuring reproducibility and the Abel inversion; the ε_{ul} error due to the reproducibility in measurement is less than 10% by carefully examining the measured data, and the error resulted from the Abel inversion due to the smoothing of the radiance is estimated to be 15% following Rouffet *et al*[12]. The second term in parentheses corresponds to the error caused by the uncertainty of

the transition probability A_{ul}, which is issued from NIST database [26]. Considering the upper limit of the accuracies in table 3.1, the error of A_{ul} was assumed to be 18%. As a consequence, the maximum temperature error $\Delta T_{exc}/T_{exc}$ in (3.2) is equal to be $1.12\times10^{-5}T_{exc}$, e.g. $\Delta T_{exc}/T_{exc}$= 11.20% (or ΔT_{exc}=1120 K) at 10000 K. The error is acceptable for this measurement.

** Stark broadening method:* For thermal plasmas, a spectral line has a definite width—line broadening, which can be measured using a high-resolution spectrometer. Torres *et al*[27] proposed a method yielding to both electron temperature and density, using the measurement of two different spectral Stark broadening lines. The lines of Ar I at 696.5 nm and Fe I at 538.3 nm were adopted in this study due to the fact that they are strongly broadened, well isolated and non-absorbed, and that they have been already used to investigate MIG arcs[10-12, 23, 28, 29].

For these two lines, their FWHMs of the Stark broadening (in nm) depend on the electron temperature T_e (K) and the electron density n_e (m^{-3})[33-35]:

$$\Delta\lambda_S^{Fe,\,538.3}=0.2648_{(\pm0.0123)}\frac{n_e}{10^{23}}\left(\frac{T_e}{13000}\right)^{1.670_{(\pm0.2098)}}\ (nm) \tag{3.5}$$

$$\Delta\lambda_S^{Ar,\,696.5}=0.0814_{(\pm0.0041)}\frac{n_e}{10^{23}}\left(\frac{T_e}{13000}\right)^{0.3685}\ (nm) \tag{3.6}$$

At atmospheric pressure and temperatures usually found in GMAW arcs (around 10000 K), the Stark broadening is prevailing in other. We estimated the broadenings for atmospheric plasmas ([82%Ar-18%CO_2]-Fe mixtures at 10000 K) in the case of a low concentration of iron (Y_{Fe}=10% by mole) and a high concentration of iron (Y_{Fe}=90% by mole), as shown in table 3.2. It is found that the stark broadening is the predominating broadening source, especially for mixtures with high iron concentrations.

Table 3.2. FWHMs of the spectral lines of Ar I (696.5 nm) and Fe I (538.3) nm at 10 kK and 1atm.

Spectral line	Y_{Fe} (mole %)	FWHM, $\Delta\lambda$ (nm)			
		$\Delta\lambda_R$	$\Delta\lambda_V$	$\Delta\lambda_S$	$\Delta\lambda_D$
Fe I 538.3 nm	10%	1.93E-3	4.33E-7	9.74E-2	5.15E-3
	90%	2.20E-5	3.33E-4	4.60E-1	5.15E-3
Ar I 696.5 nm	10%	~0	9.33E-4	4.21E-2	7.89E-3
	90%	~0	1.83E-3	1.99E-1	7.89E-3

Therefore, in this study we assume that the convolution of all to the measured line broadenings can be approximated by only Stark broadening; as already done in the diagnostics of some welding arc plasmas[24]. Then the simultaneous solution of the Stark broadenings (given in (3.4) and (3.5)) allows us to obtain the electron temperature T_e and the electron density n_e[29]:

$$T_e = 13000 \cdot \left(0.3074_{(\pm 0.0298)} \times \frac{\Delta\lambda_S^{Fe,538.3}}{\Delta\lambda_S^{Ar,696.5}}\right)^{0.7683_{(\pm 0.1239)}} \quad (K) \qquad (3.8)$$

$$n_e = \Delta\lambda_S^{Ar,696.5} \frac{10^{23}}{0.0814_{(\pm 0.0041)}} \left(\frac{T_e}{13000}\right)^{-0.3685} (m^{-3}) \qquad (3.9)$$

It should be noted, however, that the T_e and n_e errors originate from not only the accuracy of the relations (i.e. ± error in (3.7) and (3.8)) but also the accuracies of $\Delta\lambda_S^{Fe,538.3}/\Delta\lambda_S^{Ar,696.5}$ and $\Delta\lambda_S^{Ar,696.5}$, which mainly result from the reproducibility in measurement. By carefully examining our multi-group experimental results (section 3.2), we found uncertainties for $\Delta\lambda_{Ar,696.5}^S$ and $\Delta\lambda_{Fe,538.3}^S$ close to be 5% and uncertainty for $\Delta\lambda_{Fe,538.3}^S/\Delta\lambda_{Ar,696.5}^S$ close to 4%.

As a consequence, the electron temperature T_e and the electron density n_e can be deduced from the $\Delta\lambda_S^{Ar,696.5}$ and $\Delta\lambda_S^{Fe,538.3}$ measured according to (3.7) and (3.8). For example, given that $\Delta\lambda_S^{Ar,696.5}$ and $\Delta\lambda_S^{Fe,538.3}$ are 0.158 nm and 0.319 nm respectively, T_e is deduced to be (9000±1500) K and n_e to be $(2.2\pm0.4)\times10^{23}$ m^{-3}.

3.1.2 Iron vapour concentration calculations

Since the presence of iron vapour can seriously affect plasma properties, it is important to determine the iron concentration for the MAG arc. Under LTE, the iron concentration Y_{Fe} can be determined from the electron temperature T_e and the electron density n_e based on the plasma composition; it has been performed for a MIG arc (Ar-Fe plasmas) by Roufet *et al* [12]. Assuming our plasmas in LTE state, we applied a similar approacdh to determine the iron concentrations in the MAG arc ([Ar-CO_2]-Fe plasmas).

The equilibrium compositions of [82%Ar-18%CO_2]-Fe plasmas with several iron concentrations were obtained by computation. Figure 3.1 shows the plasma composition for a 90% [Ar-CO_2]-10% Fe mixture (by mole) at 1 atm, as an example. Below 9000 K, the electrical neutrality is achieved by electrons and Fe^+ ions. Thus,

the presence of iron vapour is responsible for the increase of electron density at low temperatures, due to its low ionization energy (7.902 eV) compared with those of the others atoms (11.260 eV, 13.618 eV and 15.760 eV for C, O and Ar respectively). As the temperature rises, the electron density continues to increase and reaches a maximum at 15kK.

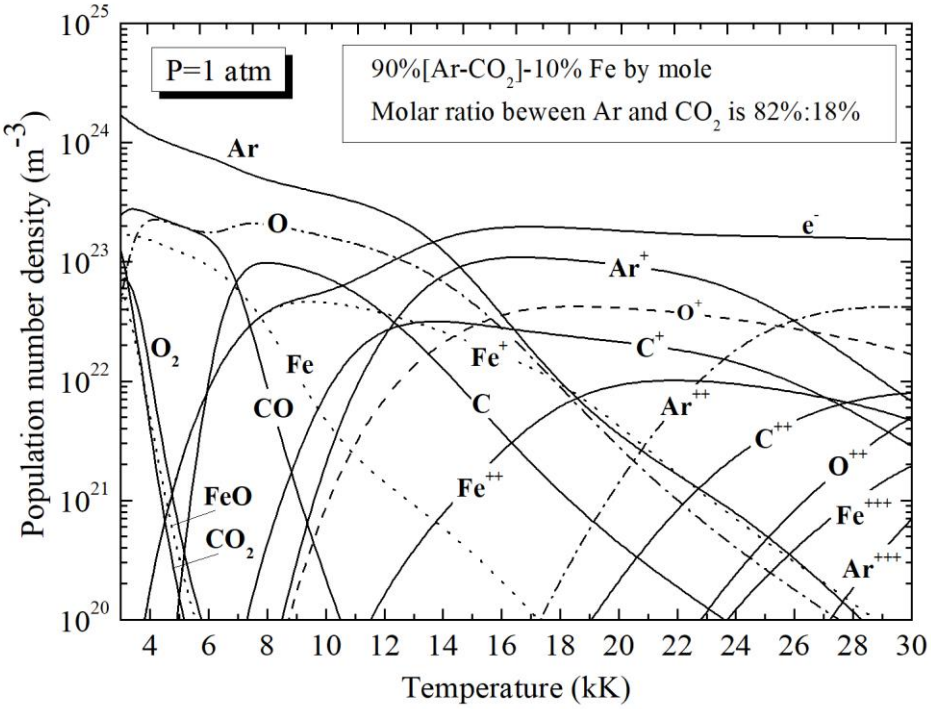

Figure 3.1. plasma composition of a 90%[Ar-CO_2]-10%Fe plasma (by mole) at 1 atm.

The relations of the electron density and the temperature can be obtained for the [Ar-CO_2]-Fe plasmas with several of iron content, as shown in figure 3.2. It can be seen that at a given temperature the electron density increases with the iron content, and the variation is very obvious in the temperature range of 7-15 kK. Given/Knowing the electron density and the temperature, the iron mole concentration can be obtained from figure 3.2. For example, if the electron density and the temperature are measured to be 1.8×10^{23} m^{-3} and 10 kK, respectively, the iron content is estimated to be 50% by mole. It should be noted, however, that this method applies only to the plasmas in LTE, since the computation of the plasmas composition is based on LTE.

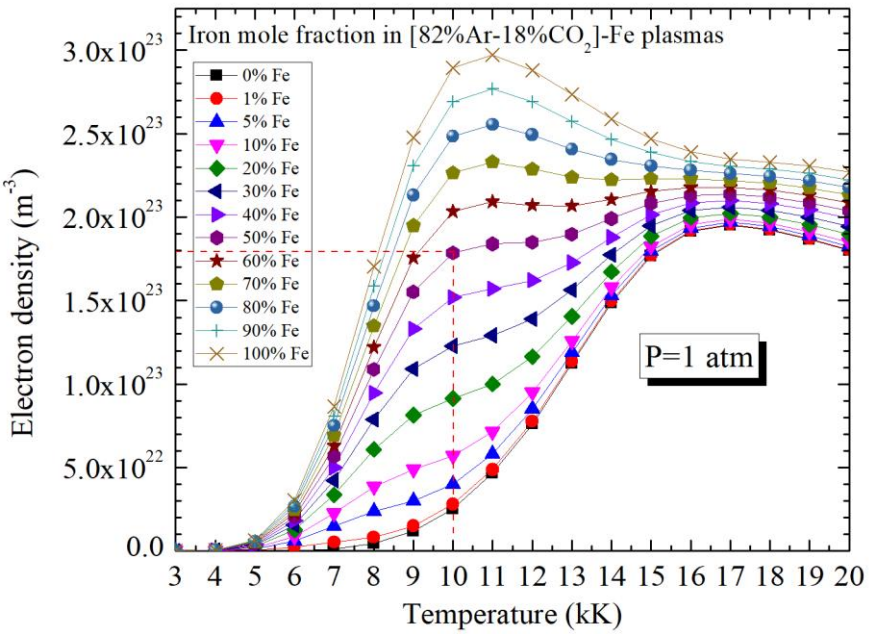

Figure 3.2. Relations between the electron density and the temperature for [82%Ar-18%CO_2]- Fe plasmas for various of iron fractions (by mole) at 0.1MPa.

3.2 Experimental setup and diagnostic procedure

We explored a pulsed MAG arc in one drop per pulse (ODDP) mode by the experimental setup shown in figure 3.3. The ODDP mode, which is characterized by a stable, periodical and controllable metal transfer to the workpiece[4, 5], is achived by using a pulsed current. Due to its good performance, the pulsed MAG welding (MAG-P welding) has been favoured in industry. The experimental setup is composed of five parts: the welding system, the high-speed camera, the electrical signal acquisition device, the spectrometer and the control system (the computer and the trigger device). They are described in forthcoming paragraphs.

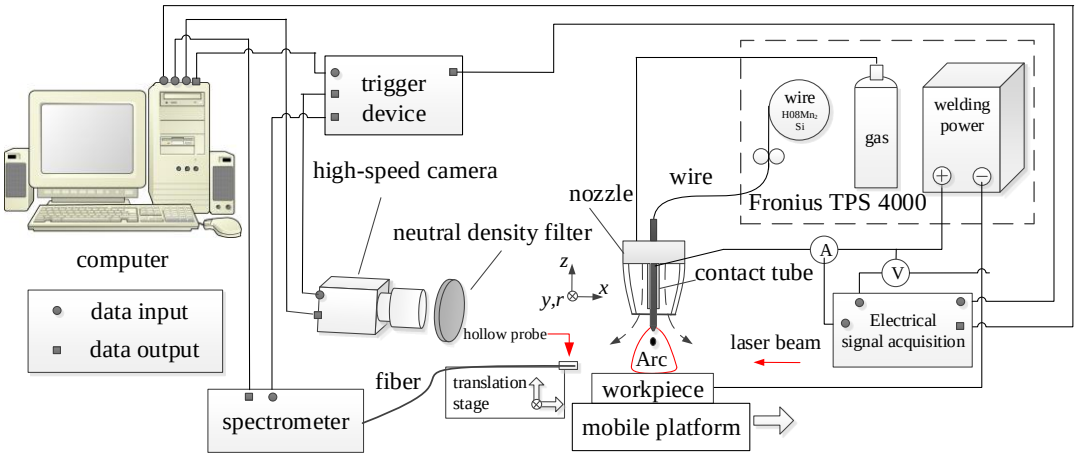

Figure 3.3. Experimental setup.

3.2.1 Welding process.

The MAG welding process is operated by a welding system (figure 3.3). An arc created by a welding power (Fronius TPS 4000) is struck between a H08Mn2Si steel wire (anode) and a Q235A steel workpiece (cathode) in the shielding gas of 82%Ar-18% CO_2 mixture (by mole) with a gas flow of 20 L/min. The wire, 1.2mm in diameter, is continually fed with a rate of 3 m/min. The workpiece, 10 mm in thick, is moved along with a mobile platform at a velocity of 0.5 m/min in *x* direction. The welding wire and workpiece consist chiefly of iron, which are chosen due to their versatility, hardness and low cost; their chemical components are listed in table 3.4. A contact tube is vertically fixed at 20 mm above the workpiece. The arc is assumed to be axisymmetric in the plane perpendicular to the arc axis, considering the pulsed current (500 A) is large; this assumption has been widely accepted in the measurements of GMAW arcs [24].

Table 3.4. Chemical compositions (mass %) of the workpiece and the wire.

	Fe	C	Mn	Si	P	S	Cr	Ni	Cu
$H08Mn_2Si$	>95.8	≤0.11	1.8-2.10	0.65-0.95	≤0.025	≤0.015	≤0.20	≤0.30	≤0.50
Q235A	>98.7	0.14-0.22	0.30-0.65	≤0.30	≤0.05	≤0.045			

A high-speed camera (PHOTRON FASTCAM Super 10KC; 3000 frames/s) associated to a neutral density filter is used to obtain the arc images. The shadowgraph technique using strong luminous backlight is adopted to visualize the droplets, which helps to adjust welding parameters (such as welding current and pulse frequency) to

achieve an ODPP droplet transfer. Also, the arc images allow us to find appropriate diagnostic positions for the spectroscopic investigation.

An electrical signal acquisition device is used to measure the welding current and voltage. The current is probed by a Hall element sensor (AHKC-KA, ACREL), with an accuracy of 0.5%. The voltage is probed by a differential voltage sensor (CHV-100, YUBO), with an accuracy of 0.6%. These signals are collected by a data acquisition card (PCL-818L, ADVANTECH) with a response time of 0.8μs and then converted to real current and voltage values by a self-compiling LabVIEW program [37]. The electrical measurements and the photo shoots are synchronously performed with a trigger device under the control of the computer.

A periodically steady welding process is necessary for the measurement of the arc. By adjusting welding parameters, an ideal ODDP can be achieved by the Fronius TPS 4000 welding machine. During the welding process, one droplet transfers per pulse and the arc behavior in different pulses is almost the same. Figure 3.4 presents the current and voltage curves together with the arc images in one pulse cycle (10.5 ms). A typical ODDP can be observed: the pulse starts with the high-current phase (P_1). The P_1 period took 900 μs, with almost constant current (500A) and voltage (39 V). The wire is gradually melted at its tip during this period, accompanied by a luminous arc. During the detachment phase (P_2), the current slowly decreases to 60 A and a droplet, which is slightly smaller than the wire diameter, detaches from the wire tip and fell across the arc. During the base-current phase (P_3), the current keeps constant to 30 A, and no droplet is formed.

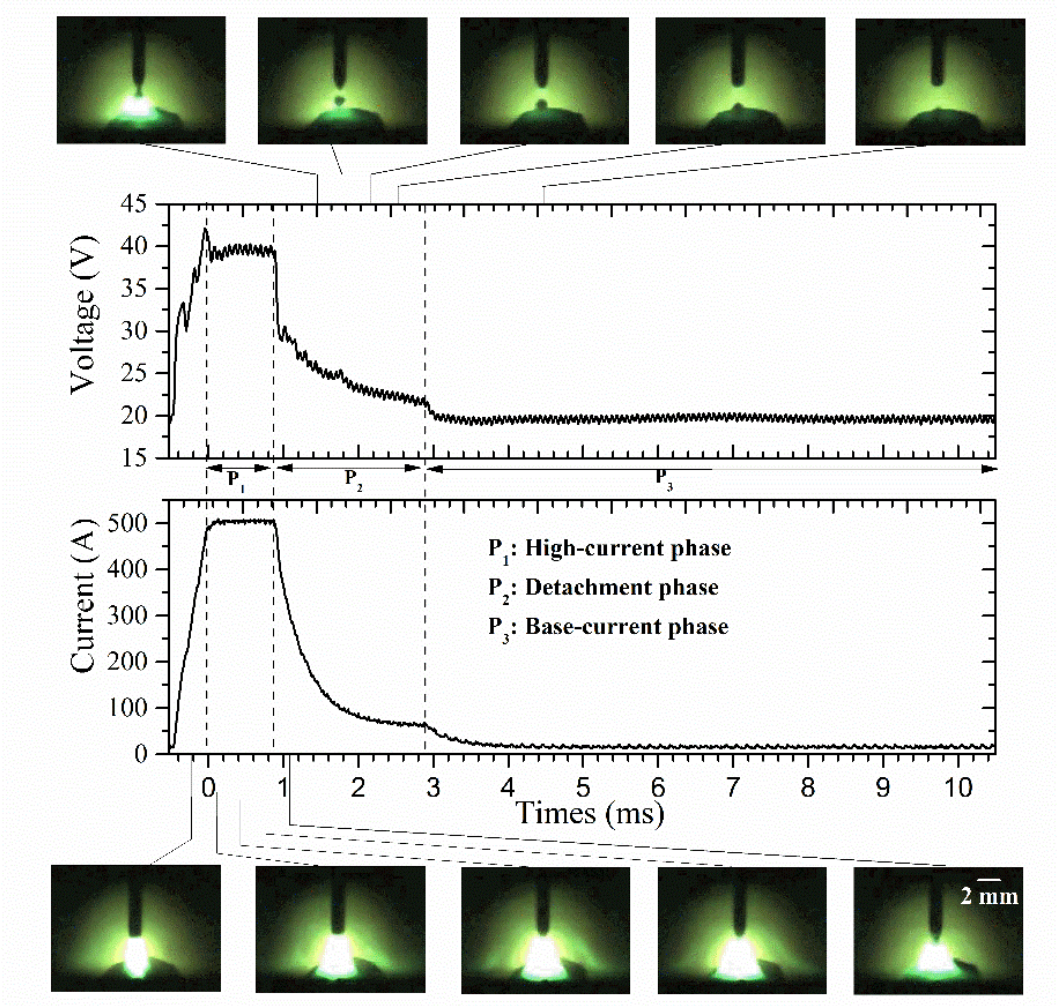

Figure 3.4. Electrical signals and the arc images measured during one pulse period.

3.2.2 Spectroscopic diagnostics.

A spectrometer (AvaSpec-2048) with a wavelength resolution of 0.016 nm and a sampling frequency of 2000 times/s is used to explore the plasma radiation. For simplification, we only investigate the arc at 450 μs, which corresponds to the middle time of the high-current pulse P_1. To find proper diagnostic positions, we took a photo of the arc using the high-speed camera (no backlight) as shown in figure 3.5 for an arc with a length of about 3 mm. Three representative layers are investigated laterally by the spectrometer: z=0.5 mm (near the workpiece), z=1.5 mm (middle of the arc) and z=2.5 mm (near the wire), where z is the desistance above the workpiece. For the three layers above, the diagnostic space ranges are y= (-4, 4) mm, y= (-3.5, 3.5) mm and y= (-3, 3) mm respectively, with a space interval of 0.5 mm as indicated in figure 3.3.

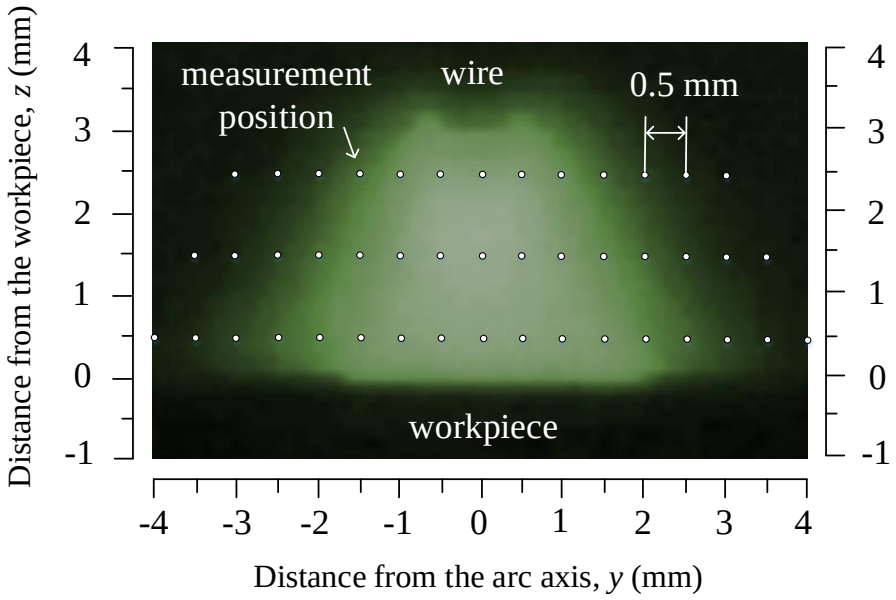

Figure 3.5. Image of the pulsed arc at t=450 μs (no backlight; 3000 frames/s).

The duration of a pulse peak in this welding process is 900 μs, while the resolution of the spectrometer is only 500 μs/time. Hence, it is impossible to record several moments in one pulse peak by this spectrometer. To obtain the spectroscopic data at the expected moment (t=450 μs), a trigger device is used to achieve the synchronous acquisition of spectroscopic information, electrical signals and arc images (Figure 3.3). Because the electrical signal collection has a high resolution (0.8 μs), it can calibrate the time for the spectroscopic measure, and thus the spectroscopic data at t=450μs in different pulse circles can be identified.

In addition, the spectroscopic measure requires a high special resolution due to the small size of the arc. Hence, a high-precision 3D mobile platform, which can achieve a precise displacement, is used to fix the fibre of the spectrometer. Also, a laser beam is used to locate the absolute position of spectroscopic diagnostics. Nevertheless, it is still hard to ensure the consistency of arc in each measurement, e.g. a slight fluctuation of the arc in shape, position or length may occur. This problem can be solved by the arc images shot by the high-speed camera. Because the arc images are collected at the same time with the spectroscopic and electrical acquisition, we can identify ideal welding process from the arc images and then find corresponding spectroscopic data. In practice, for one position many measurements are performed until one expected arc appears, and the corresponding spectroscopic measurement is chosen for the arc diagnostics. Additionally, since the fibre may block the line of sight

of the high-speed camera, the camera is placed in face of the arc with a small slope of about 10°, as shown in figure 3.3.

For one diagnostic position, five sets of spectroscopic data that corresponds to the moment *t*=450μs were chosen and averaged in this study. Figure 6 shows the spectra measured laterally for the position of *z*=1.5 mm and *y*=0 mm as an example, with the diagnostic lines highlighted. It can be seen that although these spectra were taken from five different pulses, they almost overlap. It indicates that the spectral data at t=450μs are of good quality and that it is possible to diagnose precisely one expected moment and position based on the calibration of electrical signals and the selection of arc images.

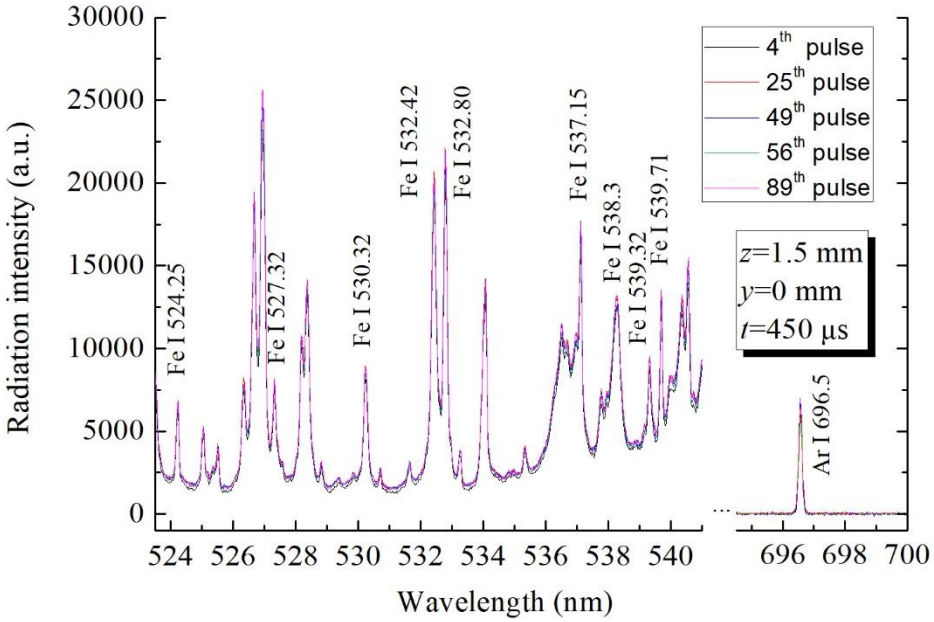

Figure 3.6. Spectra obtained laterally for a position at *z*=1.5 mm and *y*=0 mm at *t*=450μs in five selected pulse circles.

The lateral spectra recorded at different positions (*z*, *y*) are then transformed to spectra with radial distributions at positions (*z*, *r*) using an Abel inversion. The Abel inversion algorithm used in present work is similar with that in [38]. The emissivities of the Fe I lines needed for the Boltzmann plot method are obtained from the spectra. Also, the line broadenings of Fe I (538.3 mm) and Ar I (696.5 nm) required for the Stark broadening method are obtained by a Lorentz line fit [38].

The excitation temperature is then deduced by the Boltzmann plot analysis of the 8 Fe I lines, as described in section 2.1. Figure 3.7 shows the excitation temperature for a position z=1.5 mm above the workpiece and r=0mm (arc axis), as an example. The linear fit is made with the least square method [39]. The slope of the line obtained is -1.234, which corresponds to the excitation temperature T= 9404.4 K. For the same position, the measured FWHMs of Fe I (538.3 nm) and Ar I (696.54nm) lines are 0.319 nm and 0.158 nm respectively, resulting in electron temperature of T_e= 9011.1 K and electron density of n_e=2.22×10^{23} m^{-3} according to section 3.2.2.

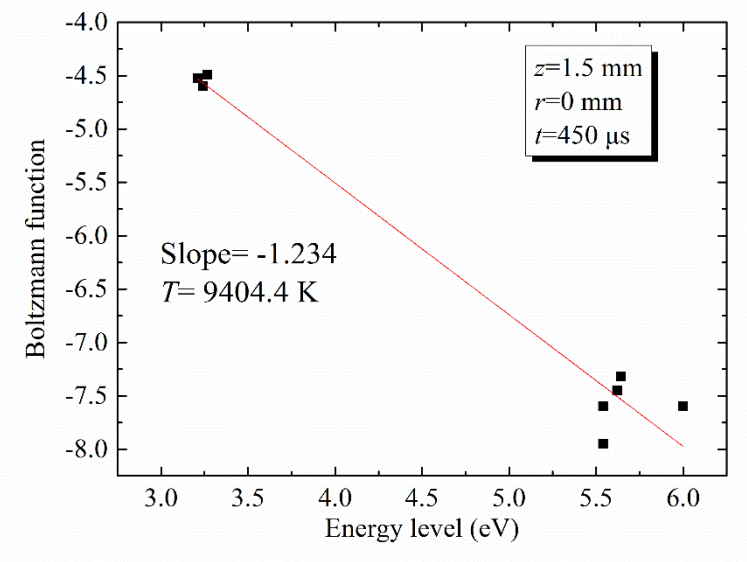

Figure 3.7. Boltzmann plot of the 8 spectral lines (in table 3.1) used to deduce the plasma excitation temperature at the position z=1.5 mm above the workpiece, on the arc axis r=0mm, and at time t=450µs.

3.3 Results and discussion

3.3.1 Plasma temperatures

** Temperature distribution in the pulsed MAG arc:* This section focuses on the temperature distribution in the arc. Figures 3.8 (a)-(c) present the results for the temperature profiles at the layers z=0.5 mm, 1.5 mm and 2.5 mm, respectively. The temperatures are almost identical for the two methods (considering their error bars), except in the fringe of the arc. It indicates that most of the arc is in LTE state and that deviation of LTE can exist in the arc fringes. A more detailed analysis of the LTE assumption is given in section 3.4.2.

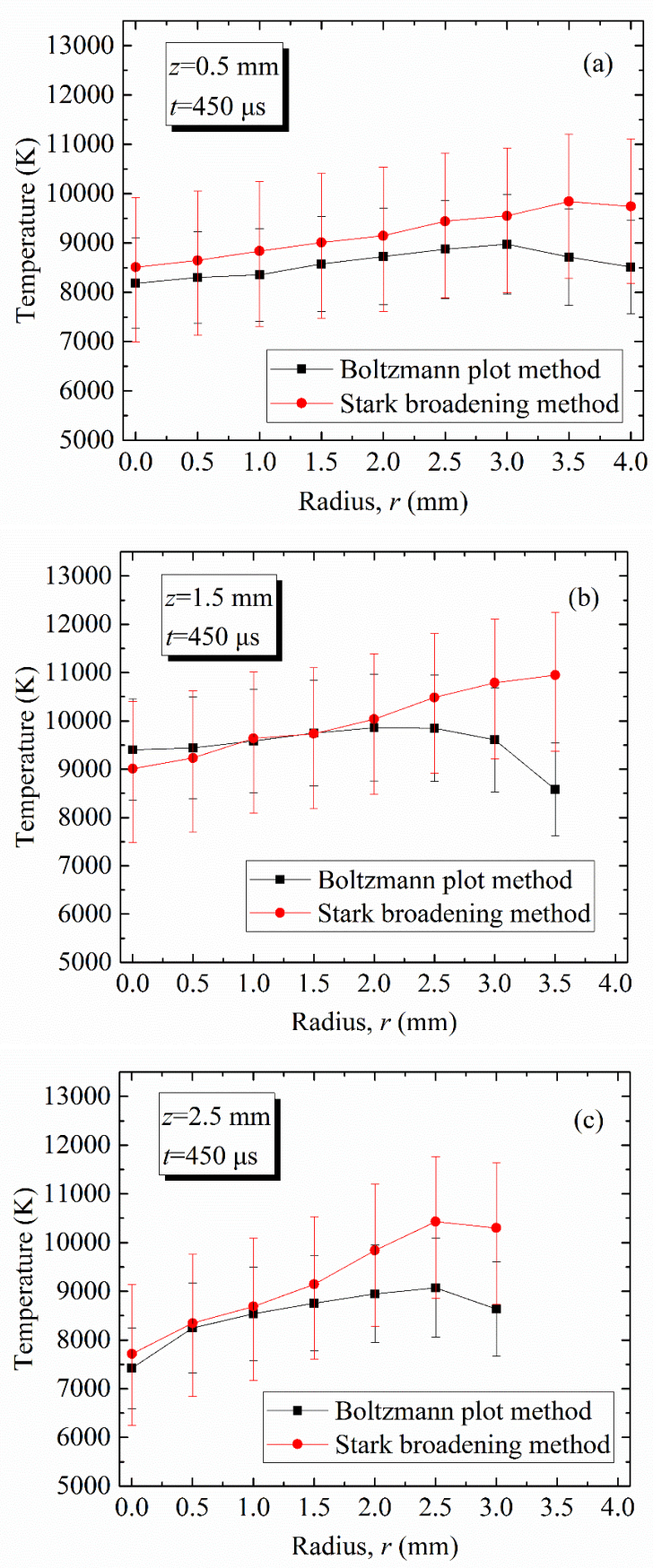

Figure 3.8. Temperature profiles in the layers of the arc (a) *z*=0.5 mm (b) *z*=1.5 mm and (c) *z*=2.5 mm at *t*=450µs.

For the three layers, it can be seen from figure 3.8 that the plasma temperature decreases gradually towards the arc axis, with a temperature drop near the arc axis, especially for the layer below the wire (*z*=2.5 mm). This phenomenon is related to the presence and the effect of metal vapours. Due to the heat effect of the arc, high concentrations of metal vapours would be produced in the molten wire and then enter the arc with the flow of the plasma. The iron vapours have a strong cooling effect on the arc due to increased radiative emission. For example, for a plasma with a radius of 1 mm, the net emission coefficient is 1.11×10^{7} $W.m^{-3}.sr^{-1}$ at 8000 K for an argon plasma, while it reaches 1.13×10^{10} $W.m^{-3}.sr^{-1}$ for an iron plasma [3]. Besides, the metal vapour influx from the wire to the arc could also decrease the arc temperature. This is because that during this process the metal vapours would absorb heat from the arc, with its temperature increasing from the evaporation temperature (about 3000 K) near the wire to the plasma temperature. On the other hand, the presence of the molten metal at the wire electrode and the workpiece, which cannot be hotter than iron boiling temperature, creates a cooling effect. This is the main cause why the plasma temperature is lower at z=0.5 mm and z=2.5 mm than at z=1.5 mm.

** Comparison with a pulsed MIG arc in literature:* The pulsed gas metal arc welding is a widely used technique, either with inert (Metal inert or MIG welding) or active (Metal active or MAG welding) shielding gas. The former uses pure inert gases (e.g. argon) as shielding gas, and the latter uses gas mixtures (e.g. 82%Ar-18%CO_2 mixture in this work). Rouffet *et al* [12] have investigated the plasma temperature in a pulsed argon MIG arc. However, although the same welding mode (ODDP) and similar pulsed current were used, there were great differences in arc shape and temperature between our MAG arc and the MIG arc. Hence, we propose here comparison between them.

Rouffet *et al*[12] performed spectroscopic investigation for the pulsed MIG arc in the shielding gas of pure argon and with a steel wire 1.2 mm in diameter during the high-current phase, based on the LTE assumption. The peak current 430 A and the peak time 1200μs were used to obtain an ODDP mode, with the arc length of 8 mm (figure 3.9). In our work, a higher peak current (500 A) and a shorter peak time (840 μs) was used, and the arc length was 3 mm (figure 3.5).

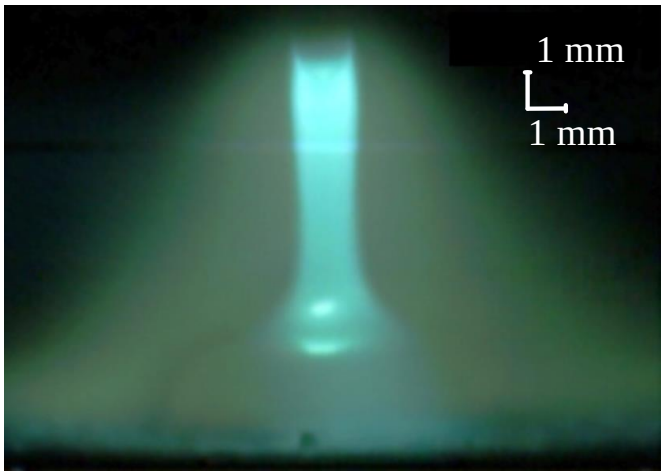

Figure 3.9. Arc image for a pulsed MIG arc at the time of 540 μs during the high-current phase, taken from Rouffet *et al* [12].

Figure 3.10 compares the radial temperature distribution in the pulsed MIG arc studied by Rouffet *et al*[12] and in our pulsed MAG arc. Since only the layer in the middle of the arc (*z*=4 mm) was measured by Rouffet *et al*, a corresponding layer in the middle region of the MAG arc (*z*=1.5 mm) was chosen. The temperature distribution in the MIG arc at 540 μs is presented and compared with those of our MAG arc at t=450μs and deduced by the Boltzman plot. The time difference between them is acceptable, since the temperature change in the MIG arc is small during the pulse[12].

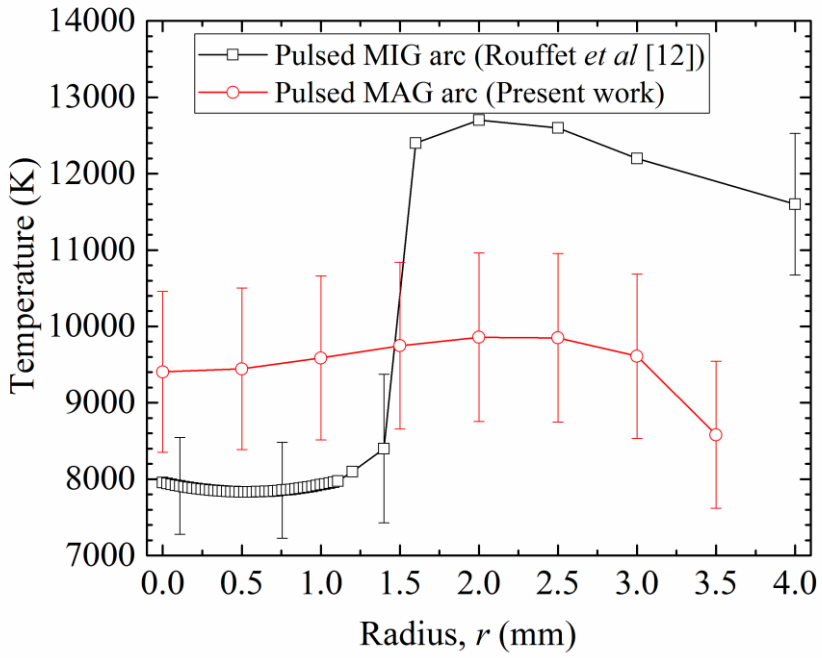

Figure 3.10. Comparison of the radial temperature in a pulsed MIG arc and in a pulsed MAG arc.

It can be seen that the temperature drop near the arc axis is significantly more obvious in the MIG arc than in the MAG arc. For the MIG arc, the temperature is around 8000 K in the inner region, and it increases rapidly to about 13000 K at r=1.5 mm. For the MAG arc, the temperature is 9404.4 K on the axis, and it changes slightly towards the edge of the arc, with a variation of less than 1000 K. The difference between the two arcs may result from the effect of CO_2 in the shielding gas. Valensi *et al* [28] found that the addition of CO_2 in argon gas would form an oxide layer which hinders the arc attachment at the wire tip, thus causing a more diffused iron vapour distribution in the MAG arc. For the MIG arc, since there is no existence of oxide layer, the iron concentration only concentrates in a narrow central region of the arc. As a consequence, the temperature drop caused by the metal vapour exists in a narrow central region of the MIG arc, while it exists in a wider region of the MAG arc.

3.3.2 LTE assumption

Many plasma spectroscopic methods, e.g. the Boltzmann plot method[19], were established assuming the LTE assumption. Some models of GMAW arcs have also been developed under LTE[5-9]. However, there has been no sufficient experimental evidence for the LTE assumption in the case of pulsed MAG arcs.

Theoretically, the LTE assumption can be validated by comparing the excitation temperature from the Boltzmann plot method with the electron temperature from the Stark broadening method. As seen in figure 3.5, the electron temperature is very close to the excitation temperature in most of positions except in the arc fringes, where the difference of these two temperatures can reach 2000 K. It indicates that LTE is questionable in the arc fringes. Therefore, we propose here to verify the LTE assumption from other aspects.

Griem[40] has established a criterion for the existence of LTE in homogenous and isothermal plasmas:

$$n_e \geq 9\times10^{23}\left(\frac{E_{21}}{E_{H^+}}\right)^3\left(\frac{k_B T}{E_{H^+}}\right)\left(m^{-3}\right). \qquad (3.10)$$

where E_{21} is the energy gap between the ground state and the first excited level, E_{H^+} is the ionization energy of hydrogen atom (E_{H^+}=13.58 eV). The right-hand term of the inequation is the electron densities required for LTE (named n_r in the following text).

This criterion shows the sensibility of n_r to E_{21}. For example, if E_{21}(Ar)=11.55 eV and E_{21}(Fe)=0.86 eV, n_r(Fe)/ n_r(Ar)=1/2422.

Figure 3.11 presents the electron density required for LTE in the case of pure argon and pure iron plasmas at temperatures existing in the MAG arc for the three layers z=0.5 mm, 1.5 mm and 2.5 mm. For the electron density required for LTE, n_r(Ar) is far greater than n_r(Fe) for the same position, and the maximums of n_r(Ar) are in the arc fringes, with values from 3.42×10^{22} m^{-3} to 3.82×10^{22} m^{-3}. Since the MAG arc is a mixture of shielding gas and iron vapour, the required electron density for the arc, n_r(Arc), ranges substantially from n_r(Ar) to n_r(Fe), and n_r(Arc) is close to n_r(Fe) in the arc center and close to n_r(Ar) in the arc fringe since the iron vapour concentrates in the arc center.

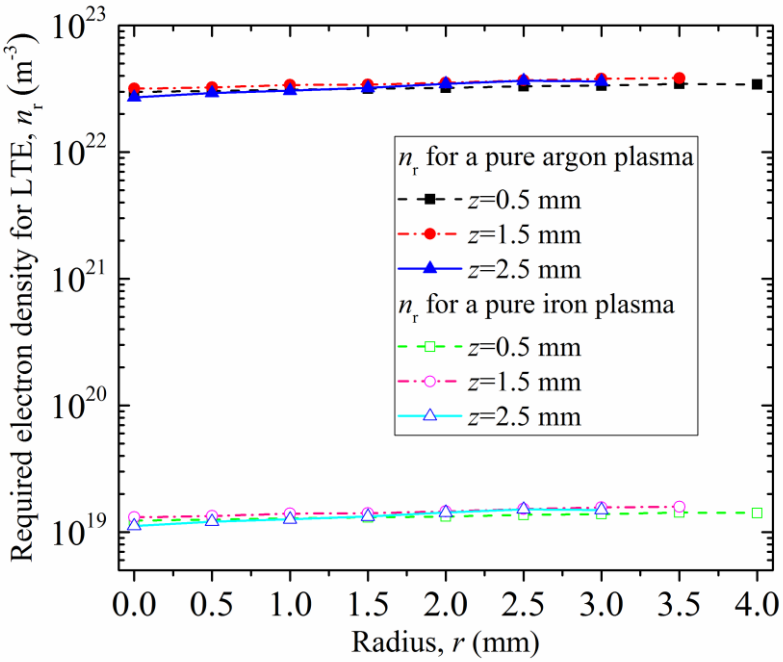

Figure 3.11. Required electron densities n_r for LTE at temperatures measured in the MAG arc for pure argon and pure iron plasmas, based on the criterion proposed by Griem[40].

Figure 3.12 shows the results for the electron density n_e measured by the Stark broadening method and the electron density required for LTE n_r (Ar) in the three layers z=0.5 mm, 1.5 mm and 2.5 mm. It can be seen that n_e reaches a maximum on the arc axis and decreases with radius in each layer, with its minima ranging from 1.90×10^{22} m^{-3} to 3.29×10^{22} m^{-3} in the arc fringes. By comparing n_e and n_r(Ar), we found that n_e are far higher than n_r(Ar) in most of positions except in the arc fringes, where n_e is slightly smaller than n_r(Ar). As a consequence, LTE can be assumed in

most regions of the pulsed MAG arc, and deviation of LTE only exists in the arc fringes. This conclusion is consistent with that drawn by the comparison of the electron temperature and the excitation temperature (see figure 3.8).

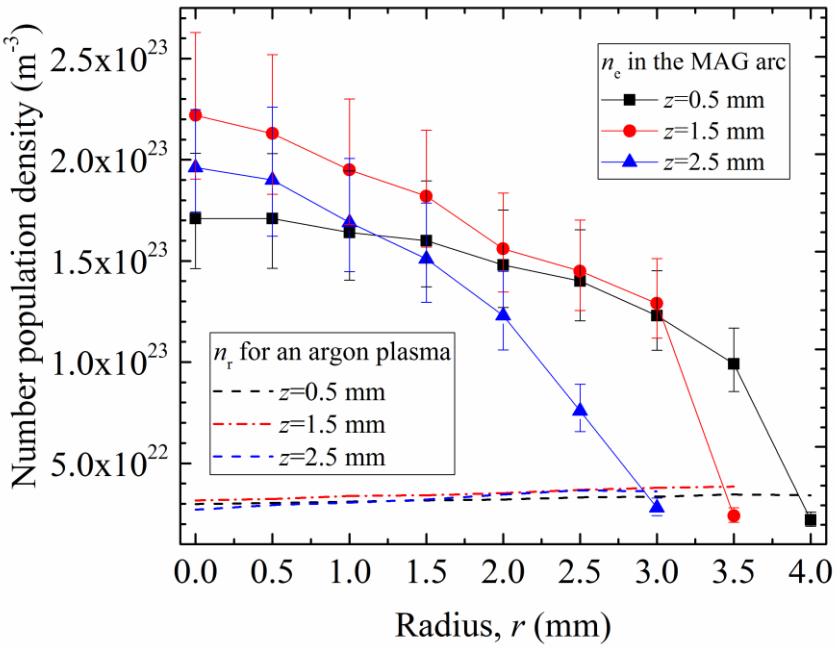

Figure 3.12. Electron density profiles issued from the Stark broadening in the three layers of the MAG arc (z=0.5 mm, 1.5 mm, 2.5 mm), and at time t=450μs.

Figure 3.13 presents the results of iron mole fraction in the three layers of the MAG arc where LTE can be assumed. It can be seen in the figure that high concentrations of iron vapour exist in the arc, especially at the positions near the arc axis and the wire electrode (anode). The iron fraction approaches even 100% at the position z=2.5 mm and r=0 mm. Also, the iron concentration at the arc fringes (z=1.5 mm, r=3.0 mm) is estimated, although the departure of LTE occurs here. The electron density is 2.40×10^{22} m^{-3} at 10949.1 K, which is less than the electron density in LTE (4.60×10^{22} m^{-3}). It indicates that the arc fringe is not contaminated by iron vapour. As a consequence, we conclude that the presence of iron vapour greatly increases the electron density in the core of the plasma up to values compatible with LTE. On the other hand, stronger radiation loss can lead to departure from LTE but our result show that this effect seems not to be dominant.

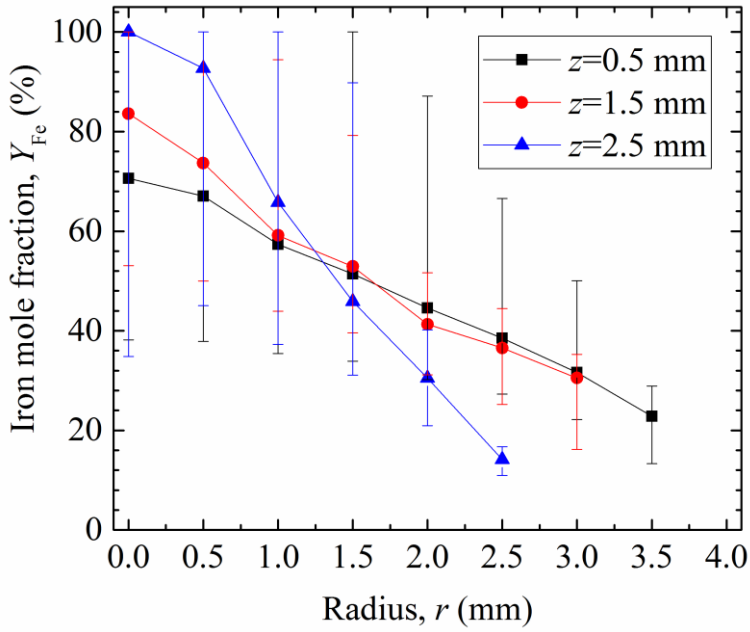

Figure 3.13. Iron mole fraction in the layers of z=0.5 mm, z=1.5 mm and z= 2.5 mm at t=450 μs.

3.4 Conclusion

A spectroscopic study was performed for a pulsed MAG arc in 82%Ar-18%CO_2 mixture and with a steel wire at the middle time of the high-current phase. Since the MAG arc are highly unsteady, the welding current and voltage were synchronously measured to calibrate the time for the spectroscopic study, and arc images were obtained to find proper diagnostic positions. The excitation temperature was measured by the Boltzmann plot analysis of many Fe I lines (based on LTE), and the electron temperature and electron density by the Stark broadening analysis of Fe I 538.3nm and Ar I 696.5 lines (independent of LTE). Our experimental results show that

(1) The electron temperature and the excitation temperature are almost identical in most of the positions in the MAG arc. The plasma temperature decreases towards the arc axis and there is a temperature drop near the arc axis, which would be related to the strong cooling effect of the iron vapour in the arc.

(2) Although the temperature drop near the arc axis has also be found in the pulsed MIG arc in literature [12], it is less steep in the pulsed MAG studied. It

maybe results from that the iron vapour is more diffused in the MAG arc than in the MIG arc.

(3) By the comparison of the electron temperature and excitation temperature and by the verification of the LTE criterion proposed by Griem, it was found that LTE can be assumed in the arc expect in the arc fringe, where the electron temperature is higher than the excitation temperature by about 2000 K.

(4) The existence of LTE in the MAG arc can be associated to the presence of high concentrations of iron vapour (e.g. approaches 100% by mole at the position z=2.5 mm and arc axis), which can strongly increase the electron density.

Besides the first investigation of the temperature and LTE assumption in the pulsed MAG arc, this work should be the basis of future studies, such as the analysis of the arc properties in different droplet modes and the modelling the MAG arc under LTE assumption. Also, extension of this method would allow us to determine the iron vapour distribution in the arc, raising the possibility of the determination of the heat transfer between the arc and the workpiece.

Chapter 4 Use of radiative properties to determine temperature and vapours concentration in MAG arc

This chapter introduces a method allowing a fast determination of space- and time-resolved plasma temperature and iron concentration for a MAG arc during the high-current phase. This method consists in measuring the plasma spectral radiation of a 82% Ar-18% CO_2 plasma with iron vapours using a high-speed CCD camera filtered by narrow band filters in the spectral intervals of 570-590 nm and 606-627 nm respectively; calculating theoretically the dependence of the absolute emissivity $\varepsilon_{570\text{-}590\ nm}$ and relative emissivity $\varepsilon_{570\text{-}590\ nm}/\varepsilon_{607\text{-}627\ nm}$ versus the plasma temperature and the iron concentration, and comparing the two results in order to deduce the plasma temperature (T) and iron concentration (Y_{Fe}) fields of the experimental measurements. The evolution of their profile in time and space are coupled to arc recorded images. This method has also been validated for a layer of plasma at the position of 1.5 mm above the workpiece by using a high-resolution spectrometer and adopting other existing diagnostics such as Stark broadening. The plasma temperature and iron concentration show good agreement throughout the different methods, which demonstrates the effectiveness of this new method.

4.1 Fundamentals of arc diagnostics by use of CCD camera

To inllustrate the diagnostics principle, it is necessary to first introduce the image process of CCD camera. As an example, figure 4.1 shows the image process of a layer of a cylindrically symmetric arc. The arc radiation is filter by a narrow-band filter with a wavelength range of $\Delta\lambda$ and a neutral density filter before entering into the camera. The emission coefficient within the wavelength range $\Delta\lambda$ and at the radial position of the arc r is $\varepsilon(\Delta\lambda, r)$. The integrated radiation across the line AA' is $I(\Delta\lambda, y)$. The radiation density $I(\Delta\lambda, y)$ pass through the filters and enter into the camera, forming a point with a brightness of $Grey(\Delta\lambda, y)$ on the image.

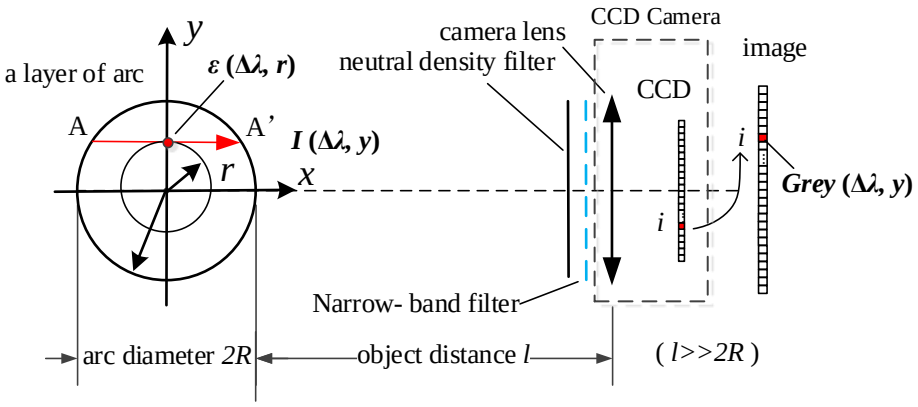

Figure 4.1. Image process from an arc to a picture.

The above image process involves two relations: (1) $\varepsilon(\Delta\lambda, r)$ and $I(\Delta\lambda, y)$; (2) $I(\Delta\lambda, y)$ and $Grey(\Delta\lambda, y)$. Besides, the emission coefficient within the wavelength range $\varepsilon(\Delta\lambda)$ has relations with plasma parameters (such as, temperature T and component Y). These relations will be discussed as follows:

** ε (Δλ, r) and I (Δλ, y):*

The reconstruction of the radial density distribution of a cylindrically symmetric object is a common task in plasma physics. For a cylindrically symmetric and optical thin arc, the emission coefficient $\varepsilon(\Delta\lambda, r)$ and its integrated radiation density $I(\Delta\lambda, y)$ conforms to the relation of Abel transform[133, 134]:

$$I(\Delta\lambda, y)=2\int_0^R \varepsilon(\Delta\lambda, r)\mathrm{d}x \tag{4.1}$$

Assuming $\varepsilon(\Delta\lambda, r)$ drops to zero more quickly than $1/r$, the inverse Abel transform is given by[133, 134]

$$\varepsilon(\Delta\lambda,r)=-\frac{1}{\pi}\cdot\int_r^R \frac{\mathrm{d}I(\Delta\lambda, y)}{\mathrm{d}y}\cdot\frac{\mathrm{d}y}{\sqrt{y^2-r^2}} \tag{4.2}$$

Indeed, the above equation can not be directly solved because it contains differential item dI/dy while the radiation density $I(\Delta\lambda, y)$ measured is discrete. However, many solution methods have been devolped in practive, such as numerical integration method, polynomial method and Nestor-Olsen method. For the Nestor-Olsen method, the arc is considered as consisting of multiple equidistant annuluses. When the number of annuluses is large enough, the calculation is precise. In the present study, the Nestor-Olsen method is used in section 4.3 due to its easy

computation and widespread use[133, 135]. The introduction of the Nestor-Olsen method is given in Appendix III.

For a non-symmetric arc, the radial density distribution $\varepsilon(\Delta\lambda, r)$ can be obtained by the optical tomography method[136]. Nevertheless, many measurements from different angle of views must be performed.

** I(Δλ) and Gray(Δλ):*

The relation of radiation density $I(\Delta\lambda)$ with its brightness $Gray(\Delta\lambda)$ on the image depends on photographic apparatus and conditions. Usually, under the premise of no overexposure, the stronger the $I(\Delta\lambda)$, the larger the $Gray(\Delta\lambda)$. The value of $Gray(\Delta\lambda)$ ranges from 0 to 255. For a given photographic apparatus (high-speed CCD camera) and photographic conditions (object distance, aperture, exposure time, the cut-off wavelength range of the narrow-band filter, and transmittances of the narrow-band and the neutral density filters), the relation between $I(\Delta\lambda)$ and $Gray(\Delta\lambda)$ can be calibrated by a tungsten strip lamp. The CCD camera is exposure by a tungsten strip lamp. The relation of $I(\Delta\lambda)$ and $Gray(\Delta\lambda)$ can be obtained by changing the brightness of the tungsten strip lamp and recording the corresponding values of $I(\Delta\lambda)$ and $Gray(\Delta\lambda)$.

In a conclusion, it is possible to deduce the radial density distribution of emission coefficient $\varepsilon(\Delta\lambda, r)$ from the brightnesses $Gray(\Delta\lambda, y)$ at different pixels on an image. First, transform the values of $Gray(\Delta\lambda, y)$ to the values of $I(\Delta\lambda, y)$, according to the relation between $Gray(\Delta\lambda)$ and $I(\Delta\lambda)$. Next, transform the values of $I(\Delta\lambda, y)$ to the radial density distribution of emission coefficient $\varepsilon(\Delta\lambda, r)$, according to the Abel-inversion algorithm.

** ε(Δλ) and plasma parameters:*

The emission coefficient in an arc is determined by, and therefore an indicator of the parameters (such as, temperature and component) of that plasma. For plasmas with fixed components at LTE state, temperature is the key parameter. But for plasmas with changeable component, temperature and iron concentration are two key parameters.

In fact, if the compoment of an arc is fixed, it is relatively simple to determine the plasma temperature by use of CCD camera. The plasma radiation properties can be calculated by taking the radiation mechanisms into account. The key is that the choice

of an in ideal wavelength range $\Delta\lambda$, within which the emission coefficient $\varepsilon(\Delta\lambda)$ increases with temperature T. When the the emission coefficient is obtained by a CCD camera, the temperature can be deduced based on the relation between $\varepsilon(\Delta\lambda)$ and T. The CCD method has been tested and validated in measuring the temperature for some plasmas with fixed components, e.g. pure Ar[137, 138], Ar-H_2 and Ar-He-H_2[139] in the case of a stabilized torch or Air[140] in steady or unsteady conditions.

However, to our knowledge, there is no report on the determination of both the temperature and the component concentration for plasmas with unfixed component, e.g. MAG arc (the iron concentration in the arc is changeable and unknown). The determation of the two parameters for MAG arc is just the objective of this chapter. Since the CCD method in fact based on the radiation properties of plasmas, the plasma properties are calculated for Ar-CO_2-Fe plasmas in chapter 2. Another key problem of this method is to find two ideal spectral intervals as diagnostic wavelength ranges, which is discussed in section 4.2.

4.2 Choice of spectral intervals

This study proposes to use the radiation of spectral intervals to diagnose plasma temperature T and iron concentration Y_{Fe}. Since there are two parameters unknown, two spectral intervals $\Delta\lambda_1$ and $\Delta\lambda_2$ are used. The parameters are determined based on the absolute and relative emission density: $\varepsilon_{\Delta\lambda 1}$ and $\varepsilon_{\Delta\lambda_1}/\varepsilon_{\Delta\lambda_2}$. Obviously, the key of this method is to find two ideal spectral intervals, or in other words, find two proper functions of $\varepsilon_{\Delta\lambda_1}(T,Y_{Fe})$ and $\varepsilon_{\Delta\lambda_1}(T,Y_{Fe})/\varepsilon_{\Delta\lambda_2}(T,Y_{Fe})$. The spectral intervals should meet two principles: (1) $\varepsilon_{\Delta\lambda_1}(T,Y_{Fe})$ and $\varepsilon_{\Delta\lambda_1}(T,Y_{Fe})/\varepsilon_{\Delta\lambda_2}(T,Y_{Fe})$ are sensitive to T and Y_{Fe}. It means that if the functions are expressed by a contour plot whose x axis and y axis represent T and Y_{Fe} respectively, the plot should be like a 'net' which is interwoven uniformly (see e.g. figure 4.5); (2) the self-absorption effect is weak in the two intervals.

The selection process of the spectral intervals is introduced as follows: (1) primary election of the possible spectral intervals by the analysis of line emission; (2) exclusion of the spectral intervals strongly absorbed; (3) test of $\varepsilon_{\Delta\lambda_1}(T,Y_{Fe})$ and $\varepsilon_{\Delta\lambda_1}(T,Y_{Fe})/\varepsilon_{\Delta\lambda_2}(T,Y_{Fe})$ in a contour plot to examine whether the first principle is met. Because the calculation of the emission density is necessary for the step (2) and (3), a

brief introduction about it is first given. Next the selection process is described in detail.

4.2.1 Calculation of the emission density.

The emission density is represented by the net emission coefficient (NEC) widely used in modelling of welding arcs[141-143] and measurement of arcs properties[32, 139, 140, 144]. The NEC is defined as the difference between the power emitted by an isothermal and spherical volume and the power absorbed by this volume. According to previous studies[92, 117, 145, 146], the absorption effect is mainly achieved within a certain temperature region. As intervals with weak absorption are expected in this study, the NEC is assumed to be enough suitable to represent radiative property. In addition, the NEC is also used in the step (2) mentioned above. The absorption effect of spectral intervals is determined by comparing their NECs at different plasma radii. The NEC is defined by Lowke[147] as

$$\varepsilon_{\mathrm{N}}\left(T,R_{\mathrm{p}}\right)=\int_{\lambda_1}^{\lambda_2}\varepsilon_{\lambda}(T)\cdot\exp\left(-K^{'}(\lambda,T)\cdot R_{\mathrm{p}}\right)\mathrm{d}\lambda \tag{4.3}$$

According to the above equation, the monochromatic emission coefficient ε_{λ} is needed. This work has been already presented in details in the chapter 2. A brief summarize is given here. All of the radiative mechanisms, including atomic lines, atomic continuum, molecular continuum and molecular bands, were considered for the 82%Ar-18 %CO_2 (by mole) plasmas with various iron contents at atmospheric pressure in the temperature range of 5 kK to 20 kK. The iron contents were set to 0%, 1%, 5%, 10%, 20%, 30%… 90%, 100% by mole in this case. The plasma compositions were calculated based on the assumption of local thermodynamic equilibrium (LTE), which has been widely accepted in the study of GMAW arcs both in modelling [141-143, 148] and experiments [149]. 117213 atomic lines and 39 chemical species were taken into account. To obtain a precise spectrum, the “line by line” method was adopted to take into account the line overlapping, and the radiation of the molecular systems of O_2, CO, CO^+, C_2, CO_2 and O_3 was considered. As an example, the spectrum in the wavelength range of 400-1000nm for a 90% [82%Ar-18%CO_2]-10% Fe plasma (by mole) at 10 kK and atmospheric pressure is presented in figure 4.2.

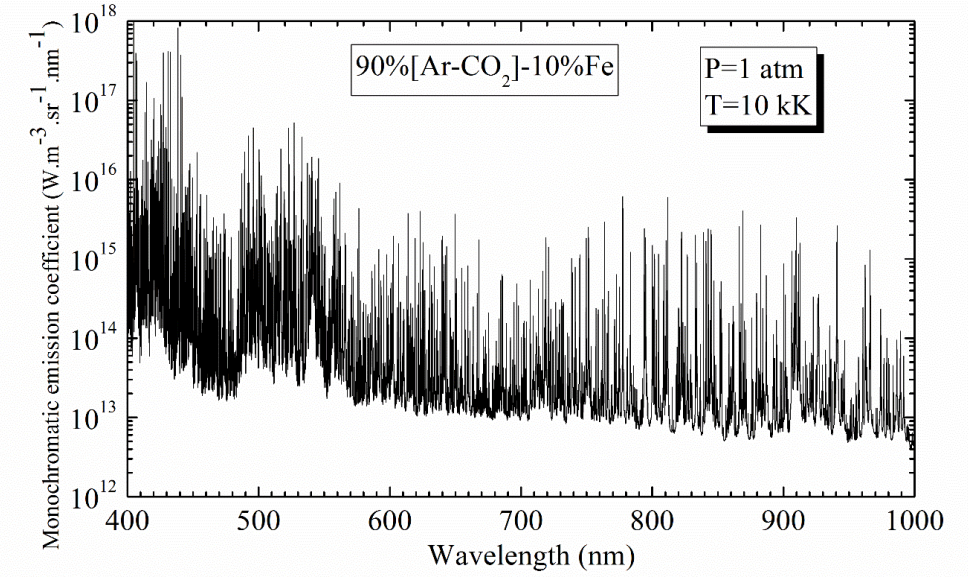

Figure 4.2. Monochromatic emission coefficient ε_λ for the 90% [82%Ar-18%CO_2]-10% Fe mixture at 10 kK and atmospheric pressure.

4.2.2 Primary election of possible spectral intervals

A primary selection is carried out based on line radiation. Compared with the continuum radiation or the molecular radiation, the lines radiation has obvious characteristic and strong emission density which can help us to choose possible spectral intervals primarily. The lines' emission for the wavelength range 400-1000 nm is calculated for a 90% [82%Ar-18CO_2]-10% Fe plasma at 10 kK and atmospheric pressure. This spectral range covers the diagnostic region of common cameras, and 10 kK approaches the temperature measured in previous study of welding arcs containing iron vapours [149].

Figure 4.3(a) shows the results for the 30, 40, 22, 193, and 91 main lines for Ar I, O I, C I, Fe I and Fe II respectively. These lines contribute to 98% of the total line emission of their respective species. The other ionic species, such as Ar II, O II and CII, are not presented due to their weak radiation. It is obvious from the figure 3(a) that Fe I lines dominate the line emission. Due to the strong radiation and large numbers of Fe I lines, the intervals dominated by Fe I lines are preferred. In addition, the expected function $\varepsilon_{\Delta\lambda_1}(T,Y_{\mathrm{Fe}})/\varepsilon_{\Delta\lambda_2}(T,Y_{\mathrm{Fe}})$ has similar type of the two-line method [150], which use two lines with a high gap for the upper level energies E_{u} as diagnostic lines. Therefore, two intervals containing Fe I lines are expected and the E_{u} of Fe I lines in the two intervals should have a wide energy gap.

Figure 4.3(b) shows the upper level energies of Fe I lines coupled to the line emission coefficients. Through a comprehensive comparison, we chose 3 specific intervals with high E_u: 460-480 nm, 530-550 nm, and 570-590 nm, and 4 specific spectral intervals with low E_u: 400-420 nm, 425-445 nm, 607-627 nm and 646-666 nm. These spectral intervals have a wavelength range of 20 nm. The narrow wavelength range ensures the fact that the CCD's sensitivity to light varies a little.

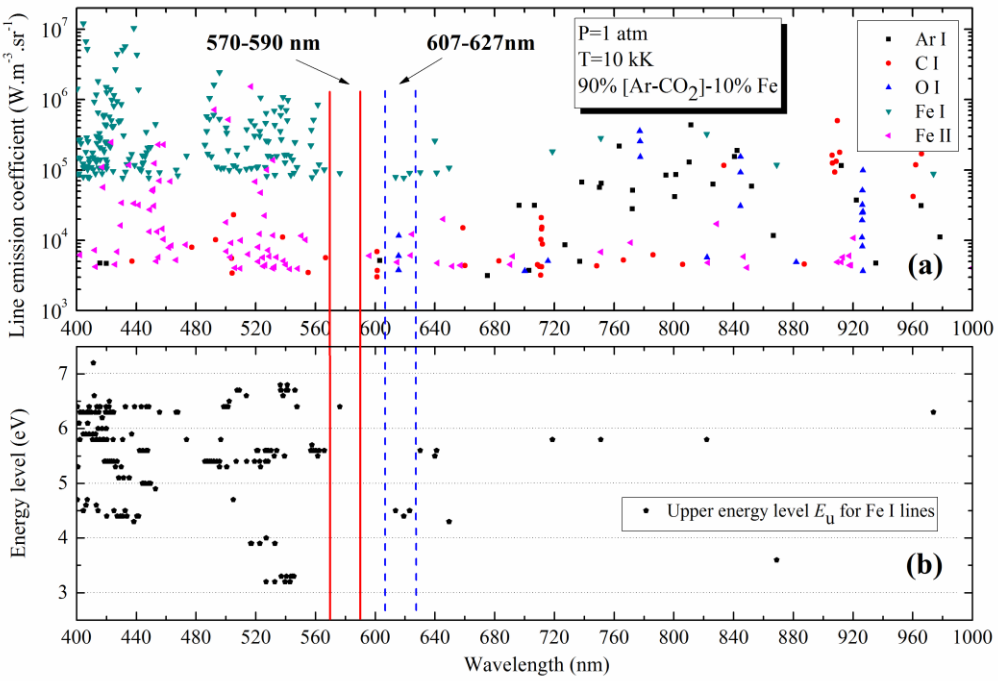

Figure 4.3. (a) Line emission density of the species Ar I, C I, O I, Fe I and Fe II and (b) upper energy levels of Fe I lines for the 90% [Ar-CO_2]-10% Fe mixture at 10 kK and atmospheric pressure.

4.2.3 Exclusion of the spectral intervals strongly absorbed.

The candidate spectral intervals were further refined by comparing their NECs at different plasma sizes. Figure 4.4 shows the relative absorption degrees of each of them for a 90% [82%Ar-18%CO_2]-10% Fe plasma at atmospheric pressure and two plasma's size R_p=0mm and 1mm respectively. The relative absorption degree can be expressed as $\varepsilon_N(\Delta\lambda, R_p\text{=}1\text{ mm})/\varepsilon_N(\Delta\lambda, R_p\text{=}0\text{ mm})$. R_p=0mm corresponds to an optically thin plasma. Figure 4.4 indicates that the absorption effect is obvious in the intervals of 530-550 nm, 400-420 nm and 425-445 nm. It means these spectral intervals are not suitable for the measurement.

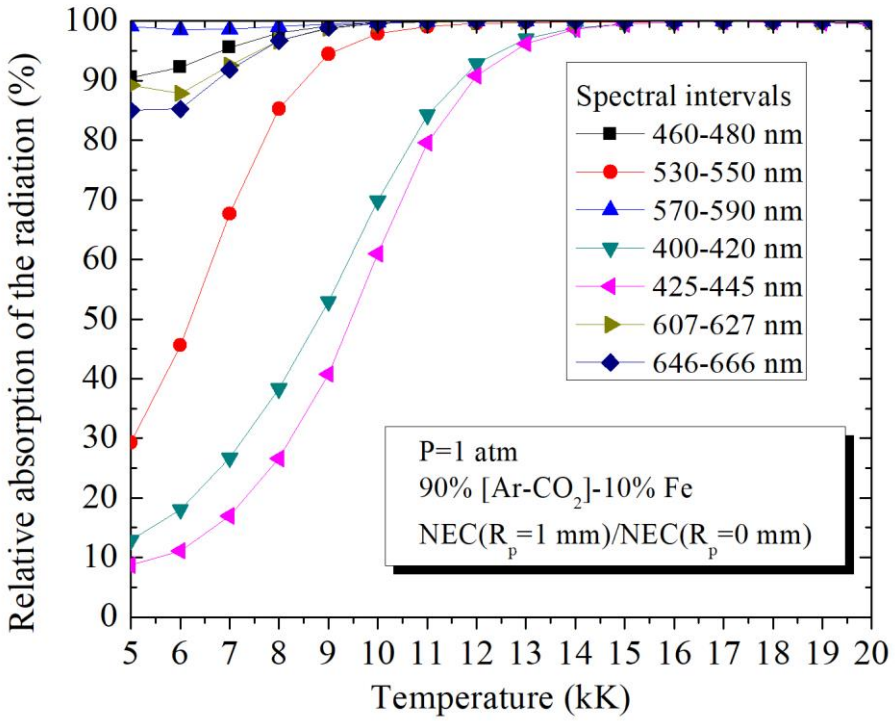

Figure 4.4. Absorption degrees of several spectral intervals for the 90% [Ar-CO_2]-10% Fe mixture at 10 kK and atmospheric pressure.

4.2.4 Test of the $\varepsilon_{\Delta\lambda 1}(T, Y_{Fe})$ and $\varepsilon_{\Delta\lambda 1}(T, Y_{Fe}) / \varepsilon_{\Delta\lambda 2}(T, Y_{Fe})$

The ideal spectral intervals were chosen by testing the $\varepsilon_{\Delta\lambda_1}$and $\varepsilon_{\Delta\lambda_1}/\varepsilon_{\Delta\lambda_2}$in contour plots. After comparison, we chose the spectral intervals of 570-590 nm and 607-627 nm. This selection is justified by plotting the functions of $\varepsilon_{570\text{-}590\ nm}(T,Y_{Fe})$ and $\varepsilon_{570\text{-}590\ nm}(T,Y_{Fe})/\varepsilon_{607\text{-}627\ nm}(T,Y_{Fe})$ as shown in figure 4.5. It can be seen that the two functions meet perfectly the requirements mentioned earlier below 15kK. According to previous study [149], the temperature in GMAW arcs is no more than 15 kK. Therefore, $\varepsilon_{570\text{-}590\ nm}$ and $\varepsilon_{570\text{-}590\ nm}/\varepsilon_{607\text{-}627\ nm}$ are ideal functions for diagnosing MAG arcs. In practice, the measured value of $\varepsilon_{570\text{-}590\ nm}$ and $\varepsilon_{570\text{-}590\ nm}/\varepsilon_{607\text{-}627\ nm}$ can be calibrated in the theoretical plot of figure 4.5, and the intersection is the plasma temperature and iron concentration needed to be determined.

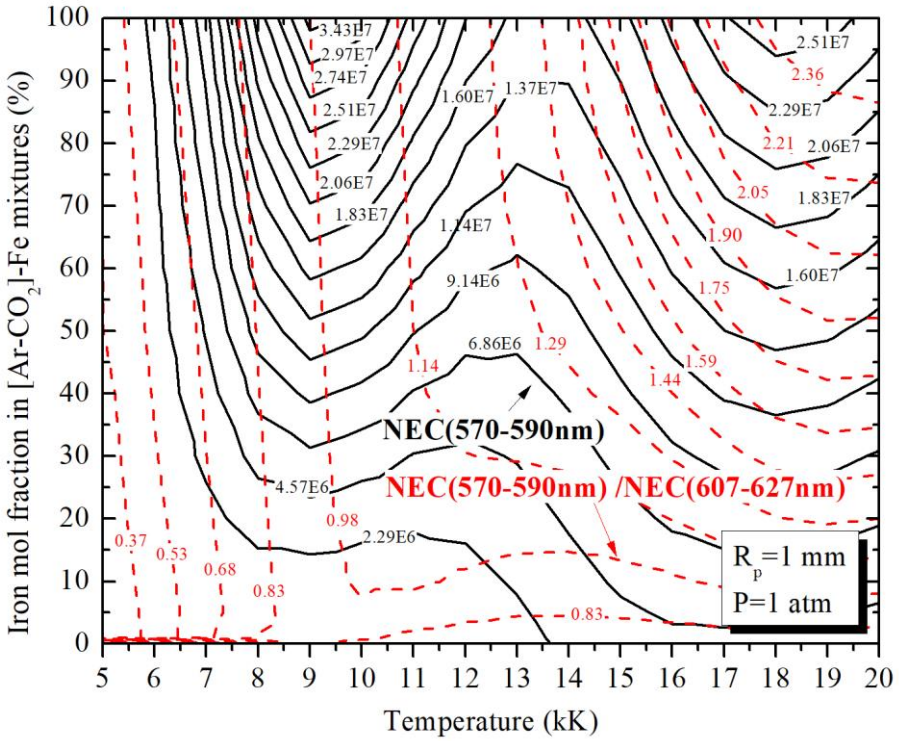

Figure 4.5. The full line is $\varepsilon_{570\text{-}590\ \mathrm{nm}}(T,Y_{\mathrm{Fe}})$; the dashed line is $\varepsilon_{570\text{-}590\ \mathrm{nm}}(T,Y_{\mathrm{Fe}})/\varepsilon_{607\text{-}627\ \mathrm{nm}}(T,Y_{\mathrm{Fe}})$, both at R_{p}=1mm.

4.3 Experimental apparatus and procedure

The functions of $\varepsilon_{570\text{-}590\ \mathrm{nm}}(T,Y_{\mathrm{Fe}})$ and $\varepsilon_{570\text{-}590\ \mathrm{nm}}(T,Y_{\mathrm{Fe}})/\varepsilon_{607\text{-}627\ \mathrm{nm}}(T,Y_{\mathrm{Fe}})$ have been calculated in section 4.2. Based on them, a pulsed MAG arc during the high current period is diagnosed by using a high-speed CCD camera. The diagnostic apparatus and process, and data processing are detailed in this section.

4.3.1 Experimental apparatus and process

The experiment system is shown in figure 4.6. An arc is generated by a welding power (Fronius TPS 4000) in the shielding gas of 82 %Ar-18% CO_2 mixture (by mole). The gas flow is 20 L/min. A Q235A steel workpiece, as the cathode, moves with a mobile platform at a velocity of 0.5 m/min in the direction of the camera look. The anode is an H08Mn2Si wire with a diameter of 1.2mm. The wire is fed through a contact tube at a velocity of 3 m/min. The chemical components of the workpiece and the wire are given in table 4.1, which indicates iron is the main component in both cases. The

contact tube is fixed perpendicular to the workpiece in order to form an axisymmetric arc. The tip of contact tube is located 20 mm above the workpiece and 5 mm within the nozzle.

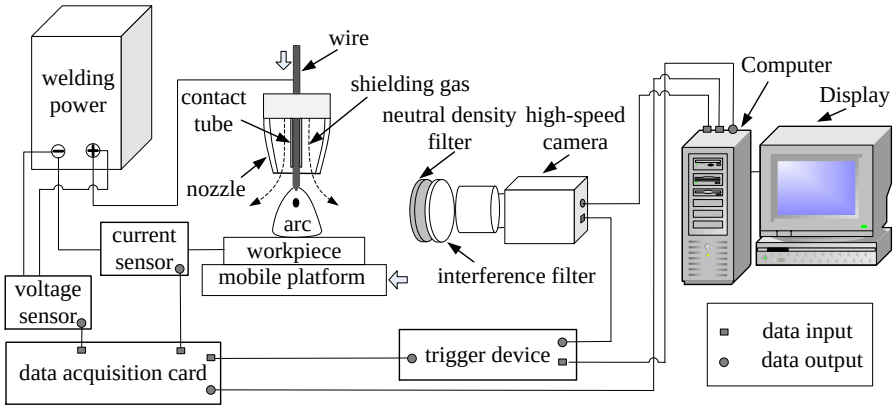

Figure 4.6. Experimental arrangement.

Table 4.1. Chemical compositions (mass %) of the workpiece and the wire.

	Fe	C	Mn	Si	P	S	Cr	Ni	Cu
Q235A	>98.7	0.14-0.22	0.30-0.65	≤0.30	≤0.05	≤0.045			
$H08Mn_2Si$	>95.8	≤0.11	1.8-2.10	0.65-0.95	≤0.025	≤0.015	≤0.20	≤0.30	≤0.50

A black-white high-speed CCD camera (Dalsa, CA-D6-0256W), with an exposure frequency set to 3000 frames/s, is used to diagnose the arc. Two narrow band filters of 570-590 nm and 607-627 nm are placed in front of the camera respectively to filter the radiation from the arc per measurement. The light transmittance of the two narrow band filters is both 70%. To obtain appropriate image brightness, we adjust the exposure time to 30 μs and stacked a neutral density filter with a light transmittance of 1% on the camera. A tungsten ribbon lamp is used to calibrate the lateral spectral radiation intensities for the arc by producing same image brightness with the arc. The local emissivities are then obtained from the lateral radiation intensities by Abel inversion transformation[134]. Here, the Nestor-Olsen Abel-inversion algorithm is chosen due to its easy computation, high precision and widespread use[135, 151, 152].

In the welding process, the synchronous acquisition of electrical signals is obtained to calibrate time for arc images. The welding current is probed with a Hall-effect transducer[153] and the voltage with a differential probe[153]. These signals are collected by a data acquisition card with a time response of 0.8 μs and then

converted to real values by a self-compiling LabVIEW program. We explore the high-current phase of the pulsed MAG welding at t_1=117 μs, t_2=450 μs and t_3=783 μs, which correspond to the beginning, middle and end of the pulse, respectively. The current and voltage curves for each time t_i is shown in Figure 4.7.

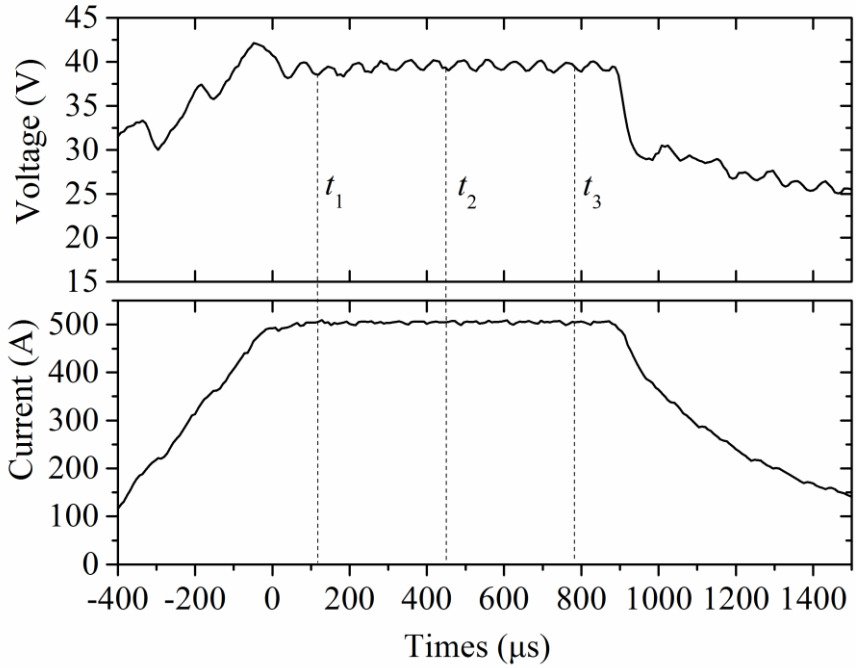

Figure 4.7. Current and voltage measured during the high-current phase of the pulsed MAG welding.

4.3.2 Arc images and data processing

High quality arc images are key to success in plasma diagnostics, since they are primary data source of the determination of plasma temperature and iron concentration. Figure 4.8 shows images of the MAG arc operated in 82%Ar-18%CO_2 mixture (by mole) with a steel wire anode during the high-current (500 A) phase. In the figures, *h* is the distance from the workpiece and *r* is the distance from the arc axis. The images correspond to the times of t_1=117 μs, t_2=450 μs and t_3=783 μs. The optical filters 570-590 nm and 607-627 nm were used respectively to filter the emission from the arc. It is noticed from the figure that the arc images obtained with the two filters has similar shape: a bright central part and a less illustrious outer part. The bright core corresponds to the region where the iron vapour is significant, and the dark part represents the region that contains only shielding gas.

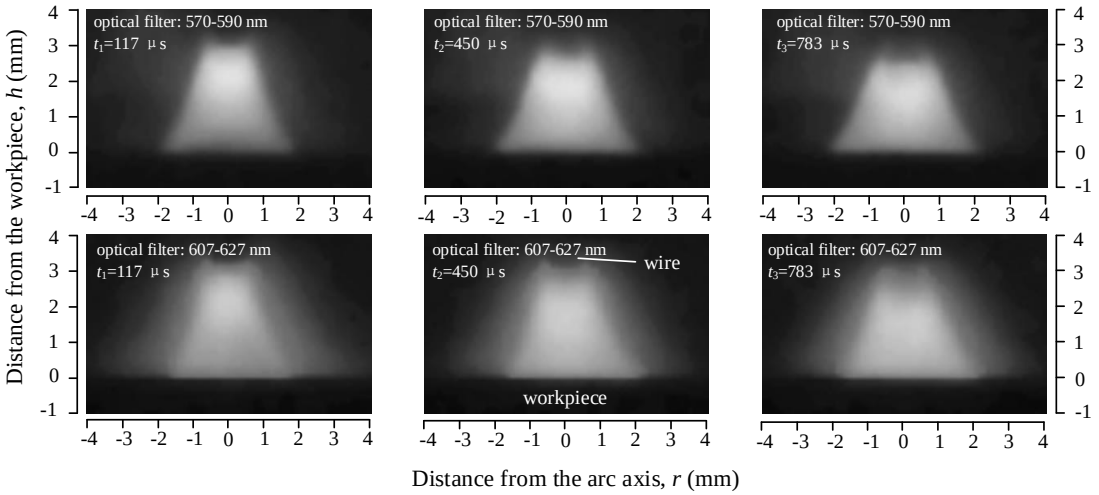

Figure 4.8. Images of MAG arc filtered by narrowband filter 570-590 nm and 607-627 nm at the times of t_1, t_2 and t_3 (3000 frames/s, exposure time: 40 µs; 85×53 pixels; no backlight).

To deduce the plasma temperature and the iron concentration, it is necessary to obtain the absolute and relative emissivities from the arc images. Figure 4.9 shows an example of $\varepsilon_{570\text{-}590\ nm}$ and $\varepsilon_{570\text{-}590nm}$ / $\varepsilon_{607\text{-}627\ nm}$ for a layer of plasma at h=1.5 mm above the workpiece at the time of 450 µs. As example, theses values are 2.61×10^{7} W.m^{-3}.sr^{-1} and 0.995 along the axis (r=0mm). After the acquisition of these values, the plasma temperature and iron vapour concentration are deduced according to the theoretical relations (see figure 4.5). Figure 4.10 presents the the plasma temperature and the iron vapour concentration obtained, with 9225 K and 85.5% along the axis.

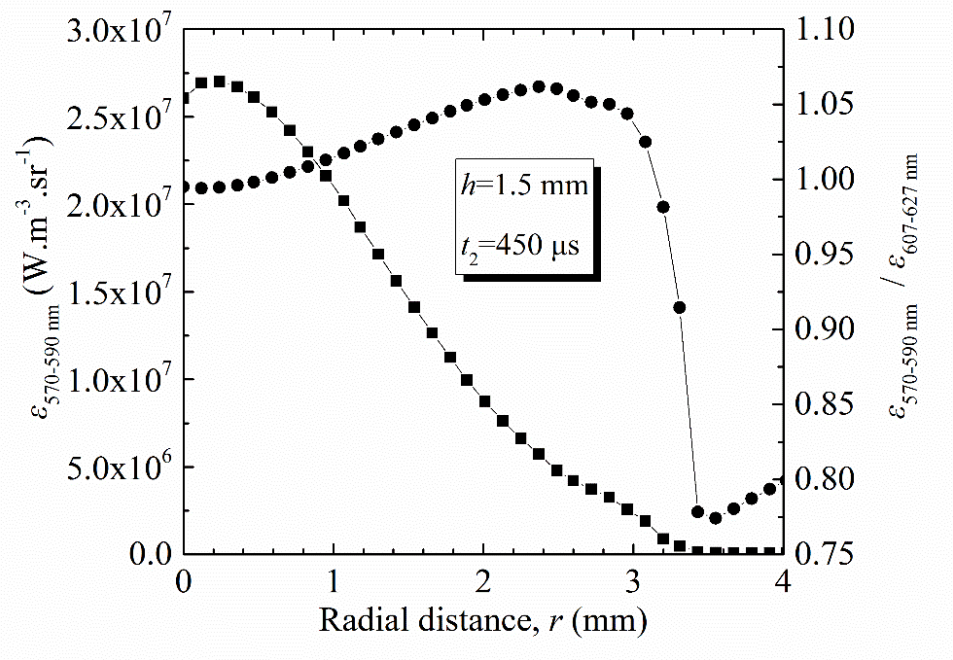

Figure 4.9. Emissivity of the spectral interval 570-590nm (squares) and the relative emissivity of the intervals of 570-590nm and 607-627 nm (circles), as function of the radial position *r*, obtained from the brightness of the image at h=1.5 mm and t_2=450 μs.

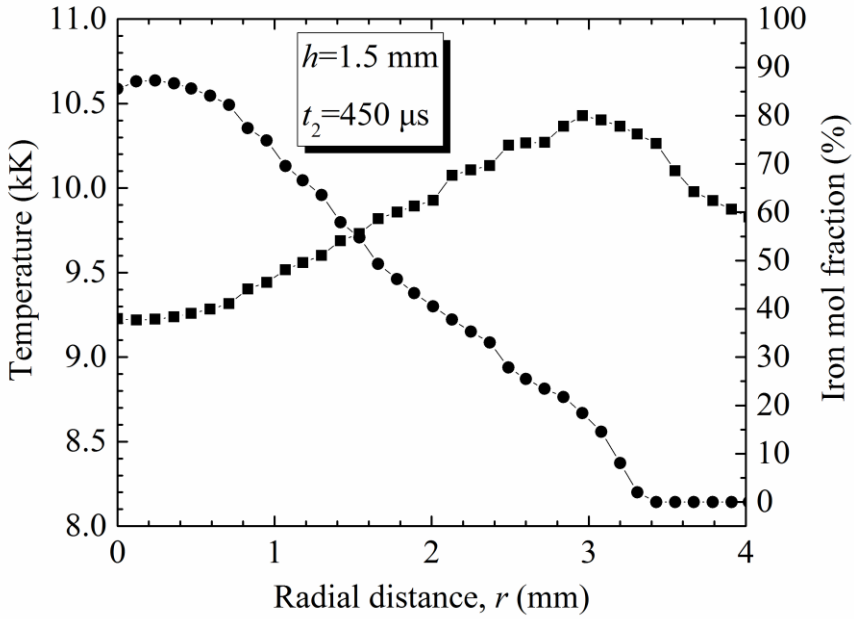

Figure 4.10. Plasma temperature (square) and iron molar fraction (circles) at h=1.5 mm and t_2=450 μs.

4.4 Results and Discussion

Based on the plasma images and the data processing procedure presented in section

4.3, we determined the iron concentration and plasma temperature fields for the pulsed MAG arc at t_1=117 µs, t_2=450 µs and t_3=783 µs (the beginning, middle and end of the pulse), both represented on figure 4.11 on the left, and on the rigth respectively. Since the wire interrupt the line of sight in measurement, the region near the wire was not considered. To better illustrate the results, we discuss the iron concentration and the plasma temperature, respectively, in two separated forthcoming sub-sections.

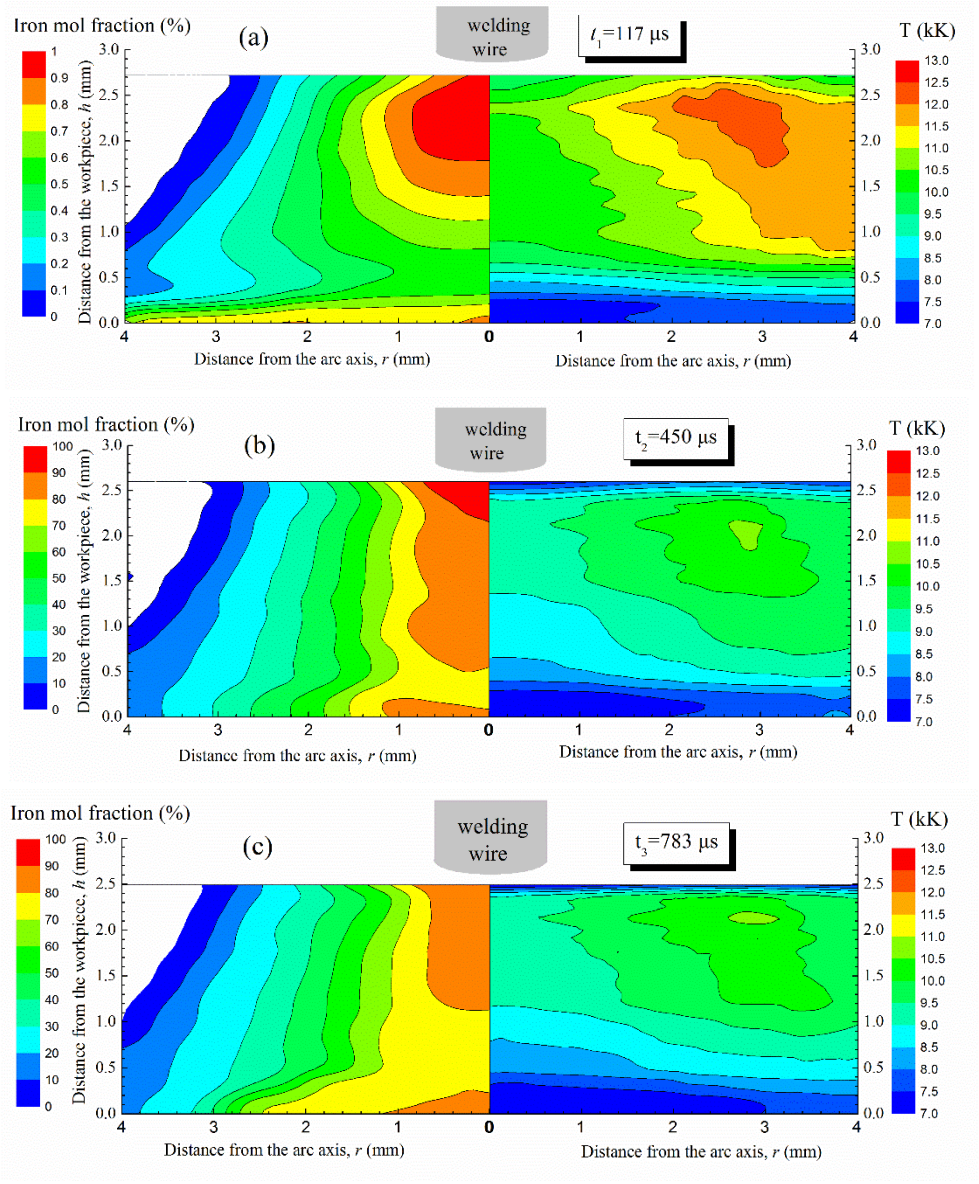

Figure 4.11. Distribution of the arc temperature (right side) and iron mass fraction (left side) at the times of (a) t_1 (b) t_2 and (c) t_3.

4.4.1 Iron concentration field

It can be observed from figure 11 that for the three times examined, high concentrations of iron vapour invariably concentrate below the wire electrode, with mole fraction remaining above 80% on the arc axis within 1 mm of the wire tip. This high iron concentration results from the high pulsed current used (500 A) since the total heat to the wire is basically proportional to the welding current[84, 142]. In addtion, the accumulation of iron vapour near the workpiece is obvious at 450 μs and 783 μs on the figure. This originates in the strong plasma flow away from the electrode towards the workpiece caused by the magnetic pinch effect[1].

Valensi *et al*[24] investigated the properties of a MAG arc in 80%Ar-20%CO_2 mixture, with a steel wire 1.2 mm in diameter and a current of 330A. They measured the mole ratio between the neutral iron and the neutral argon equal to a few tens of per cent below the wire, and they estimated the total iron content to be similar and possibly higher than the argon content. Since we used higher current than Valensi *et al*[24], a higher iron concentration is expected. Hence, present results are in agreement with those obtained by Valensi *et al*[24].

An interesting phenomenon is readable in the iron vapour distribution shown in figure 4.11. The iron concentration decreases with time during the pulse, especially at positions below the welding wire**.** For example, the iron mole fraction at the arc axis and h=2mm reaches 95.7% at t_1= 117 μs, and decreases to 89.2% and 87.6% at t_2=450 μs and t_3=783 μs respectively. Similar phenomenon has also been observed in a pulsed argon MIG arc studied by Rouffet *et al*[154] during the high-current (450 A) phase. They found that the iron mol fraction in the center of the arc was about 60% at the beginning the pulse, and contiously decreased until the end of the pulse.

The above phenomenon is related to the heat production at the wire and the heat transfer in the wire. During the pulse, the arc attachment at the wire tip gradually diffuses with time (see figure 4.8), which results in the decrease of the heat flux at the wire. The extension of the arc attachment has also been observed in the arc images recorded by Rouffet *et al*[154]. Besides, this phenomenon may be linked to the change of heat transfer in the wire. At the beginning of the pulse, a few liquid metal exists in the wire, and the heat transfer in the wire is mainly through conduction. Over the time, more liquid metal is formed and convective heat transfer, which is more effective than heat conduction, starts to work. Under these effects, the iron concentration decreases

during the pulse. Because there is no report on the measurement of thermal process of the wire in GMAW process, a numerical model is needed to explore this question in the future.

4.4.2 Plasma temperature field

On the right part of figure 4.11, the plasma temperature fields are presented. It can be seen that a temperature minimum occurs on the arc axis, associated to high concentrations of iron vapour for the three times. The local temperature minimun is caused by the effect of metal vapour. According to Murhy's review on the effects of metal vapour in arc welding [84], the metal vapour can significantly decreases the arc temperature due to high emission associated to the metal vapours and due to the influence of the metal vapour influx on flow in the arc[155].

Schnick *et al*[156] has proposed a necessary requirement for the local temperature minimum at a given position: the ohmic heat j^2/σ is less than the radiation loss. We illustrated the temperature minimum for a representative position, h=2 mm above the workpiece on axis, at t_1=117 μs as example. At this position, the temperature is 10278 K, with an iron fraction of 95.7%. According to Cressault *et al*[92] the radiation loss ($4\pi\varepsilon_N$) is about 3.37×10^{11} W.m^{-3} W m^{-3} at R_p=1mm. Assuming that the pulsed current (500 A) flows through a region with a radius of 4.0 mm, giving the current density j=9.95×10^6 A m^{-2}. The average electrical conductivity σ is estimated to be about 5.0×10^3 S/m, considering σ=5.8×10^3 S/m at r=0 mm (T=10278 K, Y_{Fe}=0.957) and σ=4.6×10^3 S/m at r=4 mm (T=11604 K, Y_{Fe}=0.0). The ohmic heat j^2/σ calculated is 1.98×10^{10} W m^{-3}, which is less than the radiation loss 3.37×10^{11} W m^{-3}. Therefore, it meet the necessary requirement for the local temperature minimum.

It can be also observed from figure 10 that the arc temperature at the beginning of the pulse is slightly higher than that at the middle and end of the pulse. For example, for the position h=2 mm above the workpiece on axis, the plasma temperature is 10278 K at t_1=117 μs, while 9141 K and 9216K at t_2=450 μs and t_3=783 μs, respectively. At the beginning of the pulse, the radiation loss is larger than the ohmic heat, which should cause a temperature decrease. With the decrease of temperature, the energy balance is established quickly at the middle and end of the pulse, and the temperature remains relatively constant.

4.5 Validation and verification

In order to validate the high-speed camera method, the Stark broadening method was used to deduce the electron temperature from the measured radiation, and the iron content from the electron temperature obtained and the plasma equilibrium composition.

The details have been given in chapter 3. The experimental configuration in chapter 3 is the same as that in this chapter. To simplify this study, we verify only one layer of plasma in the middle region of the arc (h=1.5 mm) at t_2=450 μs.

As has been described in chapter 3, the electron temperature is determined by analyzing the line broadenings of two spectral lines. In this study, the spectral lines of Ar I 696.5 nm and Fe I 538.3 nm were adopted because they are intense enough, strongly broadened, well isolated and have been fully studied. It has been demonstrated that the Stark broadening $\Delta\lambda_S$ (nm) can be expressed as a function of the electron temperature T_e (K) and the electron number density n_e (m^{-3}) for Ar I 696.5 nm [157] and Fe I 538.3 nm[158] with the results:

$$\Delta\lambda_S^{Ar,696.5}=0.0814\frac{n_e}{10^{23}}\left(\frac{T_e}{13000}\right)^{0.3685} \tag{4.4}$$

$$\Delta\lambda_S^{Fe,538.3}=0.2648\frac{n_e}{10^{23}}\left(\frac{T_e}{13000}\right)^{1.670} \tag{4.5}$$

The line broadening is dominated by the Stark Broadening, hence the line broadening measured by the spectrometer was regarded as the Stark broadening in this study, and the electron temperature T_e and the electron density n_e in the arc was obtained by simultaneously solving Eq. (4.4) and (4.5).

Figure 4.12 shows the results for the temperature distribution obtained by the high-speed CCD camera method (figure 4.11) and by the Stark broadening method (figure 3.8). The temperatures are close excepted in the arc fringe (r=3.5 mm) where the temperature obtained by the Stark broadening method is higher than that obtained by the high-speed camera method. This discrepancy may be due to the deviation of LTE in the arc fringe, which has also been found in free-burning arcs at atmospheric pressure[159, 160]. Nevertheless, the difference is only local and insignificant, because the arc fringe has little effect on the heat and current transfer in the arc.

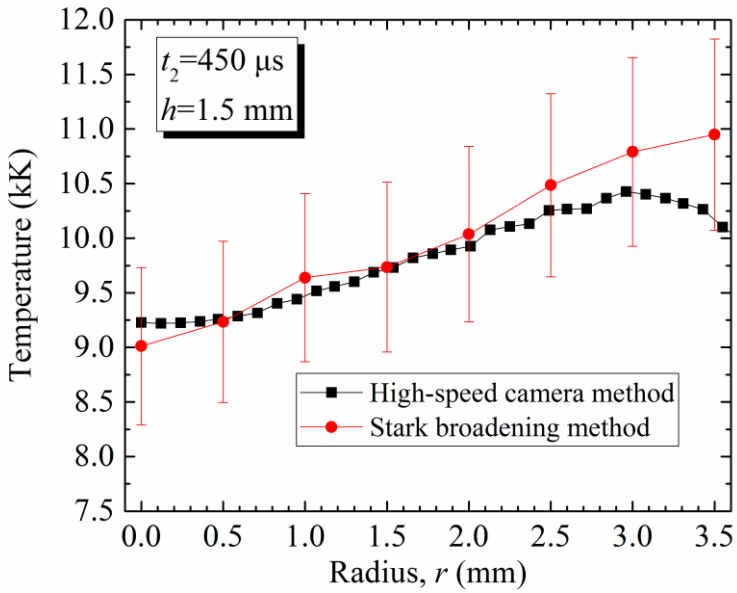

Figure 4.12. Temperature distribution at h=1.5 mm and t_2 =450 µs for the high-speed camera method and the Stark broadening method.

The iron vapour concentration can be estimated from the deduced electron density and the electron temperature based on plasma equilibrium composition (see figure 3.2). Figure 4.13 presents the results for the distribution of iron mole fraction in the arc obtained by the high-speed camera method and by the estimation based on the plasma equilibrium composition. It can be seen that there is a good agreement between the two methods. Therefore, the high-speed camera method is proved to be effective in determining the plasma temperature and iron concentration in the MAG arc.

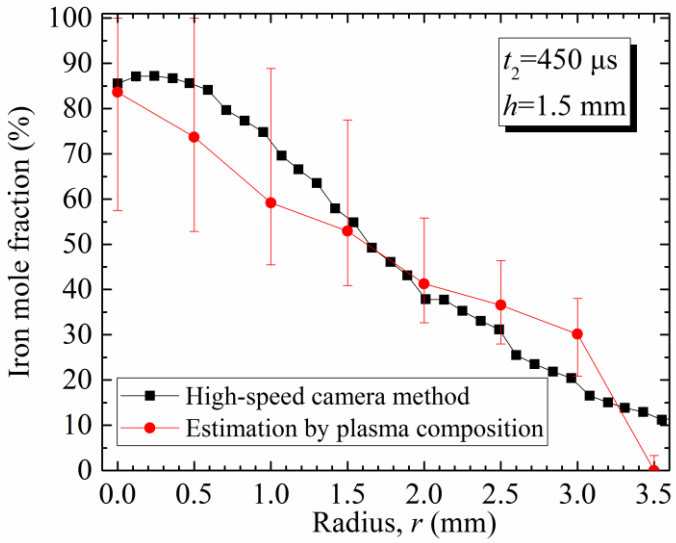

Figure 4.13. Distribution of the iron mole fraction at h=1.5 mm and t_2 =450 µs for the high-speed camera method and the Stark broadening method.

4.6 Conclusion and outlook

This chapter is devoted to introduce a new plasma diagnostic method which allows for fast determination of the time-resolved fields of the temperature and iron vapour concentration in MAG arcs (with [82%Ar-18%CO_2]-Fe plasmas). This method is based on the theoretical relations of $\varepsilon_{570\text{-}590\ \mathrm{nm}}$ and $\varepsilon_{570\text{-}590\ \mathrm{nm}}/\varepsilon_{607\text{-}627\ \mathrm{nm}}$ with T and Y_{Fe} and based on the use of a monochrome high-speed CCD camera. By comparing the values of $\varepsilon_{570\text{-}590\ \mathrm{nm}}$ and $\varepsilon_{570\text{-}590\ \mathrm{nm}}/\varepsilon_{607\text{-}627\ \mathrm{nm}}$ obtained by the arc images with the theoretical relations of $\varepsilon_{570\text{-}590\ \mathrm{nm}}(T,Y_{\mathrm{Fe}})$ and $\varepsilon_{570\text{-}590\ \mathrm{nm}}(T,Y_{\mathrm{Fe}})/\varepsilon_{607\text{-}627\ \mathrm{nm}}(T,Y_{\mathrm{Fe}})$, one can deduce the temperature and iron content in the arc. This method is advantageous due to the fact that it can quickly determine both the temperature and the iron content and can also yield the field distribution for the arc, thus eliminating the diagnostic limit caused by the arc instability and the complex plasma composition.

The method was tested on a pulsed MAG arc during the high-current period. The results show a temperature minimum near the arc axis, accompanied with high concentrations of iron vapour. In addition, the temperature and iron content at the beginning of the pulse are slightly higher than those at the middle and end of the pulse. The high-speed method was aslo validated by the Starking broadening method and the estimattion of iron content, suggesting that the new method can produce satisfactory results.

While this method is used to diagnose an axisymmetric arc, non-axially symmetric arcs could be analyzed by detecting the emission from different directions based on the tomographic reconstruction technique[140]. This method can also be applied to determine the arc properties in different welding modes. Moreover, the results obtained with the new method establish a basis for further work, e.g. the further analysis of current and energy transfer in the arc, and the comparison with numerical simulation.

Chapter 5 Optical radiation associated with photobiological hazards posed by argon GTAW arc

Optical radiation is a by-product of the arc welding process and is emitted simultaneously by the welding arc. The radiative spectra of welding arcs are extremely widened but the radiation energy is essentially transported in ultraviolet (UV), visible, and near infrared ranges. The welding radiation has received much attention in occupation health and safety[43, 46, 161] due to its adverse photobiological effects on skin and eyes. The exposure to excessive welding UV radiation can cause acute health effects: erythema (skin reddening) and photokeratitis (arc eye)[43, 44]. Chronic welding UV exposure may increase the risk of skin aging and skin cancer[43, 45]. Also, the blue light radiation is an important factor for the development of ocular diseases (e.g. retinal/corneal burn).

This chapter presents a theoretical investigation of the UV (180-400 nm), UVA (315-400 nm) and blue light (300-700 nm) radiation associated with the photobiological hazards to workers for argon GTAW arcs. Here, the radiation within 300-700 nm is known as blue light radiation, since the associated hazard is usually referred to as 'blue light' hazard [162]; the spectral interval of 300-700 nm actually covers parts of UVB, all UVA and most of visible radiation, and blue light strictly speaking covers only the wavelength range of 400 to 490 nm.

In this chapter, the radiative properties of argon plasma are calculated for the three spectral regions of interest at temperatures from 5000 K to 25000 K and atmospheric pressure. A two-dimensional model of a GTAW arc is then developed to determine the local emissions in the arc, the total radiation escaping from the arc and corresponding effective irradiances. This model is also used to study the influence of the welding parameters (current intensity and arc length) on the radiative properties and the effective irradiances. The permissible exposure durations are further evaluated according to the radiation exposure standard of the Directive 2006/25/EC for the three spectral intervals.

5.1 Radiative transfer process

The radiation transfer process from a GTAW arc to a surface that corresponds to a welder's skin or eyes is shown schematically in figure 5.1. The analysis was based upon the following assumptions: (i) the radiation transfers in a non-scattering medium (ii) the tungsten cathode is perpendicular to the anode (iii) the anode is restricted to be a water-cooled copper, and thus the metal vapour evaporated from the anode is neglected (iv) during the radiative transfer process, the absorption of the emission in the UV, UVA and blue light regions is negligible, which will be confirmed in the next subsection.

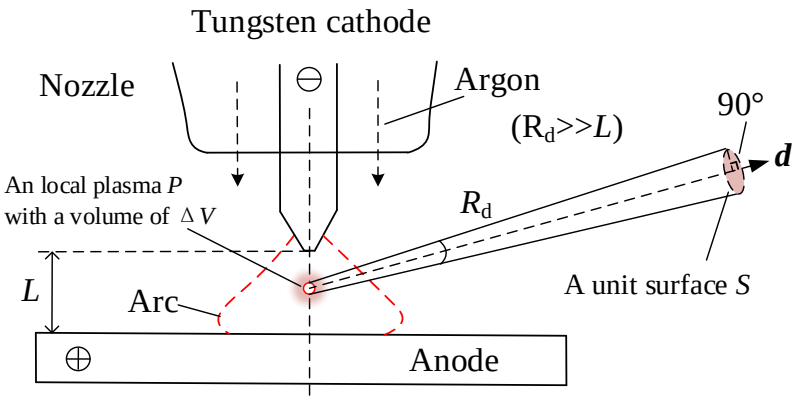

Figure 5.1. Sketch of radiative transfer from a TIG arc to a small surface.

For a local plasma P in a GTAW arc (figure 1), its temperature can be regarded as isothermal. The spectral radiant power of this plasma $\Phi_{\lambda,\Delta V}$ (W.sr^{-1}. nm^{-1}) is given by

$$\Phi_{\lambda,\Delta V}=\varepsilon_\lambda(T)\cdot\Delta V \tag{5.1}$$

Where $\varepsilon_\lambda(T)$ is the spectral emission coefficient (W. m^{-3}.sr^{-1}. nm^{-1}) and ΔV is the volume of the plasma (m^3).

The spectral irradiance (W. m^{-2}. nm^{-1}) on the unit surface S that is perpendicular to the radiation direction due to the local plasma is given by[163]

$$E_{\lambda,\Delta V}=4\pi\cdot\Phi_{\lambda,\Delta V}\cdot\frac{1}{4\pi R_d^2}$$

$$=\frac{1}{4\pi R_d^2}[4\pi\cdot\varepsilon_\lambda(T)]\cdot\Delta V \tag{5.2}$$

Where R_d is the distance from the plasma to the surface S. In the welding environment,

R_d is much larger than the size of the arc (e.g. the arc length L).

The spectral irradiance (W. m^{-2}. nm^{-1}) on the surface caused by the entire arc can be written as

$$E_\lambda = \frac{1}{4\pi R_d^2} \int_V [4\pi \cdot \varepsilon_\lambda(T)] \cdot dV \tag{5.3}$$

According to the exposure standard of the Directive 2006/25/EC (termed the "Directive"), the effective irradiance E_{eff} (W. m^{-2}) within a spectral interval can be given by[162]

$$E_{eff} = \int_{\lambda_1}^{\lambda_2} E_\lambda \cdot X(\lambda) \cdot d\lambda \tag{5.4}$$

Where $X(\lambda)$ is the relative spectral effectiveness (unitless). The $X(\lambda)$ is a biological weighting function and it varies with wavelength. According to the "Directive" [162], the curves of the three spectral intervals are given in figure 5.2. The "Directive", released in 2006, is a European Union directive on the health and safety requirements concerning the exposure of workers to risks arising from artificial optical radiation, and it has been a legislation of all European union countries since 2010.

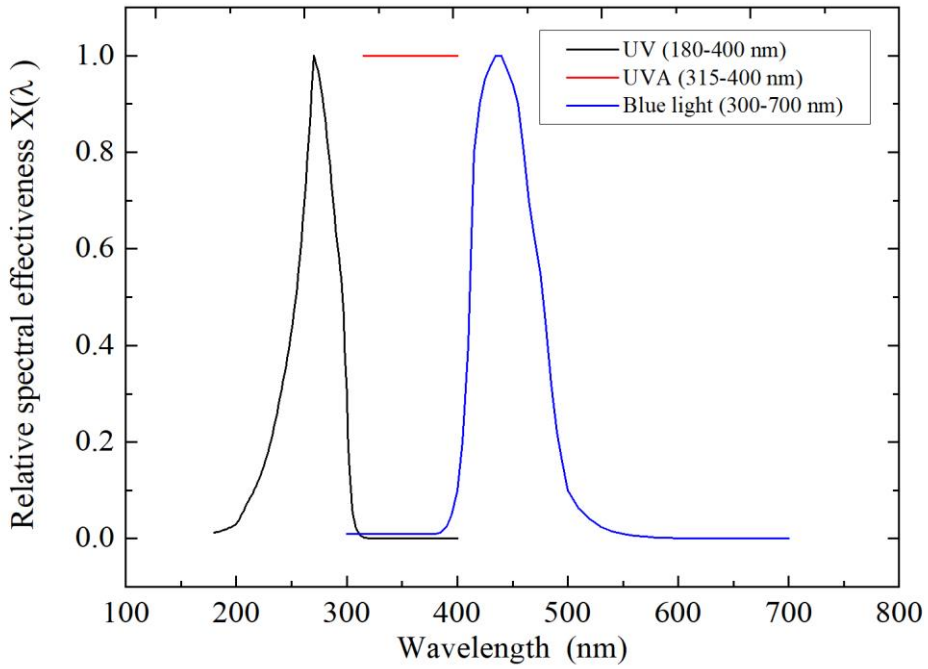

Figure 5.2. Spectral weighting taking into account the wavelength dependence of photobiological effects.

By applying Eq. (5.3) to Eq. (5.4), one finds that the effective irradiance E_{eff} is

$$E_{eff}=\frac{1}{4\pi R_d^2}\int_V \int_{\lambda_1}^{\lambda_2}[4\pi\cdot\varepsilon_\lambda(T)\cdot X(\lambda)]\cdot d\lambda\cdot dV \quad (5.5)$$

To facilitate the analysis, we define an effective emission coefficient (EEC) ε_{eff}, which represents the account of the optical emission per unit volume per unit solid angle that can cause photobiological hazards. The EEC is expressed as

$$\varepsilon_{eff}(T,\Delta\lambda)=\int_{\lambda_1}^{\lambda_2}\varepsilon_\lambda(T)\cdot X(\lambda)\cdot d\lambda \quad (5.6)$$

With the EEC, Eq. (5) reduces to

$$E_{eff}=\frac{1}{4\pi\cdot R_d^2}\int_V 4\pi\cdot\varepsilon_{eff}(T,\Delta\lambda)\cdot dV \quad (5.7)$$

Eq. (7) indicates that the effective irradiance E_{eff} follows an inverse square law on R_d, and the E_{eff} also depends on the EEC (ε_{eff}) and its distribution in the arc.

According to the "Directive", the permissible duration t_{max} (in seconds) can be further determined by[162]:

$$t_{max}=\frac{H_{limit}}{E_{eff}} \quad (5.8)$$

Where H_{limt} is the effective radiant exposure limit (J. m^{-2}). The H_{limt} values and the radiation hazards related to the UV, UVA and blue light radiation are given in table 5.1.

Table 5.1 Exposure limit values for non-coherent optical radiation[162]

Wavelength range(nm)	X(λ)	H_{limit} ($J.m^{-2}$)	Part of the body	Hazard
180-400	S(λ)	H_{eff}=30	eye cornea	photokeratitis
(UVA, UAB and UVC)		daily value 8 hour	conjunctiva	conjunctivitis
			lens	cataractogenesis
			skin	erythema
				elastosis
				skin cancer
315-400	1	$H_{eff}=10^4$	eye lens	cataractogenesis
(UVA)		daily value 8 hour		
300-700	B(λ)	H_{eff}=100	eye retina	photokeratitis
(Blue light)		for t≤10 000 s		

5.2 Radiative properties for argon plasma

In this subsection, the UV, UVA and blue light EECs are calculated for argon plasma in the temperature range of 5000-25000 K at atmospheric pressure. Also, the self-absorption of the UV, UVA and blue light emission are discussed in order to conclude that absorption can be neglected.

In order to calculate the EEC from Eq. (5.6), the spectral emission coefficient ε_λ was determined under the assumption of local thermodynamic equilibrium (LTE). Various contributions to the emission were taken into account: atomic continuum (recombination and bremsstrahlung) and lines.

** Emission of recombination:* the radiative recombination occurs when an atomic ion A^{z+} (with a charge *Ze*) recombines with an electron. Its spectral emission coefficient is given by[92]

$$\varepsilon_\lambda^{\mathrm{rec}}(T)=C_1\cdot\left(\frac{c}{\lambda^2}\right)\cdot\frac{n_{\mathrm{e}}(\mathrm{T})\cdot n_{z^+}(\mathrm{T})}{Q_{z^+}^{\mathrm{int}}(T)}\cdot\frac{Z_{z^+}^2}{\sqrt{T}}\cdot\left[1-\exp\left(-\frac{hc}{\lambda k_{\mathrm{B}}T}\right)\right]\cdot g_1^{z^+}\cdot\xi_\lambda^{(z-1)}(T) \tag{5.9}$$

$$\text{With}\quad C_1=\frac{16\pi\left(e^2/4\pi\varepsilon_0\right)^3}{3c^3\sqrt{6k_{\mathrm{B}}\pi m_e^3}}=5.44436\times10^{-52}\,\mathrm{J.m^3.K^{1/2}.sr^{-1}}$$

Where c is the light speed, e is the electron charge, n_{e} is the electron density, n_{z+} is the number density of the A^{z+} ion, Z_{z+} is the charge of the A^{z+} ion, $Q_{z^+}^{\mathrm{int}}$ and $g_1^{z^+}$ are the A^{z+} internal partition function and the A^{z+} ground state statistical weight respectively, h is the Planck constant, k_{B} is the Boltzmann constant, m_{e} is the electron mass, and ε_0 is the permittivity of free space.

** Emission of Bremsstrahlung:* the radiation is produced by the deceleration of an electron under the influence of an ion or an atom. The spectral emission coefficients for ion-electron and atom-electron interactions are, respectively, given by[92]

$$\varepsilon_\lambda^{\mathrm{ei},z^+}(T)=C_1\cdot\left(\frac{c}{\lambda^2}\right)\cdot Z_{z^+}^2\frac{n_{\mathrm{e}}(T)\cdot n_{z^+}(T)}{\sqrt{T}}\cdot\exp\left(-\frac{hc}{\lambda k_{\mathrm{B}}T}\right)\cdot G_{\mathrm{ei},\lambda}^{z^+}(T) \tag{5.10}$$

$$\varepsilon_\lambda^{\mathrm{ea}}(T)=C_2\cdot\left(\frac{c}{\lambda^2}\right)\cdot n_{\mathrm{a}}(T)\cdot n_{\mathrm{e}}(T)\cdot T^{3/2}\cdot\exp\left(-\frac{hc}{\lambda k_{\mathrm{B}}T}\right)\cdot G_{\mathrm{ea},\lambda}(T) \tag{5.11}$$

with $C_2=\frac{32}{3c^3}\cdot\left(\frac{e^2}{4\pi\varepsilon_0}\right)\cdot\left(\frac{k_{\mathrm{B}}}{2\pi m_{\mathrm{e}}}\right)^{3/2}=3.4218\times10^{-43}\,\mathrm{J\ m\ K^{-3/2}sr^{-1}}$

where n_a is the number density of neutral atoms, $G^{z^+}_{ei,\lambda}(T)$ is the Gaunt factor, and $G_{ea,\lambda}(T)$ is a factor which depends on the electron-neutral collision cross section.

** Emission of atomic lines:* the line emission results from the spontaneous transition of an excited electron from a high energy level E_i to a lower energy E_j. Its spectral emission coefficient is given by[37]

$$\varepsilon_\lambda^{line}(T)=\frac{hc}{4\pi\lambda_{ij}}\cdot A_{ij}\cdot n_i(T)\cdot P_{ij}^{Voigt}(\lambda) \tag{5.12}$$

where λ_{ij} and A_{ij} are the wavelength and the probability of the line emission, n_i is the number density of the emitting atom or ion, and $P_{ij}^{Voigt}(\lambda)$ is the normalized profile of the line. Because the line overlapping may occurs at some adjacent lines, a "line by line" method[37] is used to get rid of the overlapping spectrum.

According to the above formulae, a huge database of the spectral emission coefficient $\varepsilon_\lambda(T)$ with wavelengths from 35 nm to 4500 nm was developed in the temperature range of 5000-25000 K, as shown in figure 5.3. By intergrading the product of the $\varepsilon_\lambda(T)$ and the X (λ) in different spectral interval, one can obtain the UV, UVA and blue light EECs, as shown in figure 5.4.

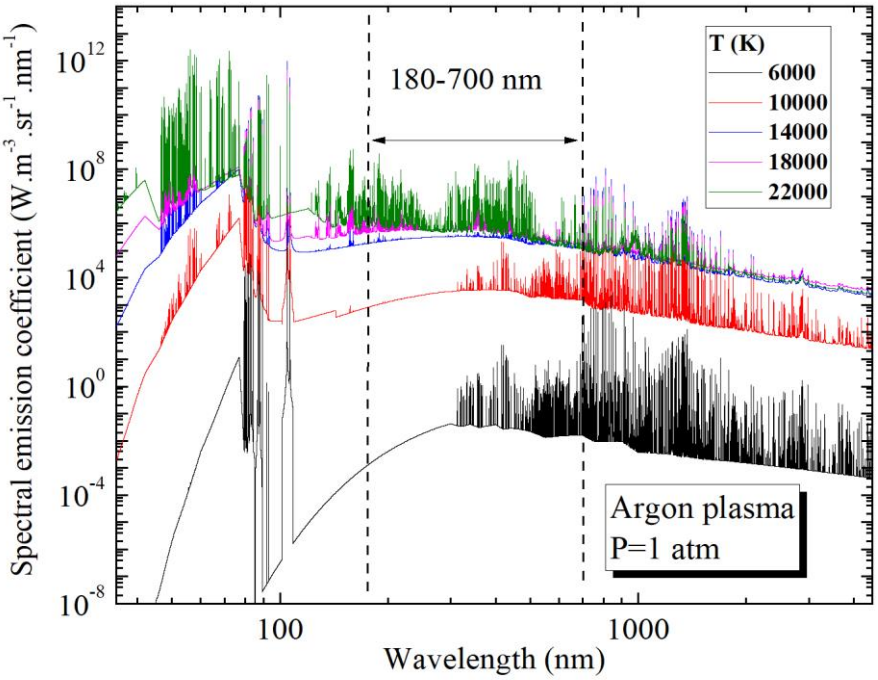

Figure 5.3. Spectral emission coefficient of argon plasma at 1 atm.

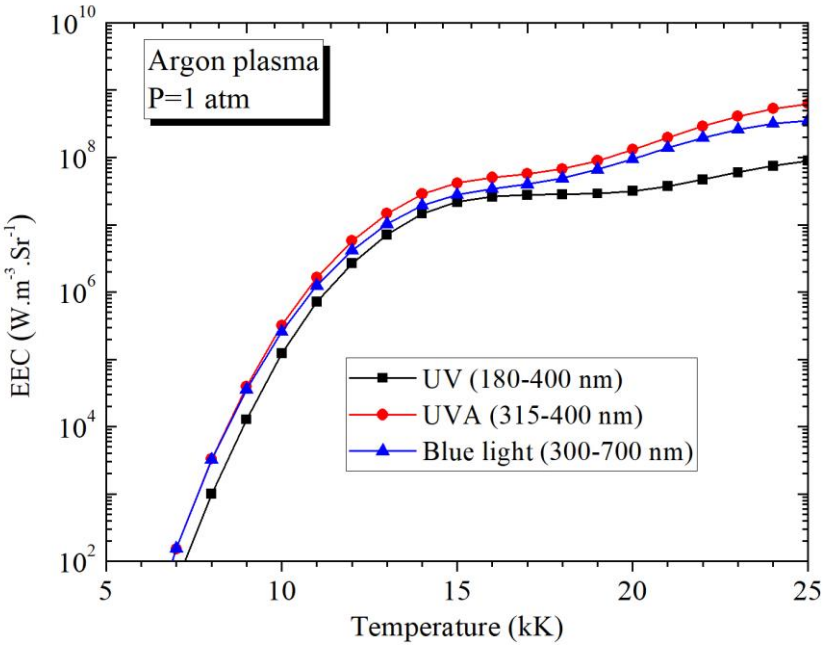

Figure 5.4. Effective emission coefficients versus temperature for the UV, UVA and blue light spectral intervals.

From the local effective coefficient ε_{eff} to the effective irradiance E_{eff}, we assumed that the emissions in the UV, UVA and blue light regions are weakly absorbed. Next, the self-absorption of the emission in the arc plasma will be evaluated with net emission coefficient (NEC) for the three spectral intervals. However, the absorption by the outer air is neglected due to the fact that the absorption of emission in air mainly concentrates in the vacuum UV spectrum (<180 nm)[164].

The NEC, firstly proposed by Lowke[147], is defined as the difference between the power locally emitted by an isothermal control volume and that which is absorbed by this volume. For a spherical geometry, the NEC ε_N is given by[147]

$$\varepsilon_N(T,R_p)=\int_{\lambda_1}^{\lambda_2}\varepsilon_\lambda(T)\cdot\exp\left(-K'_\lambda(T)\cdot R_p\right)\cdot d\lambda \qquad (5.13)$$

Where K'_λ is the spectral absorption coefficient correlated with the spectral emission coefficient ε_λ by Kirchhoff's law, and R_p is the radius of the isothermal and spherical plasma. For R_p =0 mm, this coefficient corresponds to the fictitious case of zero absorption.

According to Eq. (5.13), the NEC decreases with the plasma radius R_p, and thus the absorption of the emission can be evaluated by examining the value of ε_N with R_p. Figure 5.5 presents the results for the NECs and the absorption phenomena in the UV, UVA and blue light regions. It can be seen that the NECs increase with temperature

below 25000 K for the three spectral intervals. Besides, the emissions from an isothermal sphere with a radius of 5 mm are barely absorbed (less than 10%) for the three regions, which indicates that the weak-absorption assumption is correct.

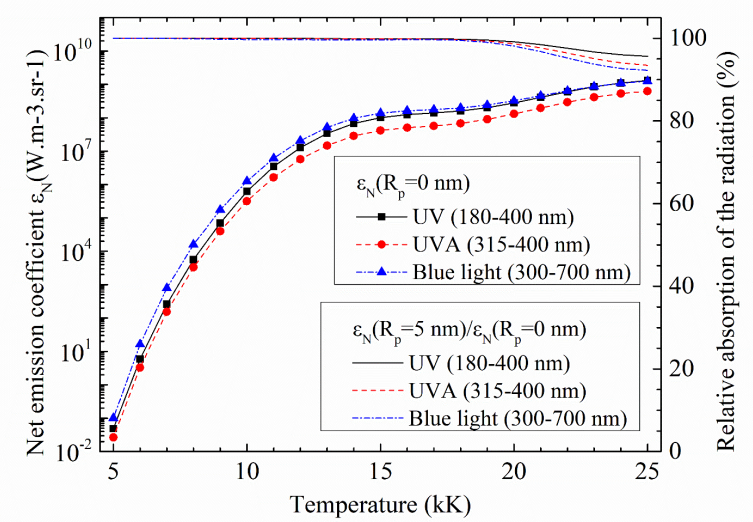

Fig. 5.5 Net emission coefficients (line and symbol) and the self-absorption phenomena (line) for the UV, UVA and blue light spectral regions

5.3 Modelling of GTAW arcs

A two-dimensional axisymmetric model of a GTAW arc in interaction of a tungsten electrode and a water-cooled copper anode was developed to determine the arc temperature for a spot GTAW welding process. Based on the relations of the EECs with the temperature (figure 5.4), the EEC distributions in the arc were further obtained for the UV, UVA and blue light radiation.

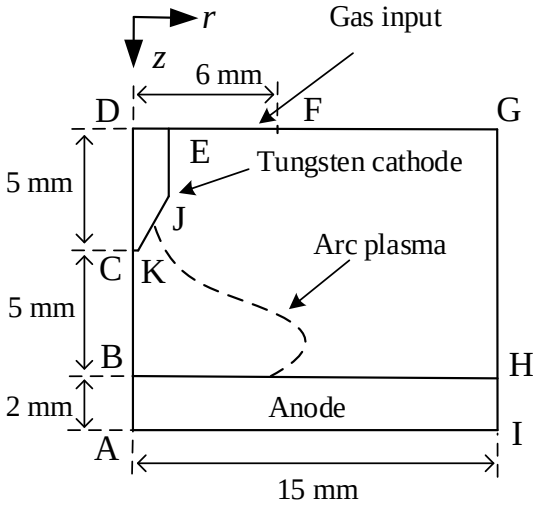

Fig.5.6 Geometric configuration of GTAW arc and electrodes.

The geometric configuration of the GTAW arc and electrodes is shown in figure 5.6. The tungsten electrode has a diameter of 3.2 mm and a conical angle of 60 °, while its extreme tip is flattened to be a flat with a radius of 0.2 mm. The copper plate with a thickness of 2 mm is perpendicular to the tungsten electrode. The shielding gas of argon flows at a rate of 10 L/min. The arc plasma struck between the two electrodes is assumed to be a laminar flow in LTE. The Boundary conditions are given in table 5.2. To investigate the effect of arc length, geometric configurations with arc lengthes (CB)— 2.5 mm, 5 mm (figure) and 7.5 mm— are created, corresponding to short arc, middle arc and long arc, repectively. Also, the welding current varies from 50 A, 100 A to 200 A, corresponding to low current, middle current and high current, repectively.

Table 5.2. Boundary conditions.

	velocity, v ($m\ s^{-1}$)	temperature, T (K)	Electrical potential, V (V)	Magnetic potential vector, A (T m)
ABCD	$\partial v/\partial r=0$	$\partial T/\partial r=0$	$\partial V/\partial r=0$	$\partial A/\partial r=0$
DE	v=0	T=2500	I=50, 100, 200 A	$\nabla A\cdot e_n=0$
EF	ρv=10 L/min	$\nabla T\cdot e_n=0$	$\nabla V\cdot e_n=0$	$\nabla A\cdot e_n=0$
FG-GH	压力出口	T=300	$\nabla V\cdot e_n=0$	A=0
AI	v=0	T=300	V=0	$\nabla A\cdot e_n=0$
HI	v=0	T=300	$\nabla V\cdot e_n=0$	A=0
BH	v=0	Eq. 5	$\nabla V\cdot e_n=0$	-
CKJE	v=0	Eq. 6	$\nabla V\cdot e_n=0$	-

5.3.1 Basic equations

The arc properties (temperature, pressure, velocity, electrical potential and magnetic potential) are described by magnetic fluid dynamics equations, including the conservation of mass, momentum, energy, electrical potential and magnetic potential. These equations can be written as a general expression for a variable Φ[165]:

$$\underbrace{\frac{\mathrm{d}\rho\Phi}{\mathrm{d}t}}_{\text{transient term}}+\underbrace{\nabla\cdot(\rho\boldsymbol{v}\Phi)}_{\text{convection term}}=\underbrace{\nabla\cdot(\Gamma\nabla\Phi)}_{\text{diffusive term}}+\underbrace{S_\phi}_{\text{Source term}} \tag{5.14}$$

Where ρ is he mass density, $\boldsymbol{v}$ is the velocity vector, Γ is the general diffusivity, and S_Φ is the source term. The paramters of Φ, Γ and S_Φ are given in table 5.3.

As an example, the energy conservation equation is given by[166]

$$\underbrace{\frac{\mathrm{d}\rho h}{\mathrm{d}t}}_{\text{transient term}} + \underbrace{\nabla\cdot(\rho \boldsymbol{v} h)}_{\text{convection term}} = \underbrace{\nabla\cdot\left(\frac{\kappa}{c_\mathrm{p}}\nabla h\right)}_{\text{diffusive term}} + \underbrace{\frac{\boldsymbol{j}\cdot\boldsymbol{j}}{\sigma} - 4\pi\varepsilon_\mathrm{N}}_{\text{Source term}} \tag{5.19}$$

Where h is the enthalpy, with $\mathrm{h} = \int c_\mathrm{p}\mathrm{d}T$, c_p is the specific heat, κ is the thermal conductivity, σ is the electrical conductivity, $\boldsymbol{j}$ is the current density, φ is the electrical potential, and ε_N is the NEC of entire spectral spectrum (R_p=1 mm).

Table 5.3. MHD Equations

Conservation equation	Φ	Γ	S_Φ
Mass	1	0	0
Momentum	$\boldsymbol{v}$	η	$-\nabla p+\boldsymbol{j}\times\boldsymbol{B}$
Energy	h	κ/c_p	S_T
Electrical potential	σ	φ	0
Magnetic potential	1	$\boldsymbol{A}$	$-\mu_0\boldsymbol{j}$

5.3.2 Electrode surfaces

Physically, there exist thin layers (space-charge regions) at the arc-electrode interfaces, where the plasma is not in LTE[167]. To ensure the electricity transition in these zones, the "simplified unified model" of Lowke[166] was used in our modelling. Also, special energy boundaries were added to treat the heat transfer at these interfaces.

Calculations on the cathode electrode surface need to include the special processes occurring at the surface, namely cooling due to the thermionic emission, heating due to ion current and heat conduction. The heat effect due to the radiation from the arc to the electrode and from the electrode to external space is neglected. As a consequence, the thermal flux from the arc to the cathode electrode (tungsten) is given by[8]

$$q_\mathrm{c} = |j_\mathrm{i}|V_\mathrm{i} - |j_\mathrm{e}|\phi_\mathrm{c} - \kappa\frac{\partial T}{\partial n} \tag{5.20}$$

Where

$$|j_e|=\begin{cases} j_R & \text{if}(|\boldsymbol{j}\cdot\boldsymbol{n}|-j_R)>0 \\ |\boldsymbol{j}\cdot\boldsymbol{n}| & \text{if}(|\boldsymbol{j}\cdot\boldsymbol{n}|-j_R)\leq 0 \end{cases};\ |j_i|=|\boldsymbol{j}\cdot\boldsymbol{n}|-|j_e| \tag{5.21}$$

with

$$j_R=A\cdot T_c^2\exp\left(-\frac{e\phi_a}{k_B T}\right) \tag{5.22}$$

Thermal flux from the arc to the anode electrode (workpiece) is given by[8]

$$q_a=|\boldsymbol{j}\cdot\boldsymbol{n}|\phi_a-\kappa\frac{\partial T}{\partial n} \tag{5.23}$$

Since large temperature differences exist between the temperature of the electrode temperature and the adjacent arc plasma, the thermal conductivity corresponding to those temperatures can vary by a factor of five or more. The function $S(T)=\int\kappa \mathrm{d}T$ within the electrode sheaths was used to avoid large numberial errors that could result from this effect. This method was first proposed by Lowke[166].

As $\kappa=\mathrm{d}S/\mathrm{d}T$, thermal conduction flux density $\kappa\mathrm{d}T/\mathrm{d}z=\mathrm{d}S/\mathrm{d}z$ and the conduction flux across a mesh length Δz is $(S_2-S_1)/\Delta z$, where S_1 and S_2 are the values of S at the end points of the segment Δz. The effective average thermal conductivity κ_{av} across Δz is obtained by equating $\kappa_{av}(T_2-T_1)/\Delta z=(S_2-S_1)/\Delta z$ so that $\kappa_{av}=(S_2-S_1)/(T_2-T_1)$. Values of S as a function of temperature were obtained by intergrating κ numerically with respect to temperature. The data of the heat conductivity κ for argon plasma were taken from Cressault *et al*[12]. The values of S were stored in tabular form,

5.3.3 Numerical solution

The commercial software of FLUENT 14.5 with a finite volume method was used for the computation solution. The pressure-based solver was chosen due to the fact that the variation of pressure in GTAW arcs is less than 1%[168], and a simple algorithm was used. The solution took about 9 minutes with an Inter(R) I7 7500 U computer.

Since there may be some difficulties in the treatment of heat transfer between the plasma-electrode interfaces and in the processes from local temperature to effective irradiance, some codes used in Fluent software are presented in table 5.4.

Table 5.4. C Programs used in Fluent

```
/*Program 1: Heat Flux into the workpiece (water-cooled copper anode) */
DEFINE_PROFILE (Heatflux_WorkpieceArc, t, i)
 {
   /*Define the parameters*/
       Domain *d=Get_Domain (1);
       Thread *wall_t=Lookup_Thread (d, F1); /* interface: Workpiece-Arc; adjacent to Workpiece */
       Thread *wall_shadow_t=THREAD_SHADOW(wall_t); /* get the wall shadow thread */
       Thread *wall_cell_t, *shadow_cell_t;
       cell_t wall_c, shadow_c;
       face_t f, f_shadow;
       real q_con, q_ele; /*Heat flux of conduction heat, electron heat*/
       real T_cu, T_arc; /* temperatures of anode sureface and its adjacent arc*/
       real S_arc, S_cu; /* S (T) at the temperatures at anode sureface and its adjacent arc*/

      /*qcond_anode= (S(Tarc)-S(Tcu)) *condf_cu (in m-1), S(T) (in W.m-1); */

       begin_f_loop (f, wall_t) /* loop over all the faces */
       {
           wall_cell_t=THREAD_T0(wall_t); /* get the cell zone */
           wall_c=F_C0(f, wall_t);
           f_shadow=F_SHADOW (f, wall_t); /* get the corresponding face in the shadow thread */
           shadow_cell_t=THREAD_T0(wall_shadow_t); /* get the cell sone in the shadow side */
           shadow_c=F_C0(f_shadow, wall_shadow_t);

           T_cu=C_T (wall_c, wall_cell_t);
           T_arc=C_T (shadow_c, shadow_cell_t);
           if (T_arc <= 3000.)
                S_arc=-7.58463+0.01777*T_arc+1.28E-05*T_arc*T_arc;
           else
               {S_arc=intp (S_cond, T_arc);}
           if (T_cu <= 3000.)
                S_cu=-7.58463+0.01777*T_cu+1.28E-05*T_cu*T_cu;
           else
               {S_cu=intp (S_cond, T_cu);}
           q_con=(S_arc-S_cu) *condf_cu; /* qcond_anode= condf_cu *(S_arc-S_cu) */

           q_ele= (C_UDMI (wall_c, wall_cell_t,1) +C_UDMI (shadow_c, shadow_cell_t,1)) *0.5*EpCu;

           F_PROFILE (f, t, i) =q_con+q_ele; /* positive value*/
       }
   end_f_loop (f, wall_t)
 }
```

```
/*Program 2: radiations emited from the arc and their effective irradiances within UV, UVA and blue light zones */

DEFINE_ON_DEMAND(Calculate_Radiation)
 {
    /* E_eff= (Rd /Rd) *(∫ε_eff(T)* dV); E_eff< H_limit/t */
    /* X(λ)= S(λ) for 180<λ<400 nm (UV); X(λ)=1 for 315<λ<400 nm (UVA); X(λ)=B(λ) for 300<λ<700 nm (Blue light) */
    /*ε_eff(T)=∫ε_λ(T)*X(λ) *dλ; ε_eff(T) is noted as EEC */

    /*Define the parameters*/
     real volume; /*volume of one mesh*/
        /* radiation emited from the arc within UV, UVA and blue light zones*/
     real Heat_rad_UV, Heat_rad_UVA, Heat_rad_Blue;
     real E_eff_UV, E_eff_UVA, E_eff_Blue; /*Effective illuminances within UV, UVA and blue light zones*/
     real Rd; /*distance between the arc to the body surface, Unit: m*/

     Domain *d;
     Thread *t;
     cell_t c;
     d = Get_Domain (1); /* Get the domain using ANSYS FLUENT utility */

     Rd =0.5;
     thread_loop_c (t, d)
      {
        begin_c_loop (c, t)
          {
              volume = C_VOLUME (c, t); /* get cell volume */
              Vol_tot += (2*Pi*volume);

              Heat_rad_UV     += (2*Pi*volume) * Rad_UV;
              Heat_rad_UVA    += (2*Pi*volume) * Rad_UVA;
              Heat_rad_Blue   += (2*Pi*volume) * Rad_Blue;

              E_eff_UV    += (2*Pi*volume) * EEC_UV;
              E_eff_UVA   += (2*Pi*volume) * EEC_UVA;
              E_eff_Blue += (2*Pi*volume) * EEC_Blue;
          }
        end_c_loop (c, t)
      }
     E_eff_UV =E_eff_UV /Rd/Rd;
     E_eff_UVA =E_eff_UVA /Rd/Rd;
     E_eff_Blue =E_eff_Blue /Rd/Rd;
```

```
    Printf ("Rad_UV = %g W; Rad_UVA = %g W; Rad_Blue = %g W; \n\n", Heat_rad_UV, Heat_rad_UVA, Heat_rad_Blue);
    Printf ("Rd= %g m; E_eff_UV = %g W.m-2; E_eff_UVA = %g W.m-2; E_eff_Blue = %g W.m-2 \n", Rd, E_eff_UV, E_eff_UVA, E_eff_Blue);
}
```

5.4 Results and discussion

5.4.1 Local emission in the arc

The arc properties, such as temperature, pressure, velocity and emission, have been modelled for GTAW arcs. Considering that arc temperature is associated with emission and is relatively easy to measure, the modelled temperature field is compared with previous experimental data for a typical GTAW arc (200 A and 5 mm arc length) to validate our modelling, as shown in figure 5.7. It can be seen that there is an agreement with the measurement of Haddad and Farmer[169] in all regions except the region near the tungsten electrode. The discrepancy near the tungsten electrode may be due to the fact that in measurement mild fusion deformation occurs at the electrode tip, which would influence the flow of current near the electrode and thus the arc temperature. This phenomenon has also been predicted in our modelling since our maximum electrode temperature (4120 K) is above the melting point of tungsten (3680 K), although the deformation was not taken into account in this model. Hence, this discrepancy is acceptable.

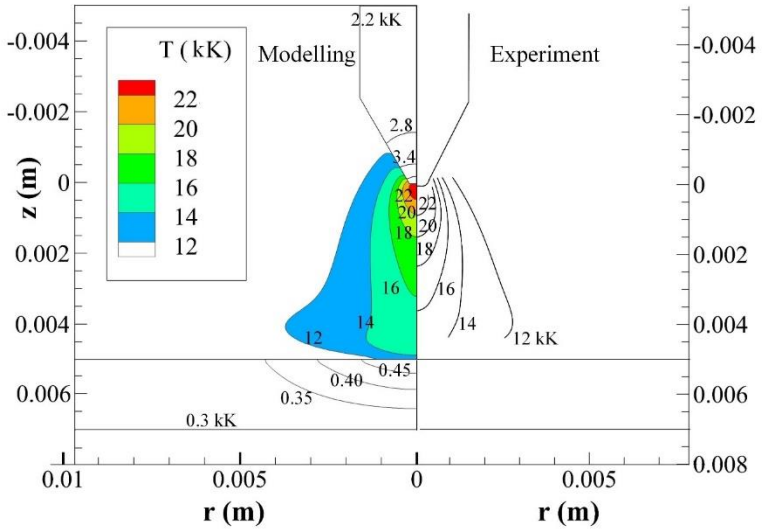

Fig. 5.7. Comparison between calculated isotherms (left) and experimental isotherms[169] (right) for a TIG arc (*I*=200 A).

Figure 5.8(a)-(c) show the results for the distributions of the 4π*NEC (left) and the 4π*EEC (right) in a 50 A,100 A and 200 A GTAW arc for the UV region, respectively. Figure 5.9(a)-(c) shows for UVA region and figure 5.10(a)-(c) for blue light region. The 4π*NEC represents the local radiation loss, while the 4π*EEC represents the local radiation loss that can cause photobiological hazards. It can be seen from all these figures that for the three spectral intervals the NEC and the EEC always decrease away from the arc axis, and the maximum values always appear below the tungsten electrode. When the welding current changes, this phenomenon still appears. This is due to the fact that the EEC and the NEC increase with temperature below 25000 K (figure 5.4-5.5) and that the arc temperature presents

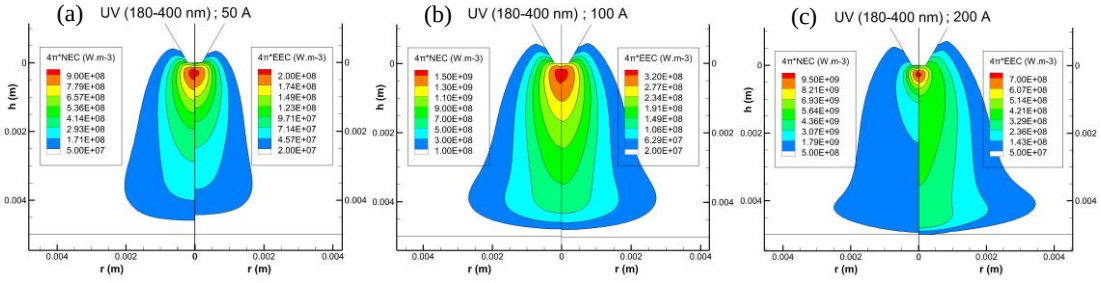

Figure 5.8. Distributions of the 4π*NEC and the EEC in a GTAW arc with a current of 200 A and an arc length of 5 mm. **(a)** 50 A. **(b)** 100 A. **(c)** 200 A.

(a) (b) (c)

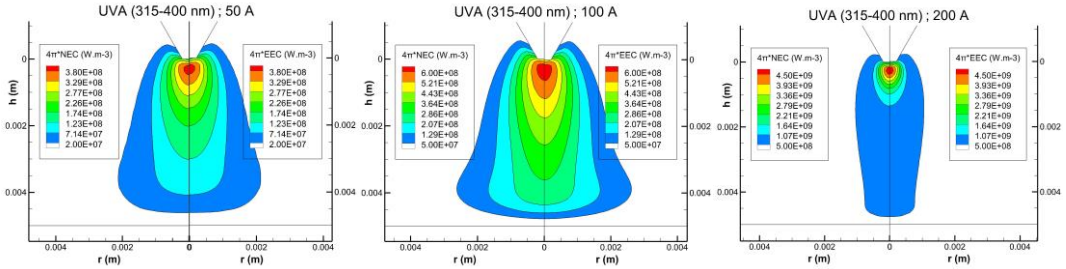

Figure 5.9. Distributions of the 4π*NEC and the EEC in a GTAW arc with a current of 200 A and an arc length of 5 mm. **(a)** 50 A. **(b)** 100 A. **(c)** 200 A.

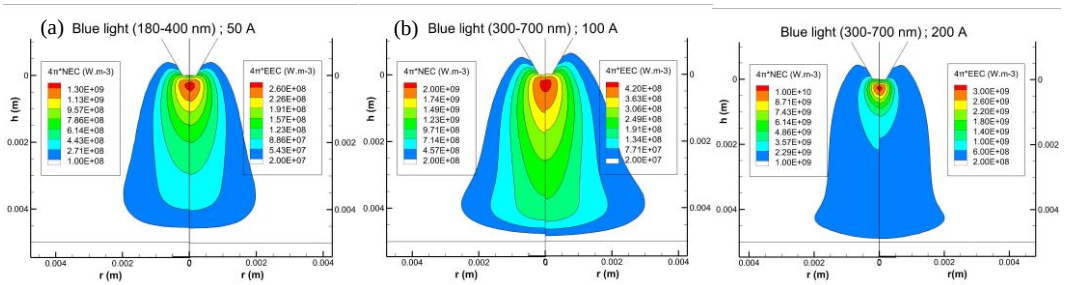

Figure 5.10. Distributions of the 4π*NEC and the EEC in a GTAW arc with a current of 200 A and an arc length of 5 mm. **(a)** 50 A. **(b)** 100 A. **(c)** 200 A.

5.4.2 Effective irradiances from GTAW arcs

The effective irradiances can be obtained from the EEC distributions according to Eq. (5.7). Since welding current and arc length are two important parameters for GTAW welding, figure 5.11(a)-(c) highlight the influence of these two parameters on the effective irradiance for the UV, UVA and blue light radiation, respectively. To validate our modelling results, Figure 8 also gives a comparison of our predictions with the experimental data from Nakashima *et al*[170] for the UV radiation; however, no experimental data has been found for the UVA and blue light radiation.

As can be seen in figure 5.11(a)-(c), the effective irradiances on a surface at 0.5 m outside increase with the welding current I and the arc length L for three spectral intervals, especially in the case of middle current (100 A) and high current (200 A). This phenomenon is related to the temperature and the volume of the high temperature zone in the arc, since the EEC increase with temperature for the three spectral intervals (figure 5.4). Table 2 lists the maximum arc temperatures T_{max} and the high temperature zone volumes *Vol_hot* (T>12000 K) for various welding conditions. It can be seen from table 2 that the increase of current leads to high values of T_{max} and *Vol_hot*; the increase of arc length has little effect on the T_{max}; however, it can

significantly increase the *Vol_hot*. All of these increases the effective irradiances. Figure 5.11 also indicates that under the premise of good welding quality, the use of a short arc and a low current is profitable for the decrease of the optical radiation.

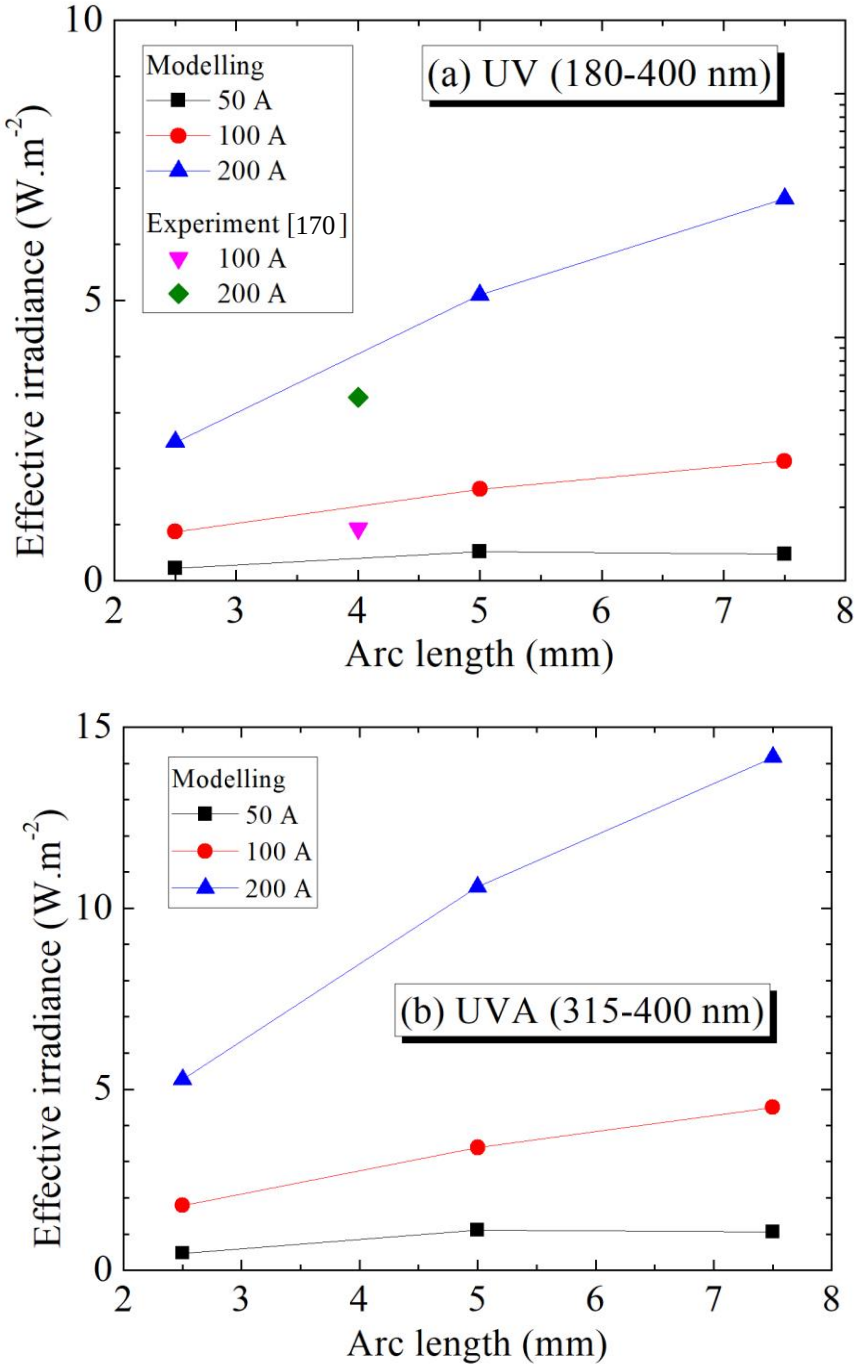

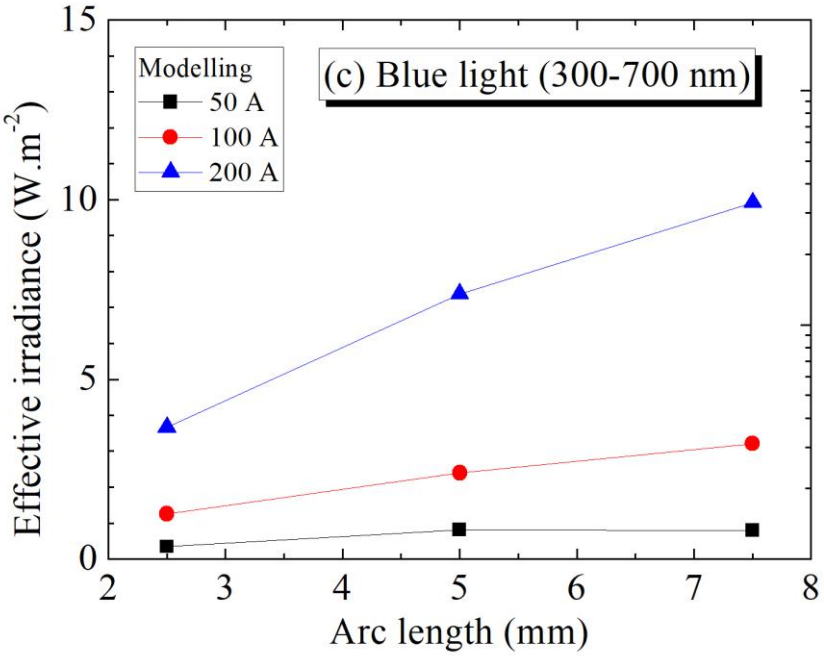

Figure 5.11. Effective irradiances caused by the GTAW arcs 0.5 m outside with different welding current and arc length. **(a)** UV. **(b)** UVA. **(c)** blue light.

Table 5.4. Maximum temperature and volume of high temperature zone (T>12000 K) for GTAW arcs.

	I=50 A		I=100 A		I=200 A	
	T_{max} (K)	*Vol_hot* (m^{-3})	T_{max} (K)	*Vol_hot* (m^{-3})	T_{max} (K)	*Vol_hot* (m^{-3})
L=2.5 mm	13728.7	6.56×10^{-9}	16097.3	2.22×10^{-8}	22868.4	4.76×10^{-8}
L=5.0 mm	14245.0	1.26×10^{-8}	16172.8	4.55×10^{-8}	22850.9	1.09×10^{-7}
L=7.5 mm	13923.1	6.55×10^{-9}	16191.9	6.11×10^{-8}	22904.9	1.60×10^{-7}

As shown in figure 11(a), our modelling results basically agree with the experimental data from Nakashima *et al* [170] for a 4 mm GTAW arc, although their values seem to be slightly lower. This discrepancy may result from that some part of radiation would be blocked out by the tungsten electrode in measurement, while this radiation has been counted in our modelling. Overall, our model gives a satisfactory prediction.

5.4.3 permissive exposure durations

The permissive exposure durations can be further determined according to the Directive 2006/25/EC. Figure 5.12 shows the results for the UV, UVA and blue permissive exposure durations dependence on the distance from a GTAW arc (200 A and 5 mm arc length), as an example. It can be seen that the permissive exposure

duration of UV is far less than that of blue light and UVA, which means the UV radiation is most hazardous among these spectra. Besides, the UV permissive exposure duration can be reached in a short time (from seconds to minutes), e.g., from 5.89 s to 9.8 minutes at the distances from 0.5 m to 5 m. It indicates the workers in the welding environment are easy to suffer an extreme UV radiation.

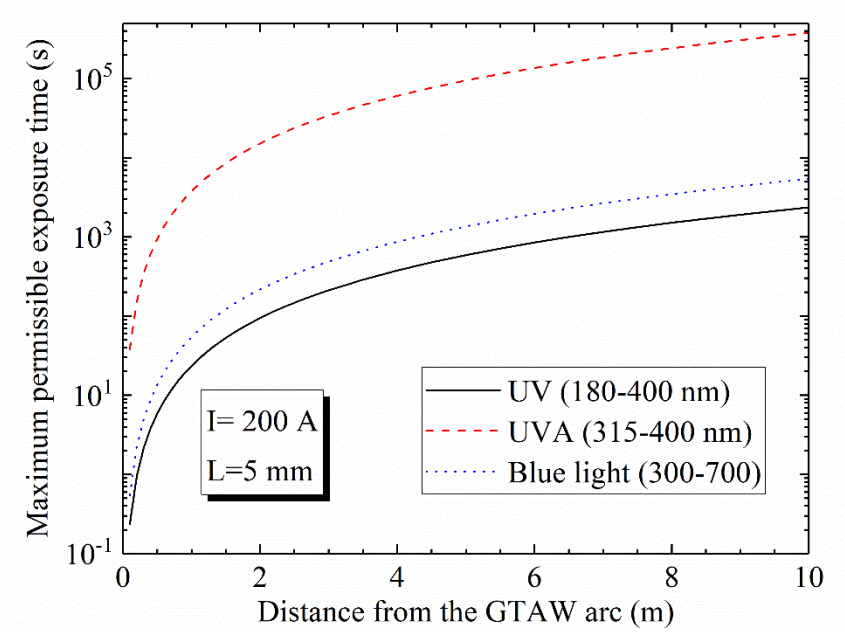

Figure 5.12. Maximum permissible exposure time versus the distance from a GTAW arc (*I*=200 A and *L*=5 mm) for the UV, UVA and blue light radiation.

Personal control measures, such as welding helmets and industrial clothing, must be adopted to minimize the exposure. For most welding processes, the UV transmittances of recommended welding helmet filters (shadow number from 7 to 14) are less than 0.007% [161]. Sliney *et al* [171] found that the transmittances of most industrial clothing are less than 0.01% for UV radiation. For a 200 A and 5 mm GTAW arc, the maximum effective irradiance at a distance of 0.5m is 5.10 $W.m^{-2}$ and its 8-hour radiant exposure is 1.47×10^{5} $J.m^{-2}$. The radiant exposures per day through a welding helmet and an industrial clothing are less than 10.3 J. m^{-2} and 14.7 J. m^{-2}, respectively. These values are within the exposure limit (30 $J.m^{-2}$), which means that welding helmets and industrial clothing can provide adequate UV protection if workers are well covered.

However, it has been found that welders do report high rates of ocular and skin symptoms associated to high UV exposure levels [172-174]. Typical protection failures exist in the following cases: welders raise their filters before arc striking since the luminous transmittance of welding filters is very low; the UV radiation may infiltrate

welding helmets from the rear due to the exposure to a nearby operation [48]; skin areas (e.g. face, neck and hands) are uncovered by clothing. Our present study is expected to provide some guidance for the further design of these protection measures.

5.5 Conclusion

This chapter is devoted to investigate the UV (180-400 nm), UVA (315-400 nm) and blue light (300-700 nm) optical radiation associated with photobiological hazards for argon GTAW arcs, based on the analysis of the radiative transfer process, the calculation of radiative properties and the modelling of GTAW process. The following conclusions are reached:

(1) The effective irradiance caused by a GTAW arc depends on the distance from the arc (R_d), the effective emission coefficient (ε_{eff}) and its distribution in the arc. The ε_{eff}, defined as a wavelength integrated emission coefficient that takes the biological weighting into account, was calculated in our work.

(2) For the UV, UVA and blue light radiation, the effective emission coefficients (ε_{eff}) in GTAW arcs decrease from the arc axis and their maximum values are always located below the electrode and on the axis.

(3) The effective irradiances of the UV, UVA and blue light radiation increase with the welding current and the arc length, especially in the case of middle and high currents.

(4) The UV radiation is hazardous due to its very short permissive exposure duration. For a typical GTAW arc (200 A and 5 mm arc length), the UV permissive exposure duration at distances from 0.5 m to 5 m outside the arc ranges from 5.89 s to 9.8 minutes.

This work also indicates the importance of implementing and developing effective protection measures for workers in the welding environment. Besides, in spite of the preliminary investigation of the hazardous radiation for argon GTAW arcs, present work should build a basis for further studies, such as the influence of the type of the shielding gases (Ar or He) and the influence of the metal vapours evaporated from the workpiece (e.g. iron steel) and possible filler rod on radiation for GTAW arcs, and the evaluation of the radiation emitted by GMAW arcs in which large

quantities of metal vapour is evaporated from molten wire electrode, leading probably to a significant increase the hazardous radiation. But taking into account metallic vapours requires the calculation of properties, the description of arc-material interactions and of ablation in the model. These improvements will be done in our forthcoming work.

General conculsion

This doctoral thesis involves two main research contents: (a) the introduction of a new method that allows a fast determination of space- and time-resolved plasma temperature and iron concentration in a MAG arc ([82%Ar-18%CO_2]-Fe mixtures)—CCD diagnostic method; (b) the study of the optical radiation associated with photobiological hazards posed by argon GTAW arc. Both of them are based on the study of plasma radiation properties. Also, in this thesis the investigation is performed for a typical MAG arc (pulsed MAG arc in one drop per pulse mode; 500 A) by use of the CCD diagnostic method and tradiational spectroscopic diagnostics. The general conculsion is summarized as follows:

(1) The spectra and the NEC in the temperature range 3-30 kK at 1 atm were obtained for [82%Ar-18%CO_2]-Fe plasmas representative of MAG arcs, which builts an interesting and useful database for the CCD diagnostic method. Besides, the NEC is also valuable data of radiation properties for the modelling of MAG arc, although the modelling work is not involved in this thesis.

(2) For the 82%Ar-18%CO_2 plasma, the radiation of molecular bands is important at low temperature (T<10 kK) and not self-absorbed in the plasma. At higher temperature, atomic lines contribute most to the radiation in spite of strong absorption, while the continuum radiation also assumes a considerable proportion. When a low iron concentration (e.g. 5%) exists in the plasma, the NEC is dramatically increased especially at low temperature. Atomic lines become the dominant contribution, thus causing continuum and molecular bands insignificant.

(3) For a typical MAG arc ([82%Ar-18%CO_2]-Fe plasmas, 500 A), LTE can be assumed in the arc expect in the arc fringe, where the electron temperature is higher than the excitation temperature by about 2000 K. In the main area of the arc, the plasma temperature decreases towards the arc axis and there is a temperature drop near the arc axis, which would be related to the strong cooling effect of the iron vapour in the arc. Although the temperature drop near the arc axis has also be found in the pulsed MIG arc in literature [12], it is

less steep in the pulsed MAG studied. It maybe results from that the iron vapour is more diffused in the MAG arc than in the MIG arc.

(4) It is possible to achieve a fast determination of the time-resolved fields of the temperature and iron vapour concentration in MAG arcs (with [82%Ar-18%CO_2]-Fe plasmas) by use of a high-speed CCD camera, as reported in this thesis. This method is based on the theoretical relations of $\varepsilon_{570\text{-}590\ nm}$ and $\varepsilon_{570\text{-}590\ nm}/\varepsilon_{607\text{-}627\ nm}$ with T and Y_{Fe} and based on the use of a monochrome high-speed CCD camera. By comparing the values of $\varepsilon_{570\text{-}590\ nm}$ and $\varepsilon_{570\text{-}590\ nm}/\varepsilon_{607\text{-}627\ nm}$ obtained by the arc images with the theoretical relations of $\varepsilon_{570\text{-}590\ nm}(T,Y_{Fe})$ and $\varepsilon_{570\text{-}590\ nm}(T,Y_{Fe})/\varepsilon_{607\text{-}627\ nm}(T,Y_{Fe})$, one can deduce the temperature and iron content in the arc. The CCD diagnostic method was validated by the Starking broadening method and the estimattion of iron content, suggesting that the new method can produce satisfactory results.

(5) The effective irradiance caused by a GTAW arc depends on the distance from the arc (R_d), the effective emission coefficient (ε_{eff}) and its distribution in the arc. The ε_{eff}, defined as a wavelength integrated emission coefficient that takes the biological weighting into account, was calculated in our work. For the UV, UVA and blue light radiation, the effective emission coefficients (ε_{eff}) in GTAW arcs decrease from the arc axis and their maximum values are always located below the electrode and on the axis.

(6) The effective irradiances of the UV, UVA and blue light radiation increase with the welding current and the arc length, especially in the case of middle and high currents. The UV radiation is hazardous due to its very short permissive exposure duration. For a typical GTAW arc (200 A and 5 mm arc length), the UV permissive exposure duration at distances from 0.5 m to 5 m outside the arc ranges from 5.89 s to 9.8 minutes. This work indicates the importance of implementing and developing effective protection measures for workers in the welding environment.

This doctoral thesis foucses on the arc diagostics, especially on the determation of the precense and concentration of iron vapour in a MAG arc. But in fact, there is still another big research content: the production and transfer of iron vapour in the arc. This work should be devoted to more energy, since it is the inner factor of the

precense of metal vapour. Besides, the effects of the composition of shielding gas on the arc is also an important research topic. For the photobiological hazards of arc welding, the radiation emitted by GMAW maybe also worthy of study, although it is often used automatically. Since it contains strong radiation element of metal vapour, its photobiological hazards maybe more ruinous.

Appendix I Equilibrium compositions of [82%Ar-18%CO_2]-Fe plasmas

The equilibrium compositions are presented in the following figures for [82%Ar−18%CO_2]−Fe plasmas with various iron concentrations (0.0%, 1%, 5%, 10%, 20%, 30%, …, 80%, 90%, 100% by mole) at 1 atm. The [82%Ar−18%CO_2]−Fe plasmas corresponds to the arcs occurring in MAG welding with the 82%Ar−18%CO_2 shielding gas and a steel wire, and some relevant hybrid welding processes such as hybrid laser-MAG welding. The relation of electron number density n_e with temperature T in plasmas with various iron concentrations Y_{Fe} can be extracted from the figures, and the relation of n_e-T-Y_{Fe} can be used in the spectroscopic determination of iron concentration by the Stark broadening method for MAG arcs (e.g. the pulse MAG arc presented in chapter 4) or related arcs (e.g. hybrid laser-MAG arcs) under LTE state. Also, the compositions built a basis for the calculation of plasma properties, such as mass density, specific heat and viscosity.

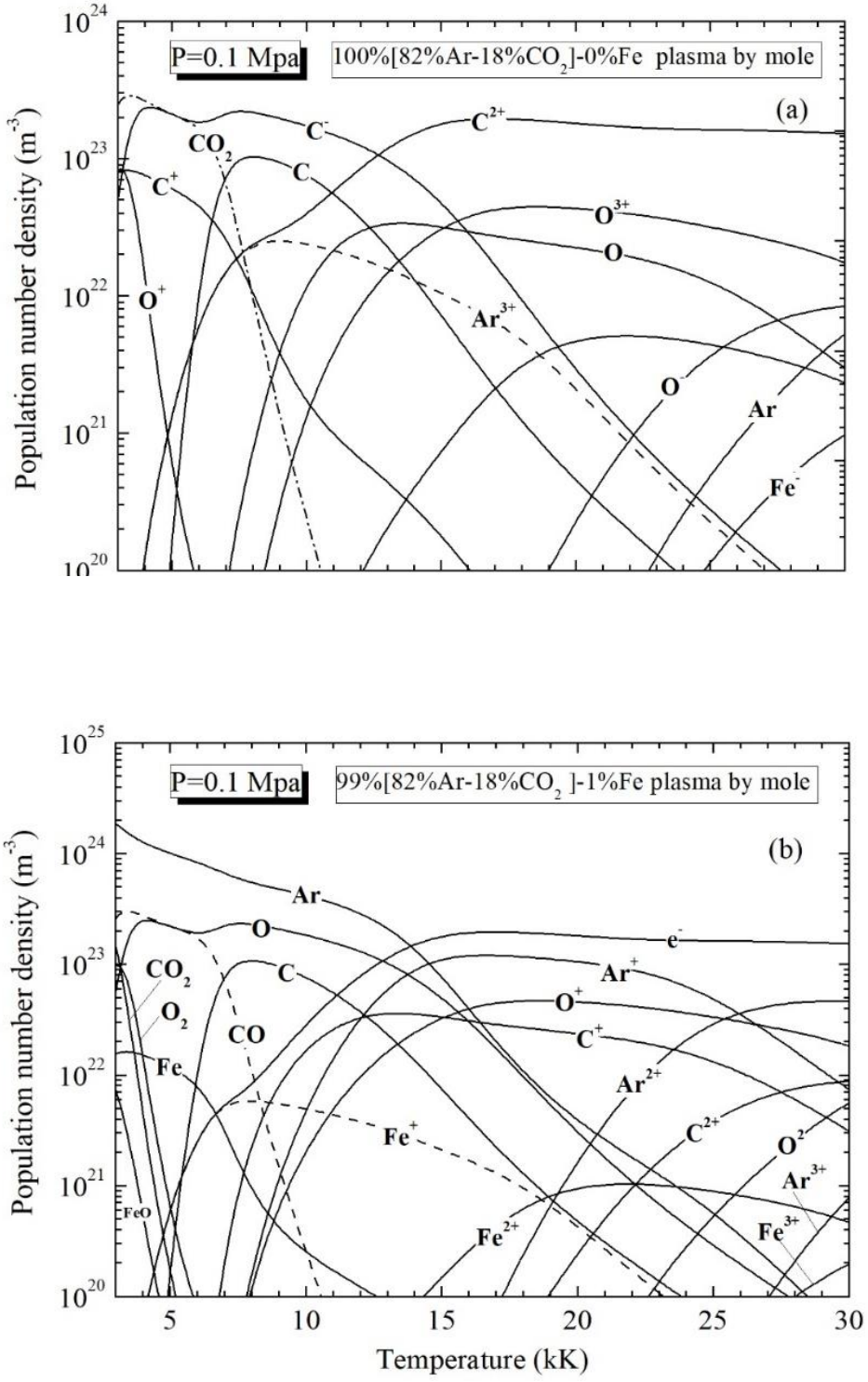
P=0.1 Mpa
100%[82%Ar-18%CO2]-0%Fe plasma by mole
(a)
Population number density (m-3)
C-
C2+
CO2
C
C+
O3+
O
O+
Ar3+
O-
Ar
Fe-
P=0.1 Mpa
99%[82%Ar-18%CO2]-1%Fe plasma by mole
(b)
Ar
O
e-
CO2
C
Ar+
O2
O+
CO
C+
Fe
Ar2+
Fe+
C2+
O2-
Ar3+
FeO
Fe2+
Fe3+
Temperature (kK)

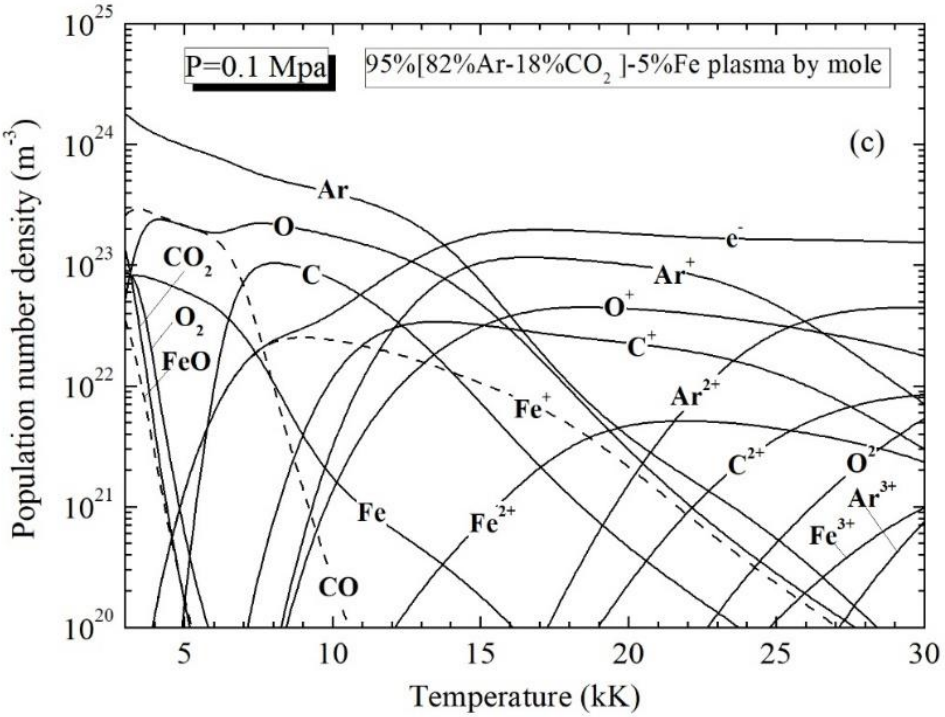
P=0.1 Mpa
95%[82%Ar-18%CO2]-5%Fe plasma by mole
(c)
Population number density (m-3)
Temperature (kK)
Ar
O
CO2
C
O2
FeO
Fe
CO
Fe+
Fe2+
e-
Ar+
O+
C+
Ar2+
C2+
O2
Ar3+
Fe3+

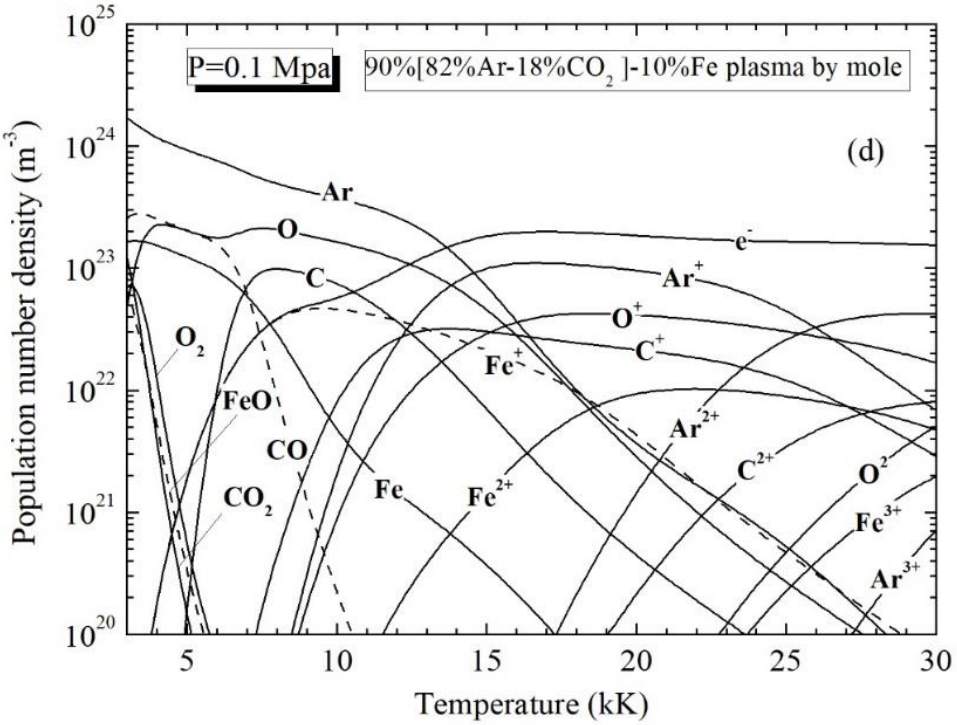
P=0.1 Mpa
90%[82%Ar-18%CO2]-10%Fe plasma by mole
(d)
Population number density (m-3)
Temperature (kK)
Ar
O
C
O2
FeO
CO
CO2
Fe
Fe+
Fe2+
e-
Ar+
O+
C+
Ar2+
C2+
O2
Fe3+
Ar3+

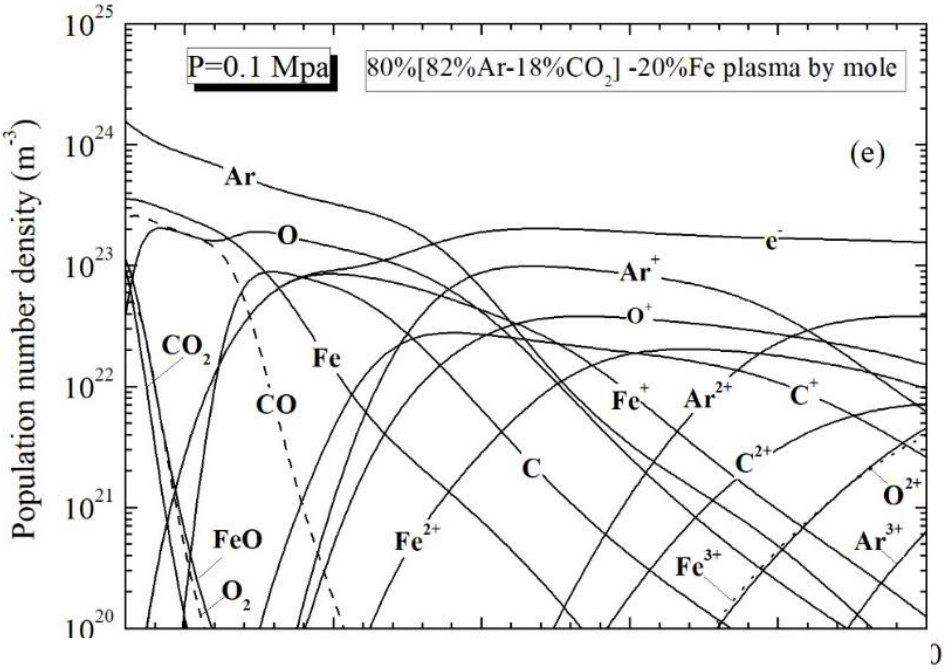
P=0.1 Mpa
80%[82%Ar-18%CO2] -20%Fe plasma by mole
(e)
Population number density (m-3)
Ar
O
e-
Ar+
O+
CO2
Fe
CO
Fe+
Ar2+
C+
C
C2+
O2+
FeO
Fe2+
Ar3+
O2
Fe3+

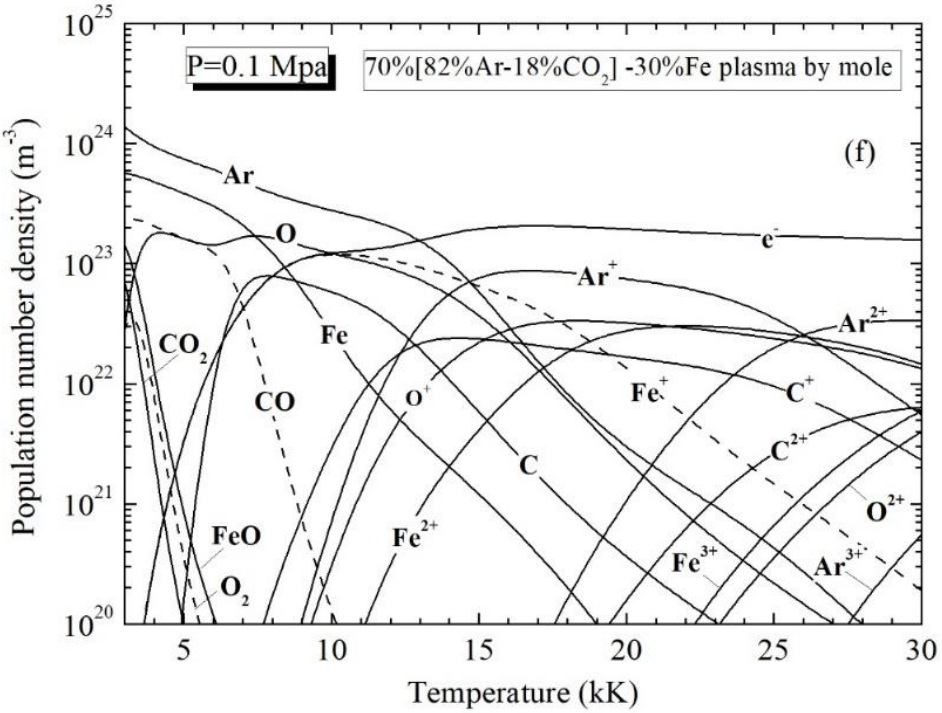
P=0.1 Mpa
70%[82%Ar-18%CO2] -30%Fe plasma by mole
(f)
Population number density (m-3)
Ar
O
e-
Ar+
Ar2+
CO2
Fe
CO
O+
Fe+
C+
C2+
C
O2+
FeO
Fe2+
Fe3+
Ar3+
O2
5
10
15
20
25
30
Temperature (kK)

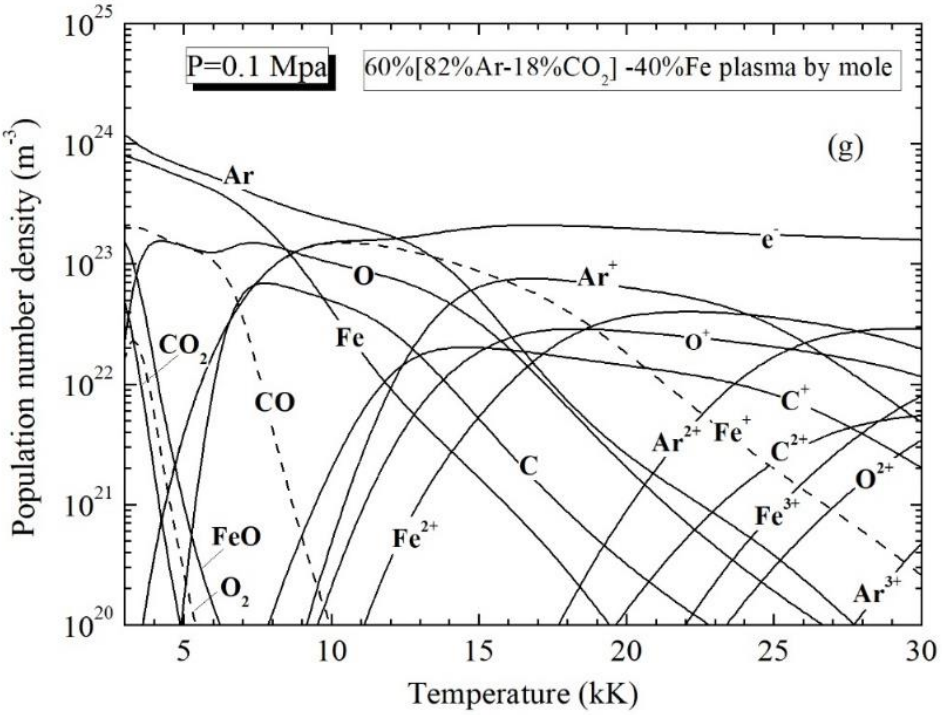
P=0.1 Mpa
60%[82%Ar-18%CO2] -40%Fe plasma by mole
(g)
Population number density (m-3)
Temperature (kK)
Ar
e-
O
Ar+
CO2
Fe
O+
CO
C+
Ar2+
Fe+
C2+
C
O2+
Fe3+
FeO
Fe2+
O2
Ar3+

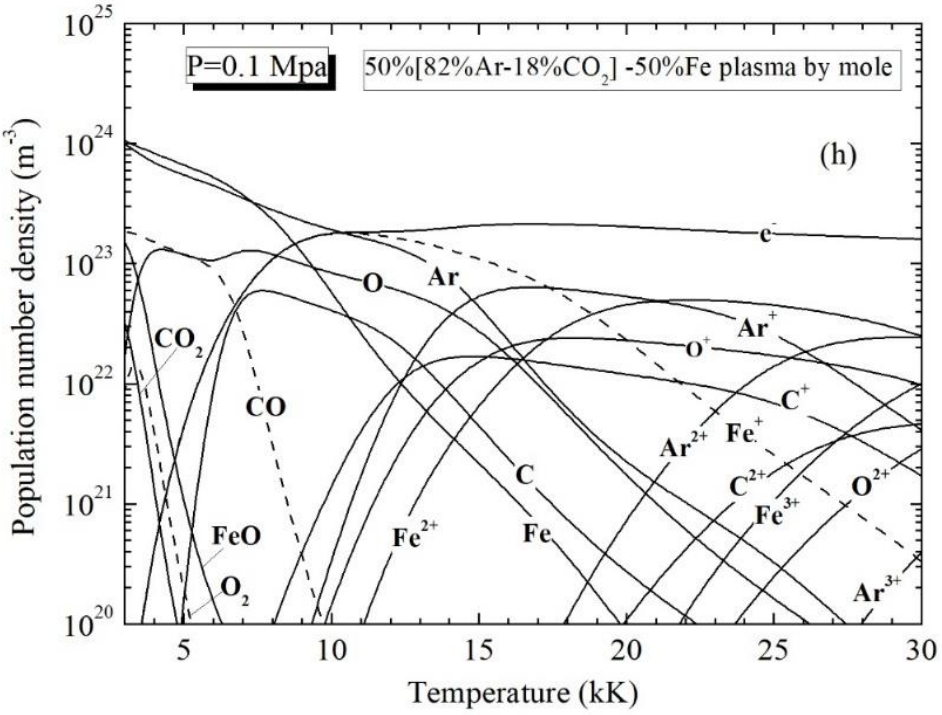
P=0.1 Mpa
50%[82%Ar-18%CO2] -50%Fe plasma by mole
(h)
Population number density (m-3)
Temperature (kK)
e-
O
Ar
Ar+
CO2
O+
CO
C+
Ar2+
Fe+
C
C2+
O2+
Fe3+
FeO
Fe2+
Fe
O2
Ar3+

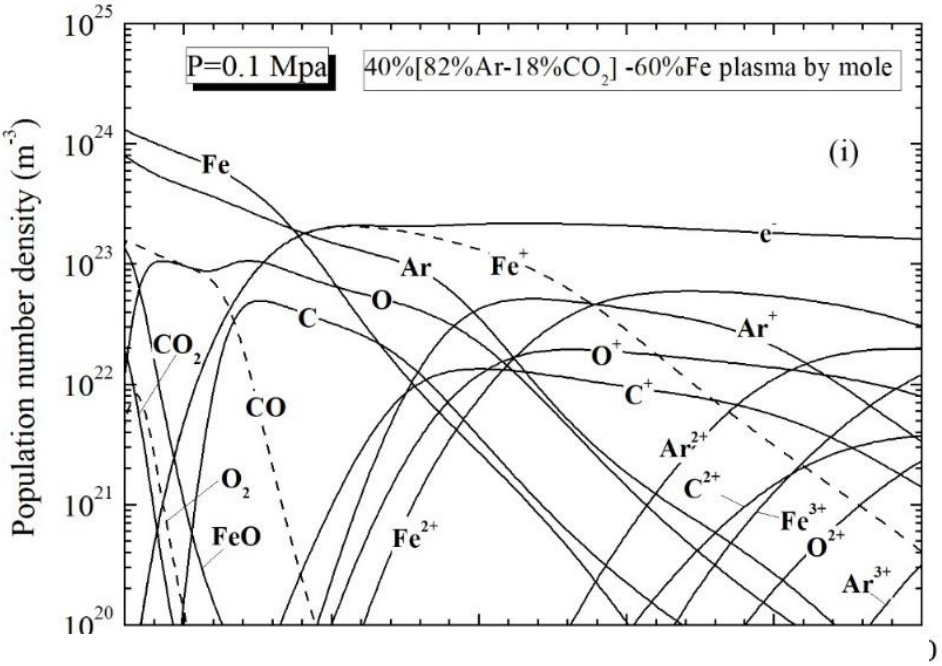
P=0.1 Mpa
40%[82%Ar-18%CO2] -60%Fe plasma by mole
(i)
Population number density (m-3)
Fe
e-
Ar
Fe+
O
C
Ar+
CO2
O+
C+
CO
Ar2+
C2+
O2
Fe3+
FeO
Fe2+
O2+
Ar3+

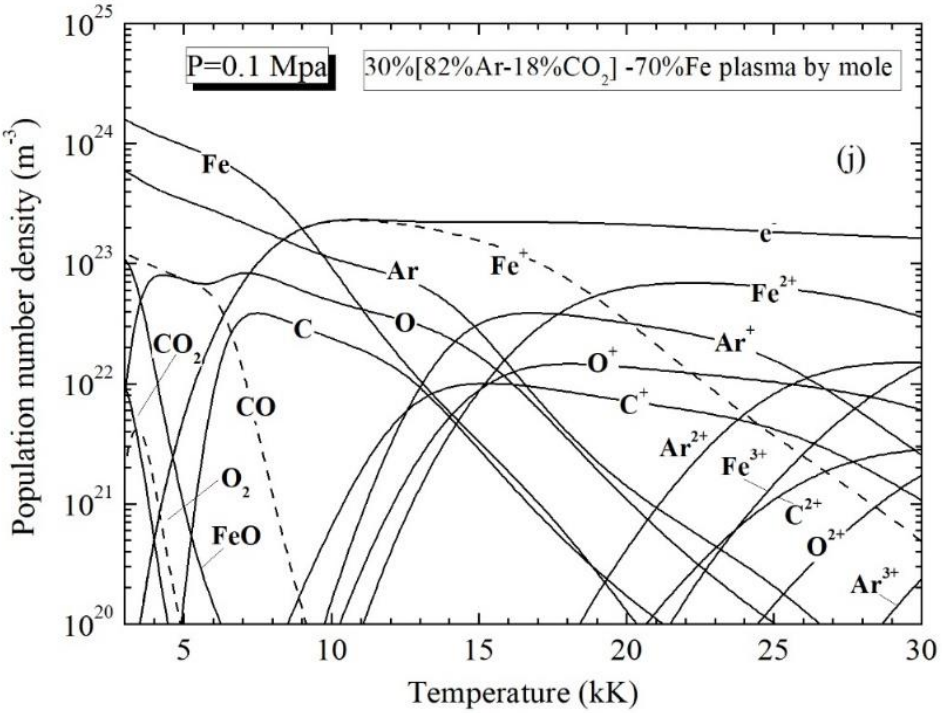
P=0.1 Mpa
30%[82%Ar-18%CO2] -70%Fe plasma by mole
(j)
Population number density (m-3)
Fe
e-
Ar
Fe+
Fe2+
O
C
Ar+
CO2
O+
C+
CO
Ar2+
Fe3+
O2
C2+
FeO
O2+
Ar3+
5
10
15
20
25
30
Temperature (kK)

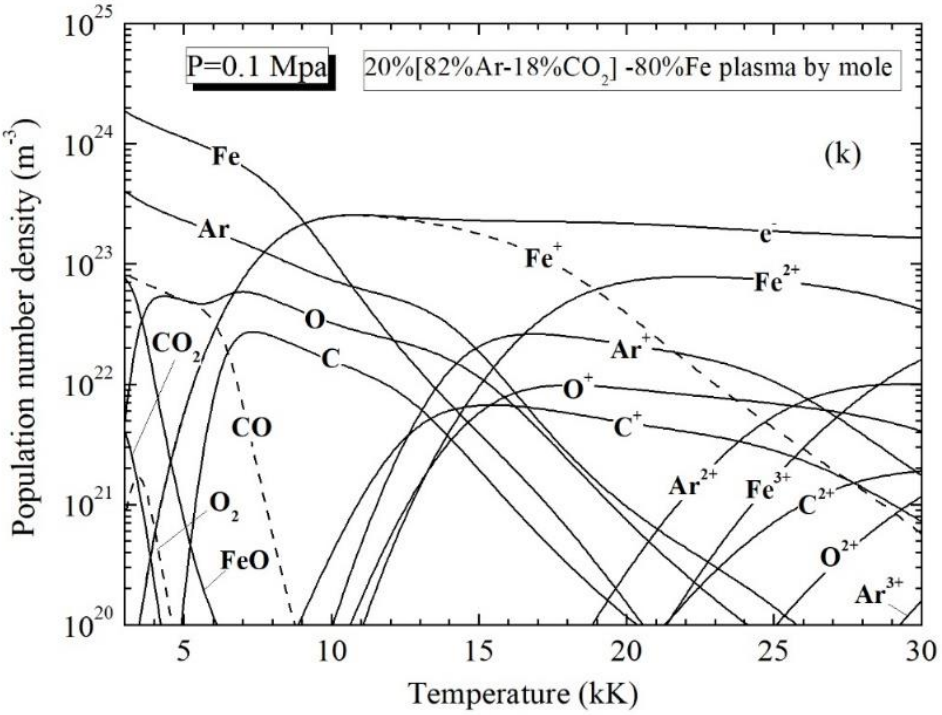
P=0.1 Mpa
20%[82%Ar-18%CO2] -80%Fe plasma by mole
(k)
Population number density (m-3)
Temperature (kK)
Fe
Ar
CO2
O
C
CO
O2
FeO
Fe+
e-
Fe2+
Ar+
O+
C+
Ar2+
Fe3+
C2+
O2+
Ar3+

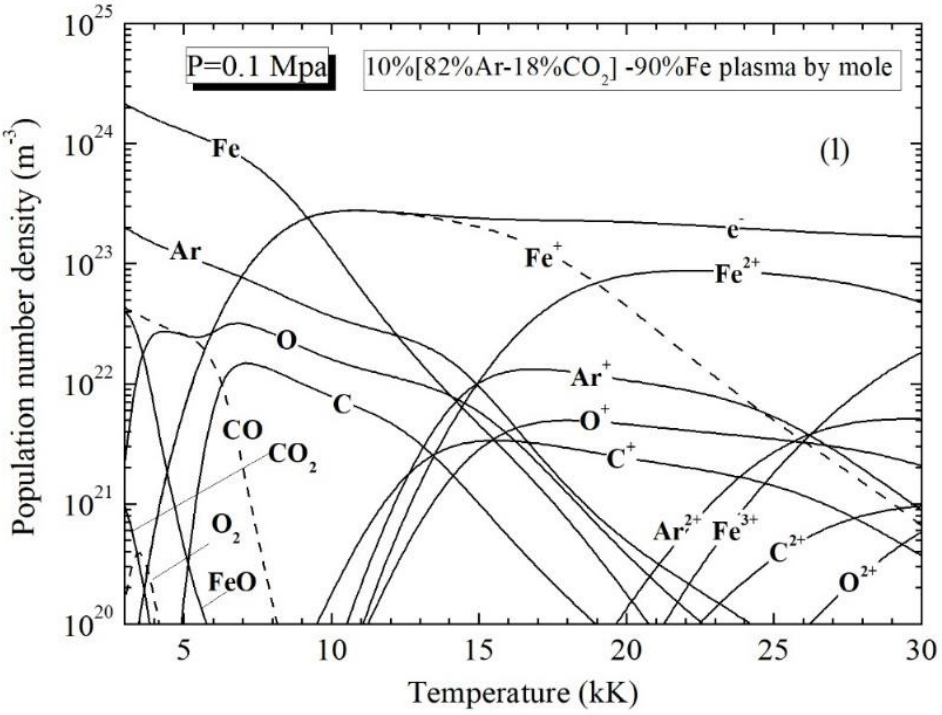
P=0.1 Mpa
10%[82%Ar-18%CO2] -90%Fe plasma by mole
(l)
Population number density (m-3)
Temperature (kK)
Fe
Ar
O
C
CO
CO2
O2
FeO
Fe+
e-
Fe2+
Ar+
O+
C+
Ar2+
Fe3+
C2+
O2+

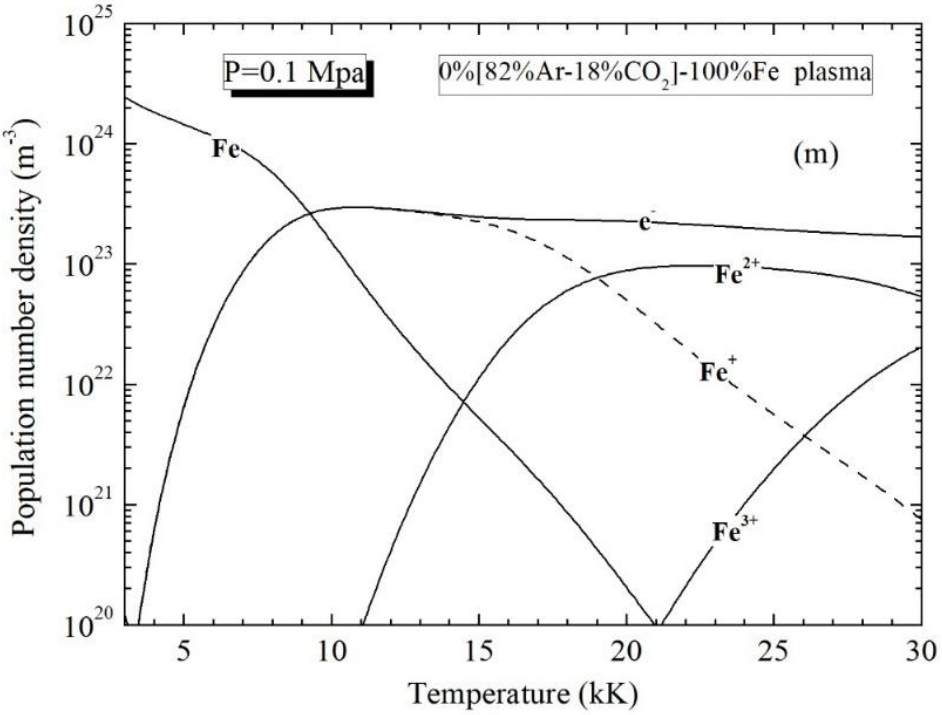

Figure AI.1. Equilibrium compositions of [82%Ar-18%CO_2]-Fe Plasmas. (a)-(m): with 0%, 1%, 5%, 10%, 20%, 30%, 40%, 50%, 60%, 70%, 80%, 90%, 100% Fe (by mole).

Appendix II Net emission coefficients of [82%Ar-18%CO2]-Fe plasmas

These tables below provide the net emission coefficients (NECs) for [82%Ar−18%CO_2]−Fe plasmas with various iron concentrations (0.0%，1%，5%，10%，20%，50%，80%，100% by mole) at 1 atm. The [82%Ar−18%CO_2]−Fe plasmas corresponds to the arcs occurring in MAG welding with the 82%Ar−18%CO_2 shielding gas and a steel wire, and some relevant hybrid welding processes such as hybrid laser-MAG welding. The calculation method is presented in the sections of 2.2 and 2.3. In spite of the rough assumptions adopted in the calculation method (LTE plasma, isothermal and homogeneous spherical plasma), the NEC values can be useful in the modelling of MAG arcs or other arcs related (e.g. laser-MAG arcs) because they correspond quite well to the radiative energy losses from the hottest regions of the plasma. An uncertainty of a factor of 2 on the NEC is acceptable: in arc modelling, the modification by a factor of 2 of the NEC leads to a rative temperature variation in the hottest regions of the orders of a few percent which corresponds to the experimental uncentranty obtained by optical spectroscopy.

Table AII.1. NECs for [82%Ar−18%CO_2]−Fe plasmas at R_p=0 mm (mole proportions, W. m^{-3}. sr^{-1})

T/kK	0.0%Fe	1%Fe	5%Fe	10%Fe	20%Fe	50%Fe	80%Fe	100%Fe
3	7.46E+04	1.90E+05	6.64E+05	1.30E+06	2.70E+06	7.80E+06	1.37E+07	1.79E+07
4	1.24E+04	4.26E+06	2.13E+07	4.33E+07	8.83E+07	2.34E+08	3.96E+08	5.14E+08
5	7.36E+04	3.48E+07	1.77E+08	3.62E+08	7.38E+08	1.93E+09	3.27E+09	4.24E+09
6	1.41E+06	1.22E+08	6.84E+08	1.43E+09	2.95E+09	7.85E+09	1.33E+10	1.73E+10
7	2.12E+07	2.17E+08	1.39E+09	3.08E+09	6.66E+09	1.85E+10	3.22E+10	4.28E+10
8	1.27E+08	3.86E+08	1.91E+09	4.38E+09	9.97E+09	2.95E+10	5.23E+10	6.96E+10
9	4.22E+08	8.35E+08	2.72E+09	5.58E+09	1.22E+10	3.56E+10	6.23E+10	8.17E+10
10	1.06E+09	1.71E+09	4.37E+09	7.91E+09	1.54E+10	3.99E+10	6.59E+10	8.38E+10
11	2.21E+09	3.16E+09	6.94E+09	1.17E+10	2.12E+10	4.87E+10	7.50E+10	9.18E+10
12	4.02E+09	5.28E+09	1.03E+10	1.66E+10	2.89E+10	6.32E+10	9.36E+10	1.12E+11
13	6.42E+09	7.97E+09	1.41E+10	2.19E+10	3.72E+10	8.07E+10	1.19E+11	1.43E+11
14	8.96E+09	1.07E+10	1.78E+10	2.67E+10	4.46E+10	9.76E+10	1.48E+11	1.79E+11

15	1.10E+10	1.30E+10	2.07E+10	3.05E+10	5.02E+10	1.11E+11	1.74E+11	2.16E+11
16	1.28E+10	1.48E+10	2.28E+10	3.31E+10	5.41E+10	1.20E+11	1.91E+11	2.42E+11
17	1.51E+10	1.71E+10	2.51E+10	3.53E+10	5.61E+10	1.23E+11	1.96E+11	2.48E+11
18	1.90E+10	2.08E+10	2.82E+10	3.76E+10	5.67E+10	1.18E+11	1.85E+11	2.34E+11
19	2.53E+10	2.69E+10	3.32E+10	4.12E+10	5.75E+10	1.10E+11	1.66E+11	2.07E+11
20	3.49E+10	3.62E+10	4.14E+10	4.77E+10	6.09E+10	1.03E+11	1.48E+11	1.81E+11
21	4.85E+10	4.95E+10	5.36E+10	5.86E+10	6.90E+10	1.02E+11	1.37E+11	1.62E+11
22	6.60E+10	6.68E+10	7.02E+10	7.42E+10	8.25E+10	1.09E+11	1.36E+11	1.55E+11
23	8.70E+10	8.77E+10	9.05E+10	9.38E+10	1.01E+11	1.22E+11	1.44E+11	1.60E+11
24	1.10E+11	1.10E+11	1.13E+11	1.16E+11	1.22E+11	1.41E+11	1.60E+11	1.73E+11
25	1.32E+11	1.33E+11	1.35E+11	1.38E+11	1.44E+11	1.62E+11	1.80E+11	1.92E+11
26	1.53E+11	1.54E+11	1.56E+11	1.59E+11	1.65E+11	1.83E+11	2.02E+11	2.15E+11
27	1.74E+11	1.74E+11	1.77E+11	1.80E+11	1.86E+11	2.05E+11	2.24E+11	2.38E+11
28	1.95E+11	1.95E+11	1.98E+11	2.00E+11	2.06E+11	2.24E+11	2.43E+11	2.57E+11
29	2.19E+11	2.19E+11	2.21E+11	2.23E+11	2.27E+11	2.42E+11	2.57E+11	2.68E+11
30	2.47E+11	2.62E+11	2.48E+11	2.48E+11	2.50E+11	2.56E+11	2.63E+11	2.69E+11

Table A2. NECs for [82%Ar−18%CO_2]−Fe plasmas at R_p=0.5 mm (mole proportions, W. m^{-3}. sr^{-1})

T/kK	0.0%Fe	1%Fe	5%Fe	10%Fe	20%Fe	50%Fe	80%Fe	100%Fe
3	7.44E+04	9.42E+04	1.25E+05	1.46E+05	1.83E+05	2.87E+05	3.94E+05	4.60E+05
4	1.22E+04	7.21E+05	1.72E+06	2.65E+06	4.15E+06	7.70E+06	1.06E+07	1.20E+07
5	5.85E+04	6.57E+06	1.70E+07	2.71E+07	4.35E+07	8.78E+07	1.16E+08	1.36E+08
6	9.41E+05	3.15E+07	9.63E+07	1.63E+08	2.77E+08	5.58E+08	7.99E+08	9.49E+08
7	4.50E+06	7.94E+07	3.16E+08	5.81E+08	1.05E+09	2.21E+09	3.19E+09	3.80E+09
8	8.78E+06	1.32E+08	6.12E+08	1.24E+09	2.42E+09	5.45E+09	7.98E+09	9.47E+09
9	2.89E+07	2.53E+08	9.65E+08	1.94E+09	3.94E+09	9.39E+09	1.39E+10	1.66E+10
10	1.00E+08	5.20E+08	1.62E+09	2.93E+09	5.58E+09	1.30E+10	1.93E+10	2.29E+10
11	2.84E+08	9.98E+08	2.81E+09	4.68E+09	8.11E+09	1.72E+10	2.47E+10	2.89E+10
12	6.63E+08	1.73E+09	4.62E+09	7.41E+09	1.21E+10	2.35E+10	3.23E+10	3.70E+10
13	1.31E+09	2.74E+09	6.92E+09	1.10E+10	1.75E+10	3.22E+10	4.33E+10	4.90E+10
14	2.23E+09	3.94E+09	9.38E+09	1.49E+10	2.36E+10	4.31E+10	5.76E+10	6.51E+10
15	3.22E+09	5.13E+09	1.16E+10	1.84E+10	2.96E+10	5.49E+10	7.42E+10	8.46E+10
16	4.01E+09	6.03E+09	1.32E+10	2.11E+10	3.45E+10	6.60E+10	9.10E+10	1.05E+11

17	4.54E+09	6.58E+09	1.41E+10	2.26E+10	3.76E+10	7.44E+10	1.05E+11	1.23E+11
18	4.99E+09	6.93E+09	1.42E+10	2.28E+10	3.83E+10	7.82E+10	1.13E+11	1.33E+11
19	5.60E+09	7.35E+09	1.40E+10	2.21E+10	3.70E+10	7.70E+10	1.13E+11	1.35E+11
20	6.54E+09	8.09E+09	1.41E+10	2.14E+10	3.52E+10	7.31E+10	1.08E+11	1.29E+11
21	8.00E+09	9.43E+09	1.50E+10	2.17E+10	3.44E+10	6.97E+10	1.02E+11	1.22E+11
22	1.01E+10	1.15E+10	1.69E+10	2.34E+10	3.56E+10	6.90E+10	9.98E+10	1.17E+11
23	1.31E+10	1.45E+10	2.01E+10	2.67E+10	3.90E+10	7.21E+10	1.02E+11	1.18E+11
24	1.68E+10	1.84E+10	2.43E+10	3.14E+10	4.44E+10	7.87E+10	1.09E+11	1.24E+11
25	2.12E+10	2.29E+10	2.94E+10	3.70E+10	5.12E+10	8.81E+10	1.20E+11	1.34E+11
26	2.60E+10	2.78E+10	3.49E+10	4.33E+10	5.87E+10	9.92E+10	1.34E+11	1.49E+11
27	3.09E+10	3.29E+10	4.05E+10	4.97E+10	6.66E+10	1.11E+11	1.49E+11	1.65E+11
28	3.61E+10	3.82E+10	4.63E+10	5.61E+10	7.43E+10	1.22E+11	1.63E+11	1.80E+11
29	4.16E+10	4.37E+10	5.21E+10	6.22E+10	8.12E+10	1.32E+11	1.75E+11	1.93E+11
30	4.74E+10	5.20E+10	5.79E+10	6.79E+10	8.72E+10	1.39E+11	1.83E+11	2.00E+11

Table A3. NECs for [82%Ar−18%CO_2]−Fe plasmas at R_p=1 mm (mole proportions, W. m^{-3}. sr^{-1})

T/kK	0.0%Fe	1%Fe	5%Fe	10%Fe	20%Fe	50%Fe	80%Fe	100%Fe
3	7.42E+04	8.87E+04	1.10E+05	1.23E+05	1.46E+05	2.14E+05	2.83E+05	3.27E+05
4	1.21E+04	5.18E+05	1.28E+06	1.98E+06	3.08E+06	5.55E+06	7.44E+06	8.34E+06
5	5.10E+04	4.77E+06	1.29E+07	2.04E+07	3.24E+07	6.37E+07	8.21E+07	9.54E+07
6	8.18E+05	2.36E+07	7.41E+07	1.25E+08	2.09E+08	4.05E+08	5.66E+08	6.62E+08
7	4.14E+06	6.15E+07	2.47E+08	4.52E+08	7.98E+08	1.60E+09	2.22E+09	2.58E+09
8	7.50E+06	1.05E+08	4.83E+08	9.73E+08	1.86E+09	3.96E+09	5.51E+09	6.34E+09
9	2.28E+07	2.04E+08	7.63E+08	1.53E+09	3.06E+09	6.91E+09	9.78E+09	1.13E+10
10	7.79E+07	4.26E+08	1.29E+09	2.31E+09	4.32E+09	9.67E+09	1.38E+10	1.60E+10
11	2.20E+08	8.34E+08	2.25E+09	3.70E+09	6.27E+09	1.27E+10	1.77E+10	2.03E+10
12	5.10E+08	1.47E+09	3.76E+09	5.90E+09	9.36E+09	1.73E+10	2.30E+10	2.59E+10
13	1.00E+09	2.32E+09	5.74E+09	8.87E+09	1.37E+10	2.38E+10	3.07E+10	3.41E+10
14	1.72E+09	3.34E+09	7.96E+09	1.23E+10	1.88E+10	3.22E+10	4.12E+10	4.54E+10
15	2.57E+09	4.40E+09	1.01E+10	1.56E+10	2.42E+10	4.18E+10	5.38E+10	5.97E+10
16	3.30E+09	5.27E+09	1.17E+10	1.84E+10	2.89E+10	5.15E+10	6.74E+10	7.57E+10
17	3.81E+09	5.82E+09	1.27E+10	2.01E+10	3.23E+10	5.96E+10	8.00E+10	9.10E+10
18	4.19E+09	6.10E+09	1.30E+10	2.06E+10	3.37E+10	6.46E+10	8.89E+10	1.03E+11

19	4.64E+09	6.37E+09	1.28E+10	2.01E+10	3.32E+10	6.57E+10	9.26E+10	1.08E+11
20	5.32E+09	6.86E+09	1.27E+10	1.95E+10	3.19E+10	6.40E+10	9.18E+10	1.08E+11
21	6.40E+09	7.82E+09	1.32E+10	1.95E+10	3.11E+10	6.18E+10	8.90E+10	1.05E+11
22	7.96E+09	9.36E+09	1.46E+10	2.07E+10	3.18E+10	6.12E+10	8.74E+10	1.02E+11
23	1.01E+10	1.16E+10	1.70E+10	2.31E+10	3.43E+10	6.32E+10	8.87E+10	1.03E+11
24	1.29E+10	1.44E+10	2.02E+10	2.67E+10	3.84E+10	6.81E+10	9.37E+10	1.07E+11
25	1.60E+10	1.77E+10	2.40E+10	3.11E+10	4.37E+10	7.54E+10	1.02E+11	1.15E+11
26	1.93E+10	2.12E+10	2.80E+10	3.59E+10	4.97E+10	8.43E+10	1.13E+11	1.26E+11
27	2.27E+10	2.47E+10	3.21E+10	4.07E+10	5.60E+10	9.40E+10	1.25E+11	1.39E+11
28	2.61E+10	2.83E+10	3.62E+10	4.55E+10	6.20E+10	1.04E+11	1.37E+11	1.52E+11
29	2.97E+10	3.19E+10	4.02E+10	4.99E+10	6.75E+10	1.12E+11	1.48E+11	1.63E+11
30	3.36E+10	3.78E+10	4.42E+10	5.40E+10	7.21E+10	1.18E+11	1.56E+11	1.71E+11

Table A4. NECs for [82%Ar−18%CO_2]−Fe plasmas at R_p=2.0 mm (mole proportions, W. m^{-3}. sr^{-1})

T/kK	0.0%Fe	1%Fe	5%Fe	10%Fe	20%Fe	50%Fe	80%Fe	100%Fe
3	7.38E+04	8.43E+04	9.83E+04	1.06E+05	1.20E+05	1.60E+05	2.03E+05	2.32E+05
4	1.19E+04	3.79E+05	9.60E+05	1.47E+06	2.26E+06	3.92E+06	5.14E+06	5.69E+06
5	4.27E+04	3.54E+06	9.71E+06	1.52E+07	2.37E+07	4.53E+07	5.71E+07	6.57E+07
6	6.70E+05	1.78E+07	5.66E+07	9.39E+07	1.53E+08	2.86E+08	3.87E+08	4.45E+08
7	3.69E+06	4.77E+07	1.92E+08	3.45E+08	5.89E+08	1.11E+09	1.46E+09	1.65E+09
8	6.48E+06	8.30E+07	3.78E+08	7.51E+08	1.39E+09	2.72E+09	3.55E+09	3.94E+09
9	1.82E+07	1.63E+08	5.97E+08	1.19E+09	2.30E+09	4.81E+09	6.38E+09	7.11E+09
10	6.09E+07	3.43E+08	1.01E+09	1.77E+09	3.25E+09	6.82E+09	9.25E+09	1.04E+10
11	1.70E+08	6.79E+08	1.77E+09	2.84E+09	4.66E+09	8.94E+09	1.20E+10	1.35E+10
12	3.91E+08	1.21E+09	2.98E+09	4.55E+09	6.95E+09	1.20E+10	1.53E+10	1.70E+10
13	7.58E+08	1.93E+09	4.61E+09	6.91E+09	1.02E+10	1.65E+10	2.03E+10	2.21E+10
14	1.28E+09	2.77E+09	6.49E+09	9.70E+09	1.43E+10	2.25E+10	2.73E+10	2.94E+10
15	1.95E+09	3.68E+09	8.40E+09	1.26E+10	1.87E+10	2.97E+10	3.62E+10	3.90E+10
16	2.62E+09	4.51E+09	1.01E+10	1.53E+10	2.30E+10	3.75E+10	4.64E+10	5.05E+10
17	3.14E+09	5.08E+09	1.12E+10	1.72E+10	2.64E+10	4.47E+10	5.68E+10	6.26E+10
18	3.50E+09	5.37E+09	1.16E+10	1.81E+10	2.84E+10	5.02E+10	6.56E+10	7.35E+10
19	3.86E+09	5.56E+09	1.15E+10	1.80E+10	2.87E+10	5.30E+10	7.13E+10	8.11E+10
20	4.36E+09	5.88E+09	1.14E+10	1.75E+10	2.81E+10	5.34E+10	7.36E+10	8.47E+10

21	5.18E+09	6.58E+09	1.17E+10	1.74E+10	2.75E+10	5.28E+10	7.37E+10	8.54E+10
22	6.35E+09	7.73E+09	1.26E+10	1.82E+10	2.80E+10	5.26E+10	7.35E+10	8.52E+10
23	7.96E+09	9.39E+09	1.44E+10	2.00E+10	2.98E+10	5.41E+10	7.47E+10	8.59E+10
24	9.95E+09	1.15E+10	1.69E+10	2.27E+10	3.29E+10	5.76E+10	7.82E+10	8.89E+10
25	1.22E+10	1.39E+10	1.97E+10	2.61E+10	3.69E+10	6.30E+10	8.41E+10	9.46E+10
26	1.45E+10	1.64E+10	2.28E+10	2.98E+10	4.16E+10	6.97E+10	9.21E+10	1.03E+11
27	1.68E+10	1.88E+10	2.58E+10	3.35E+10	4.65E+10	7.72E+10	1.01E+11	1.12E+11
28	1.91E+10	2.12E+10	2.88E+10	3.71E+10	5.13E+10	8.48E+10	1.11E+11	1.22E+11
29	2.15E+10	2.36E+10	3.16E+10	4.04E+10	5.56E+10	9.18E+10	1.20E+11	1.32E+11
30	2.40E+10	2.77E+10	3.42E+10	4.33E+10	5.91E+10	9.74E+10	1.27E+11	1.39E+11

Table A5. NECs for [82%Ar−18%CO_2]−Fe plasmas at R_p=5.0 mm (mole proportions, W. m^{-3}. sr^{-1})

T/kK	0.0%Fe	1%Fe	5%Fe	10%Fe	20%Fe	50%Fe	80%Fe	100%Fe
3	7.26E+04	7.91E+04	8.71E+04	8.99E+04	9.53E+04	1.09E+05	1.29E+05	1.45E+05
4	1.17E+04	2.59E+05	6.52E+05	9.80E+05	1.46E+06	2.42E+06	3.09E+06	3.38E+06
5	3.28E+04	2.44E+06	6.56E+06	1.00E+07	1.52E+07	2.79E+07	3.42E+07	3.88E+07
6	4.73E+05	1.24E+07	3.85E+07	6.22E+07	9.81E+07	1.71E+08	2.20E+08	2.45E+08
7	2.91E+06	3.39E+07	1.33E+08	2.30E+08	3.72E+08	6.27E+08	7.66E+08	8.29E+08
8	5.39E+06	6.00E+07	2.67E+08	5.10E+08	8.81E+08	1.49E+09	1.77E+09	1.87E+09
9	1.34E+07	1.19E+08	4.21E+08	8.12E+08	1.48E+09	2.67E+09	3.21E+09	3.39E+09
10	4.34E+07	2.51E+08	7.02E+08	1.20E+09	2.09E+09	3.91E+09	4.89E+09	5.29E+09
11	1.21E+08	5.03E+08	1.24E+09	1.89E+09	2.95E+09	5.14E+09	6.54E+09	7.20E+09
12	2.79E+08	9.11E+08	2.09E+09	3.03E+09	4.33E+09	6.75E+09	8.34E+09	9.15E+09
13	5.35E+08	1.47E+09	3.28E+09	4.64E+09	6.36E+09	9.15E+09	1.08E+10	1.17E+10
14	8.74E+08	2.11E+09	4.68E+09	6.60E+09	8.97E+09	1.25E+10	1.44E+10	1.53E+10
15	1.29E+09	2.78E+09	6.16E+09	8.77E+09	1.20E+10	1.69E+10	1.93E+10	2.03E+10
16	1.79E+09	3.48E+09	7.63E+09	1.10E+10	1.53E+10	2.20E+10	2.54E+10	2.67E+10
17	2.29E+09	4.07E+09	8.84E+09	1.29E+10	1.84E+10	2.74E+10	3.23E+10	3.43E+10
18	2.68E+09	4.43E+09	9.52E+09	1.41E+10	2.07E+10	3.24E+10	3.92E+10	4.23E+10
19	3.01E+09	4.63E+09	9.68E+09	1.46E+10	2.19E+10	3.62E+10	4.52E+10	4.95E+10
20	3.39E+09	4.86E+09	9.65E+09	1.45E+10	2.23E+10	3.85E+10	4.96E+10	5.51E+10
21	3.97E+09	5.33E+09	9.82E+09	1.46E+10	2.24E+10	3.96E+10	5.22E+10	5.86E+10
22	4.78E+09	6.10E+09	1.05E+10	1.51E+10	2.28E+10	4.05E+10	5.39E+10	6.09E+10

23	5.88E+09	7.25E+09	1.17E+10	1.63E+10	2.39E+10	4.18E+10	5.56E+10	6.27E+10
24	7.21E+09	8.68E+09	1.33E+10	1.81E+10	2.60E+10	4.41E+10	5.81E+10	6.51E+10
25	8.67E+09	1.03E+10	1.53E+10	2.04E+10	2.87E+10	4.74E+10	6.18E+10	6.86E+10
26	1.02E+10	1.19E+10	1.75E+10	2.30E+10	3.19E+10	5.17E+10	6.66E+10	7.34E+10
27	1.16E+10	1.35E+10	1.96E+10	2.57E+10	3.54E+10	5.66E+10	7.25E+10	7.93E+10
28	1.30E+10	1.50E+10	2.16E+10	2.83E+10	3.89E+10	6.19E+10	7.89E+10	8.59E+10
29	1.44E+10	1.65E+10	2.35E+10	3.07E+10	4.21E+10	6.69E+10	8.52E+10	9.24E+10
30	1.58E+10	1.92E+10	2.52E+10	3.27E+10	4.48E+10	7.12E+10	9.07E+10	9.81E+10

Appendix III Nestor-Olsen Abel-inversion algorithm

The reconstruction of the radial density distribution of a cylindrically symmetric object is a common task in different area of physics (e.g. plasma physics). Typically, optical measurements of objects like plasma columns or flames are integrated along the line of sight. To obtain the underlying distribution from a measured projection, the inverse Abel transform has to be calculated. The Schematic diagram of Abel inversion is given in figure B.

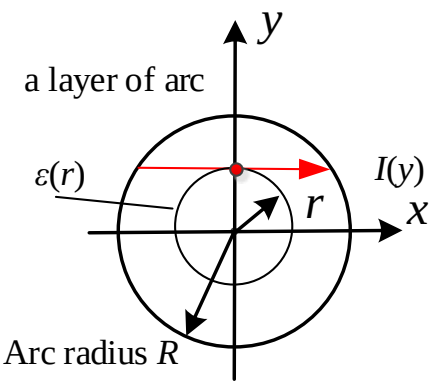

Figure B Schematic diagram of Abel inversion

For a cylindrically symmetric and optical thin arc, the emission coefficient $\varepsilon(r)$ and its integrated radiation density $I(y)$ conforms to the relation of Abel transform[133, 134]:

$$I(y)=2\int_0^R \varepsilon(r)\mathrm{d}x \tag{1}$$

Assuming $\varepsilon(\Delta\lambda, r)$ drops to zero more quickly than $1/r$, the inverse Abel transform is given by[133, 134]

$$\varepsilon(r)=-\frac{1}{\pi}\cdot\int_r^R \frac{\mathrm{d}I(y)}{\mathrm{d}y}\cdot\frac{\mathrm{d}y}{\sqrt{y^2-r^2}} \tag{2}$$

For Nestor-Olsen method, the arc is considered as consisting of multiple equidistant annuluses. When the number of annuluses is large enough, the calculation is precise. In the present study, the Nestor-Olsen method was used due to its easy computation and widespread use[133, 135].

According to the Nestor-Olsen method, emission coefficient $\varepsilon(r)$ can be expressed as[133, 134]

$$\varepsilon(r_j)=-\frac{2}{\pi\Delta y}\sum_{i=j}^{N-1} I(y_i)\, B_{j,i} \tag{4}$$

where

$$B_{j,i}=\begin{cases} A_{j,i-1}-A_{j,i} & \text{for } i\geq j \\ -A_{j,i} & \text{for } i=j \end{cases} \tag{5}$$

with

$$A_{j,i}=\frac{\sqrt{i^2-(j-1)^2}-\sqrt{(i-1)^2-(j-1)^2}}{2i-1} \tag{6}$$

In Eq. (4), $y_i=i\Delta y$ and $r_i=i\Delta r$, with $i=-N, \ldots,0, \ldots N$. Δy is the distance of two adjacent test positions for $I(y)$, and Δr is the distance of two adjacent equidistant annuluses. Δy is equal to Δr. At the axis of the arc, $y_0=r_0=0$. At the margin of the arc, $y_N=r_N=R$.

References

[1] Lancaster J F. The physics of welding, Oxford: Pergamon, 1984

[2] Lesnewich A. Control of melting rate and metal transfer in gas-shielded metal-arc welding part I -control of electrode melting rate, Welding Journal, 1958, 37: 343s-53s

[3] Lesnewich A. Control of melting rate and metal transfer in gas-shielded metal-arc welding part II - control of metal transfer, Welding Journal, 1958, 37: 418s-24s

[4] Geary D, Miller R. Welding, New York: McGraw-Hill Education, 2011

[5] Weman K. Welding processes handbook, UK: Woodhead Publishing, 2011

[6] Ton H. Physical properties of the plasma–MIG welding arc, Journal of Physics D: Applied Physics, 1975, 8(8): 922-33

[7] Smars E A, Acinger K. Material transport and temperature distribution in arc between melting aluminium electrodes, International Institude of Welding, 1968, Document 212: 162-68

[8] Smars E A, Acinger K, Sipek L. Temperature in argon shielded welding arc with iron electrodes, International Institude of Welding, 1970, Document 212: 162-68

[9] Murphy A B. The effects of metal vapour in arc welding, Journal of Physics D: Applied Physics, 2010, 43: 434001

[10] Cressault Y, Gleizes A. Thermal plasma properties for Ar–Al, Ar–Fe and Ar–Cu mixtures used in welding plasmas processes: I. Net emission coefficients at atmospheric pressure, Journal of Physics D: Applied Physics, 2013, 46: 415206

[11] Cressault Y. Basic knowledge on radiative and transport properties to begin in thermal plasmas modelling, AIP Advances, 2015, 5: 057112

[12] Cressault Y, Murphy A B, Teulet P, et al. Thermal plasma properties for Ar–Cu, Ar–Fe and Ar–Al mixtures used in welding plasmas processes: II. Transport coefficients at atmospheric pressure, Journal of Physics D: Applied Physics, 2013, 46: 415207

[13] Murphy A B. Influence of metal vapour on arc temperatures in gas–metal arc welding: convection versus radiation, Journal of Physics D: Applied Physics, 2013, 46: 224004

[14] Murphy A B, Farmer A J D, Haidar J. Laser-scattering measurement of temperature profiles of a free-burning arc, Applied Physics Letters, 1992, 60(11): 1304-06

[15] Dzierzega K, Zawadzki W, Pokrzywka B, et al. Experimental investigations of plasma perturbation in Thomson scattering applied to thermal plasma diagnostics, Physical Review E, 2006, 74(2 Pt 2): 026404

[16] Snyder S C, Reynolds L D, Fincke J R, et al. Electron-temperature and electron-density profiles in an atmospheric-pressure argon plasma jet, Physical Review E, 1994, 50(1): 519-25

[17] Meiering E M, Serrano L, Fersht A R. Analysis of the enthalpy probe technique for thermal plasma diagnostics, Review of Scientific Instruments, 1995, 66(6): 3424-31

[18] Swank W D, Fincke J R, Haggard D C. Modular enthalpy probe and gas analyzer for thermal plasma measurements, Review of Scientific Instruments, 1993, 64(1): 56-62

[19] Akbar S, Etemadi K. Impact of copper vapor contamination on argon arcs, Plasma Chemistry and Plasma Processing, 1997, 17(2): 251-62

[20] Etemadi K, Pfender E. Impact of anode evaporation on the anode region of a high-intensity argon arc, Plasma Chemistry and Plasma Processing, 1985, 5(2): 175-82

[21] Gonzalez J J, Bouaziz M, Razafinimanana M, et al. The influence of iron vapour on an argon transferred arc, Plasma Sources Science and Technology, 1997, 6(1): 20-28

[22] Razafinimanana M, Hamidi L E, Gleizes A, et al. Experimental study of the influence of anode ablation on the characteristics of an argon transferred arc, Plasma Sources Science and Technology, 1998, 4(3): 501-10

[23] Rouffet M, Wendt M, Goett G, et al. Spectroscopic investigation of the high-current phase of a pulsed GMAW process, Journal of Physics D: Applied Physics, 2010, 43: 434003

[24] Valensi F, Pellerin S, Boutaghane A, et al. Plasma diagnostics in gas metal arc

welding by optical emission spectroscopy, Journal of Physics D: Applied Physics, 2010, 43(43): 434002

[25] Valensi F, Pellerin S, Castillon Q, et al. Study of the spray to globular transition in gas metal arc welding: a spectroscopic investigation, Journal of Physics D: Applied Physics, 2013, 46: 224005

[26] Wilhelm G, Gött G, Schöpp H, et al. Study of the welding gas influence on a controlled short-arc GMAW process by optical emission spectroscopy, Journal of Physics D: Applied Physics, 2010, 43: 434004

[27] Wilhelm G, Kozakov R, Gött G, et al. Behaviour of the iron vapour core in the arc of a controlled short-arc GMAW process with different shielding gases, Journal of Physics D: Applied Physics, 2012, 45(8): 085202

[28] Zielińska S, Musioł K, Dzierżęga K, et al. Investigations of GMAW plasma by optical emission spectroscopy, Plasma Sources Science and Technology, 2007, 16(4): 832-38

[29] Goecke S F. Auswirkungen von Aktivgaszumischungen im vpm-Bereich zu Argon auf das MIG-Impulsschweißen von Aluminium, PhD Thesis, Technical University Berlin, 2004

[30] Goecke S F, Metzke E, Spille-Kohoff A, et al. ChopArc. MSG-Lichtbogenschweißen für den Ultraleichtbau, Stuttgart: Fraunhofer IRB Verlag, 2005

[31] Uhrlandt D. Diagnostics of metal inert gas and metal active gas welding processes, Journal of Physics D: Applied Physics, 2016, 49: 313001

[32] Ogawa Y. High speed imaging technique Part 1–high speed imaging of arc welding phenomena, Science and Technology of Welding and Joining, 2013, 16(1): 33-43

[33] Bachmann B, Kozakov R, Gött G, et al. High-speed three-dimensional plasma temperature determination of axially symmetric free-burning arcs, Journal of Physics D: Applied Physics, 2013, 46: 125203

[34] Rouffet M E, Cressault Y, Gleizes A, et al. Thermal plasma diagnostic methods based on the analysis of large spectral regions of plasma radiation, Journal of Physics D: Applied Physics, 2008, 41: 125204

[35] Rouffet M E. Nouvelle méthode de diagnostic optique des plasmas thermiques: application au mélange argon-hydrogène-hélium, PhD Thesis, Université de

Toulouse, 2008

[36] Hlína J, Šonský J, Gruber J, et al. Fast tomographic measurements of temperature in an air plasma cutting torch, Journal of Physics D: Applied Physics, 2016, 49: 105202

[37] Menart J, Heberlein J, Pfender E. Line-by-line method of calculating emission coefficients for thermal plasmas consisting of monatomic species, Journal of Quantitative Spectroscopy and Radiative Transfer, 1996, 56(3): 377-98

[38] Billoux T, Cressault Y, Gleizes A. Tables of radiative transition probabilities for the main diatomic molecular systems of OH, CH, CH+, CO and CO+ occurring in CO–H2 syngas-type plasma, Journal of Quantitative Spectroscopy and Radiative Transfer, 2014, 133: 434-44

[39] Mościcki T, Hoffman J, Szymański Z. Emission coefficients of low temperature thermal iron plasma, Czechoslovak Journal of Physics, 2004, 54(3): C677-C82

[40] Billoux T, Cressault Y, Boretskij V, et al. Net emission coefficient of CO2-Cu thermal plasmas: role of copper and molecules, Journal of Physics: Conference Series, 2012, 406: 012027

[41] Essoltani A, Proulx P, Boulos M I, et al. Effect of the presence of iron vapors on the volumetric emission of Ar/Fe and Ar/Fe/H2 plasmas, Plasma Chemistry and Plasma Processing, 1994, 14(3): 301-15

[42] Zhong L L, Wang X H, Rong M Z, et al. Effects of copper vapour on thermophysical properties of CO2-N2 plasma, European Physical Journal Applied Physics, 2016, 70(11): 233

[43] Non-binding guide to good practice for implementing Directive 2006/25/EC 'Artificial Optical Radiation', Directorate-General for Employment, Social Affairs and Inclusion Unit B.3, European Commission. 2016, Doi:10.2767/74218

[44] Baxter P J, Aw T-C, Cockcroft A, et al. Hunter's diseases of occupations 10th edition, London: Hodder Arnold, 2011: 421-433

[45] Heltoft K N, Slagor R M, Agner T, et al. Metal arc welding and the risk of skin cancer, International Archives of Occupational & Environmental Health, 2017, 90(8): 873-81

[46] Tenkate T D. Ocular ultraviolet radiation exposure of welders, Scandinavian

Journal of Work Environment and Health, 2017, 43(3): 287-88

[47] Tenkate T D, Collins M J. Angles of entry of ultraviolet radiation into welding helmets, American Industrial Hygiene Association Journal, 1997, 58(1): 54-56

[48] Tenkate T D, Collins M J. Personal ultraviolet radiation exposure of workers in a welding environment, American Industrial Hygiene Association Journal, 1997, 58(1): 33-38

[49] Nakashima H, Utsunomiya A, Takahashi J, et al. Hazard of ultraviolet radiation emitted in gas metal arc welding of mild steel, Journal of Occupational Health, 2016, 58(5): 452-59

[50] Nakashima H, Takahashi J, Fujii N, et al. Blue-light hazard from gas metal arc welding of aluminum alloys, Annals of Work Exposures and Health 2017, 61(8): 965-74

[51] Okuno T. Measurement of ultraviolet radiation from welding arcs, Industrial Health, 1987, 25(3): 147-56

[52] Devore R K. The effective spectral irradiance of ultra-violet radiations from inert-gas-shielded welding processes in relation to the arc current density, Master Thesis, Texas A&M University, 1973

[53] Nakashima H, Utsunomiya A, Fujii N, et al. Hazard of ultraviolet radiation emitted in gas tungsten arc welding of aluminum alloys, Industrial Health, 2016, 54(2): 149-56

[54] Gourzoulidis G A, Achtipis A, Topalis F V, et al. Artificial optical radiation photobiological hazards in arc welding, Physica Medica, 2016, 32(8): 981-86

[55] Okuno T, Ojima J, Saito H. Blue-light hazard from CO2 arc welding of mild steel, Annals of Occupational Hygiene, 2010, 54(3): 293-98

[56] Directive 2006/25/EC. On the minimum health and safety requirements regarding the exposure of workers to risks arising from physical agents (artificial optical radiation), Official Journal of the European Union, 2006

[57] Documentation of the threshold limit values and biological exposure indices, American conference of governmental industrial hygienists, Cincinnati, 1991

[58] Xiong J, Zhang G, Zhang W. Forming appearance analysis in multi-layer single-pass GMAW-based additive manufacturing, International Journal of Advanced Manufacturing Technology, 2015, 80(9-12): 1767-76

[59] Griem H R. Plasma spectroscopy, New York: McGraw-Hill, 1964

[60] Griem H R. Principles of plasma spectroscopy, Cambridge: Cambridge University Press, 1997

[61] Boulos M I, Fauchais P, Pfender E. Thermal plasmas: Fundamentals and applications volume 1, New York: Plenum Press, 1994

[62] Drawin H W, Emard F. Optical escape factors for bound-bound and free-bound radiation from plasmas. I. constant source function, Beit Plasmaphys, 1973, 13(3): 143-68

[63] Naghizadeh-Kashani Y, Cressault Y, Gleizes A. Net emission coefficient of air thermal plasmas, Journal of Physics D: Applied Physics, 2002, 35: 2925-34

[64] Godin D, Trépanier J Y. A robust and efficient method for the computation of equilibrium composition in gaseous mixtures, Plasma Chemistry and Plasma Processing, 2004, 24(3): 447-73

[65] Sauer T. Numerical analysis, Beijing: China Machine Press, 2012

[66] Kramida A E, Ralchenko Y, Reader J, et al. NIST Atomic Spectra Database,

[67] Drawin H W, Felenbok P. Data for plasmas in local thermodynamic equilibrium, Paris: Gauthier-Villars, 1965

[68] Herzberg G, Mrozowski S. Molecular Spectra and Molecular Structure. I. Spectra of Diatomic Molecules, New York: Van-Nostrand Reinhold, 1955

[69] Drellishak K S, Aeschliman D P, Cambel A B. Partition functions and thermodynamic properties of nitrogen and oxygen, Physics of Fluids, 1965, 8(9): 1590-600

[70] Herzberg G. Molecular Spectra and Molecular Structure II. Infrared and Raman Spectra, New York: Van-Nostrand Reinhold, 1945

[71] Huber K P, Herzberg G. Molecular spectra and molecular structure: IV. constants of diatomic molecules, New York: Van-Nostrand Reinhold, 1978

[72] Chase M W J, Davies C A, Downey J R J, et al. JANAF thermochemical tables, J Phys Chem Ref Data, 1985, 14: 3rd edn (Suppl. 1)

[73] Lowke J. Predictions of arc temperature profiles using approximate emission coefficients for radiation losses, J Quant Spectrosc Radiat Transfer, 1974, 14(2): 111-22

[74] Aubrecht V, Lowke J J. Calculations of radiation transfer in SF6 plasmas using the method of partial characteristics, J Phys D: Appl Phys, 1994, 27: 2066-73

[75] Menart J. Radiative transport in a two-dimensional axisymmetric thermal

plasma using the S–N discrete ordinates method on a line-by-line basis, J Quant Spectrosc Radiat Transfer, 2000, 67(67): 273-91

[76] Nordborg H, Iordanidis A A. Self-consistent radiation based modelling of electric arcs: I. Efficient radiation approximations, Journal of Physics D: Applied Physics, 2008, 41: 135205

[77] Larsen E W, Thömmes G, Klar A, et al. Simplified PN approximations to the equations of radiative heat transfer and applications, Journal of Computational Physics, 2002, 183(2): 652-75

[78] Soucasse L, Rivière P, Soufiani A, et al. Transitional regimes of natural convection in a differentially heated cubical cavity under the effects of wall and molecular gas radiation, Physics of Fluids, 2014, 26(24105): 1-23

[79] Siegel R, Howell J R. Thermal radiation heat transfer, London: Hemisphere Publishing, 1992

[80] Modest M F. Radiative heat transfer, New York: The Pennsylvania State University, 2003

[81] Boulos M I, Fauchais P, Pfender E. Thermal Plasmas: Fundamentals and Applications vol 1, New York: Plenum Press, 1994: 468

[82] Gleizes A, Gonzalez J J, Razafinimanana M, et al. Influence of radiation on temperature field calculation in SF6 arcs, Plasma Sources Sci Technol, 1992, 1: 135-40

[83] Lowke J J, Liebermann R W. Predicted arc properties in sulfur hexafluoride, Journal of Applied Physics, 1971, 42(9): 3532-39

[84] Murphy A B. The effects of metal vapour in arc welding, J Phys D: Appl Phys, 2010, 43(43): 434001

[85] Moore C E. Atomic Energy Levels, Vols I-III, Washington D C: U.S Government Printing Office, 1949-1958

[86] Kurucz R L, Peytremann E. Atomic line data,

[87] Aubrecht V, Bartlova M. Net emission coefficients of radiation in air and SF6 thermal plasmas, Plasma Chemistry and Plasma Processing, 2009, 29(2): 131-47

[88] Laux C O. Optical diagnostics and radiative emission of air plasmas, PhD Thesis Thesis, Stanford University, 1993

[89] Traving G. Interpretation of Line Broadening and Line Shift. In:

Lochte-Holtgreven W, editor. Plasma Diagnostics. Amsterdam: North-Holland, 1968. p. 66-134

[90] Griem H R. Semiempirical formulas for the electron-impact widths and shifts of isolated ion lines in plasmas, Physical Review, 1968, 165(1): 258-66

[91] Whiting E E. An empirical approximation to the Voigt profile, J Quant Spectrosc Radiat Transfer, 1968, 8(6): 1379-84

[92] Cressault Y, Gleizes A. Thermal plasma properties for Ar–Al, Ar–Fe and Ar–Cu mixtures used in welding plasmas processes: I. Net emission coefficients at atmospheric pressure, J Phys D: Appl Phys, 2013, 46(41): 415206

[93] D'Yachkov L G, Golubev O A. Studies of continuum radiation from nitrogen, oxygen and carbon dioxide plasmas in the vacuum ultraviolet region, J Quant Spectrosc Radiat Transfer, 1978, 20(20): 175–89

[94] Robinson E J, Geltman S. Single- and double-quantum photodetachment of negative ions, Physical Review, 1967, 153(1): 4-8

[95] Stewart J C, Rotenberg M. Wave functions and transition probabilities in scaled Thomas-Fermi ion potentials, Physical Review, 1967, 156(5A): A1508-A19

[96] Hofsaess D. Emission continua of rare gas plasmas, J Quant Spectrosc Radiat Transfer, 1978, 19(3): 339-52

[97] Gleizes A, Gongassian M, Rahmani B. Continuum absorption coefficient in SF6 and SF6-N2 mixture plasmas, J Phys D: Appl Phys, 2000, 22(1): 83-89

[98] Hofsaess D. Photoionization cross sections calculated by the scaled Thomas-Fermi method ($h\nu \leq 50$ eV), At Data Nucl Data Tables, 1979, 24(24): 285-321

[99] Okuda S, Ueda Y, Murai Y, et al. Spectroscopic approach to the analysis of high current arcs in SF6, IEEE Transactions on Plasma Science, 1980, 8(4): 395-99

[100] Cabannes F, Chapelle J. Spectroscopic Plasma Diagnostics. In: Venugopalan M, editor. Reactions Under Plasma Conditions vol 2. Vol. 2. New York: John Wiley & Sons, 1971. p. 367

[101] Grant I P. Calculation of Gaunt factors for free-free transitions near positive ions, Monthly Notices of the Royal Astronomical Society, 1958, 118(3): 241-57

[102] Neynaber R H, Marino L L, Rothe E W, et al. Scattering of low-energy electrons by atomic hydrogen, Physical Review, 1961, 124(1): 135-36

[103] Tanaka M, Lowke J. Predictions of weld pool profiles using plasma physics, Journal of Physics D: Applied Physics, 2006, 40(1): R1-R23

[104] Jan C, Cressault Y, Gleizes A, et al. Calculation of radiative properties of SF6-C2F4 thermal plasmas-application to radiative transfer in high-voltage circuit breakers modelling, J Phys D: Appl Phys, 2014, 47(1): 15204

[105] Pouilly B, Robbe J M, Schamps J, et al. Photodissociation and radiative processes in interstellar C2, J Phys B: At Mol Phys, 1999, 16(3): 437-48

[106] Padial N T, Collins L A, Schneider B I. Photoionization of ground-state molecular carbon C2, Astrophysical Journal, 1985, 298(1): 369-74

[107] Fennelly J A, Torr D G. Photoionization and photoabsorption cross sections of O, N2, O2, and N for aeronomic calculations, At Data Nucl Data Tables, 1992, 51(2): 321-63

[108] Cole B E, Dexter R N. Photoabsorption and photoionisation measurements on some atmospheric gases in the wavelength region 50-340 A, J Phys B: At Mol Opt Phys, 1978, 11(6): 1011-23

[109] Reilhac L D, Damany N. Photoabsorption cross-section measurements of some gases, from 10 to 50 nm, J Quant Spectrosc Radiat Transfer, 1977, 18(1): 121-31

[110] Cook G R, Metzger P H, Ogawa M. Photoionization and absorption coefficients of CO in the 600 to 1000 Å, Canadian Journal of Physics, 1965, 43(43): 1706-22

[111] Lee L C, Carlson R W, Judge D L, et al. The absorption cross sections of N2, O2, CO, NO, CO2, N2O, CH4, C2H4, C2H6 and C4H10 from 180 to 700 Å, J Quant Spectrosc Radiat Transfer, 1973, 13(10): 1023-31

[112] Hudson R D. Absorption Cross Sections of Stratospheric Molecules, Can J Chem, 1974, 52(8): 1-9

[113] Moortgat G K, Warneck P. Relative O/1D/ quantum yields in the near UV photolysis of ozone at 298 K, Zeitschrift Fur Naturforschung A, 1975, 30(6-7): 835-44

[114] Fiocco G. Mesospheric models and related experiments, Berlin: Springer, 1971

[115] Griggs M. Absorption coefficients of ozone in the ultraviolet and visible regions, Journal of Chemical Physics, 1968, 49(2): 857-59

[116] Tanaka Y, Inn E C Y, Watanabe K. Absorption coefficients of gases in the vacuum ultraviolet. Part IV. Ozone, Journal of Chemical Physics, 1953, 21: 1651-53

[117] Cressault Y. Basic knowledge on radiative and transport properties to begin in thermal plasmas modelling, AIP Adv, 2015, 5(5): 057112

[118] Billoux T, Cressault Y, Boretskij V, et al. Net emission coefficient of CO2-Cu thermal plasmas: role of copper and molecules, Journal of Physics: Conference Series, 2012, 406(1): 012027

[119] Babou Y, Rivière P, Perrin M Y, et al. Spectroscopic data for the prediction of radiative transfer in CO 2 –N 2 plasmas, J Quant Spectrosc Radiat Transfer, 2009, 110(1–2): 89-108

[120] Chauveau S. Constitution de bases de données spectroscopiques relatives à un plasma d'air: Application au calcul du transfert radiatif, PhD Thesis Thesis, Ecole Centrale Paris, 2001

[121] Lino d S, M, Dudeck M. Arrays of radiative transition probabilities for CO2–N2 plasmas, J Quant Spectrosc Radiat Transfer, 2006, 102(3): 348-86

[122] Whiting E E, Schadee A, Tatum J B, et al. Recommended conventions for defining transition moments and intensity factors in diatomic molecular spectra, Journal of Molecular Spectroscopy, 1980, 80(2): 249-56

[123] Jr B R. Spectral line broadening in air molecule systems, Applied Optics, 1967, 6(1): 141-47]

[124] Sick V, Decker M, Heinze J, et al. Collisional processes in the O2 B 3Sigma-u state, Chemical Physics Letters, 1996, 249(1996): 335-40

[125] Lewis B R, Berzins L, Dedman C J, et al. Pressure-broadening in the Schumann-Runge bands of molecular oxygen, J Quant Spectrosc Radiat Transfer, 1988, 39(4): 271-82

[126] LS R, IE G, A B, et al. The HITRAN 2008 molecular spectroscopic database, J Quant Spectrosc Radiat Transfer, 2009, 110: 533-72

[127] Sung K, Varanasi P. Intensities, collision-broadened half-widths, and collision-induced line shifts in the second overtone band of ja:math, J Quant Spectrosc Radiat Transfer, 2004, 83(3–4): 445-58

[128] Tashkun S A, Perevalov V I. CDSD-4000: High-resolution, high-temperature carbon dioxide spectroscopic databank, J Quant Spectrosc Radiat Transfer, 2011, 112(9): 1403-10

[129] Rothman L S, Gordon I E, Babikov Y, et al. The HITRAN2012 molecular spectroscopic database, J Quant Spectrosc Radiat Transfer, 2013, 130(11): 4-50

[130] Randrianandraina H Z, Cressault Y, Gleizes A. Improvements of radiative transfer calculation for SF6 thermal plasmas, J Phys D: Appl Phys, 2011, 44(19): 252-60

[131] Drayson S R. Rapid computation of the Voigt profile, J Quant Spectrosc Radiat Transfer, 1976, 16(7): 611-14

[132] Wiese W L. Spectroscopic diagnostics of low temperature plasmas: techniques and required data, Spectrochimica Acta Part B: Atomic Spectroscopy, 1991, 46(6–7): 831-41

[133] Álvarez R, Rodero A, Quintero M C. An Abel inversion method for radially resolved measurements in the axial injection torch, Spectrochimica Acta Part B: Atomic Spectroscopy, 2002, 57(11): 1665-80

[134] Chan G C Y, Hieftje G M. Estimation of confidence intervals for radial emissivity and optimization of data treatment techniques in Abel inversion, Spectrochimica Acta Part B: Atomic Spectroscopy, 2006, 61(1): 31-41

[135] Engel U, Prokisch C, Voges E, et al. Spatially resolved measurements and plasma tomography with respect to the rotational temperatures for a microwave plasma torch, Journal of Analytical Atomic Spectrometry, 1998, 13(9): 955-61

[136] Neger T. Optical tomography of plasmas by spectral interferometry, Journal of Physics D Applied Physics, 1999, 28(1): 47

[137] Bachmann B, Kozakov R, Gött G, et al. High-speed three-dimensional plasma temperature determination of axially symmetric free-burning arcs, J Phys D: Appl Phys, 2013, 46(12): 125203

[138] Ogawa Y. High speed imaging technique Part 1–high speed imaging of arc welding phenomena, Sci Technol Weld Join, 2013, 16(1): 33-43

[139] Rouffet M E, Cressault Y, Gleizes A, et al. Thermal plasma diagnostic methods based on the analysis of large spectral regions of plasma radiation, J Phys D:

Appl Phys, 2008, 41(12): 125204

[140] Hlína J, Šonský J, Gruber J, et al. Fast tomographic measurements of temperature in an air plasma cutting torch, J Phys D: Appl Phys, 2016, 49(10): 105202

[141] Haidar J. The dynamic effects of metal vapour in gas metal arc welding, J Phys D: Appl Phys, 2010, 43(16): 165204

[142] Murphy A B. A self-consistent three-dimensional model of the arc, electrode and weld pool in gas–metal arc welding, J Phys D: Appl Phys, 2011, 44(19): 194009

[143] Schnick M, Fuessel U, Hertel M, et al. Modelling of gas–metal arc welding taking into account metal vapour, J Phys D: Appl Phys, 2010, 43(43): 434008

[144] Rouffet M E. Nouvelle méthod de diagnostic optique des plasmas thermiques: application au mélange argon-hydrogène-hélium, PhD Thesis, Université Toulouse III-Paul Sabatier, 2008

[145] Menart J, Malik S. Net emission coefficients for argon-iron thermal plasmas, J Phys D: Appl Phys, 2002, 35(9): 867

[146] Essoltani A, Proulx P, Boulos M I, et al. Effect of the presence of iron vapors on the volumetric emission of Ar/Fe and Ar/Fe/H2 plasmas, Plasma Chem Plasma Process, 1994, 14(3): 301-15

[147] Lowke J J. Predictions of arc temperature profiles using approximate emission coefficients for radiation losses, Journal of Quantitative Spectroscopy and Radiative Transfer, 1974, 14(2): 111-22

[148] Rao Z, Hu J, Liao S, et al. Modeling of the transport phenomena in GMAW using argon–helium mixtures. Part I–The arc, International Journal of Heat and Mass Transfer, 2010, 53(25): 5707-21

[149] Uhrlandt D. Diagnostics of metal inert gas and metal active gas welding processes, J Phys D: Appl Phys, 2016, 49(31): 313001

[150] Drawin H. Spectroscopic measurement of high temperatures (a review), High Temp High Press, 1970, 2: 359–409

[151] Álvarez R, Rodero A, Quintero M C. An Abel inversion method for radially resolved measurements in the axial injection torch, Spectrochim Acta B, 2002, 57(11): 1665-80

[152] Blades M W, Horlick G. Photodiode array measurement system for

implementing Abel inversions on emission from an inductively coupled plasma, Applied Spectroscopy, 1980, 34(6): 696-99

[153] Gu X, Li H, Yang L, et al. Coupling mechanism of laser and arcs of laser-twin-arc hybrid welding and its effect on welding process, Opt Laser Technol, 2013, 48(6): 246-53

[154] Rouffet M, Wendt M, Goett G, et al. Spectroscopic investigation of the high-current phase of a pulsed GMAW process, J Phys D: Appl Phys, 2010, 43(43): 434003

[155] Murphy A B. Influence of metal vapour on arc temperatures in gas–metal arc welding: convection versus radiation, J Phys D: Appl Phys, 2013, 46(22): 224004

[156] Schnick M, Hertel M, Fuessel U, et al. Energy balance in MIG arcs, J Phys D: Appl Phys, 2013, 46(46): 224002

[157] Pellerin S, Musiol K, Pokrzywka B, et al. Stark width of 4p'[1/2]-4s[3/2]° Ar I transition (696.543 nm), JPhysB:AtMolOptPhys, 1996, 29(17): 3911

[158] Lesage A, Lebrun J L, Richou J. Temperature dependence of Stark parameters for Fe I lines, Astrophys J, 1990, 360(360): 737-40

[159] Cram L E, Poladian L, Roumeliotis G. Departures from equilibrium in a free-burning argon arc, Journal of Physics D: Applied Physics, 1988, 21(3): 418-25

[160] Rat V, Murphy A B, Aubreton J, et al. Treatment of non-equilibrium phenomena in thermal plasma flows, Journal of Physics D: Applied Physics, 2008, 41(18): 183001

[161] Tenkate T D. Optical radiation hazards of welding arcs, Reviews on Environmental Health, 1998, 13(3): 131-45

[162] Directive 2006/25/EC. On the minimum health and safety requirements regarding the exposure of workers to risks arising from physical agents (artificial optical radiation)//. Official Journal of the European Union. 2006.

[163] Ryer A. The light measurement handbook, USA: International Light Inc., 1997

[164] Bass M, Stryland E W V, Williams D R, et al. Handbook of Optics Volume II Devices, Measurements, and Properties 2nd edition, 1995

[165] Patankar S V. Numerical heat transfer and fluid flow: Computational methods in mechanics and thermal science, Washington: McGraw-Hill, 1980

[166] Lowke J J, Morrow R, Haidar J. A simplified unified theory of arcs and their electrodes, Journal of Physics D: Applied Physics, 1997,

[167] Morrow R, Lowke J J. A one-dimensional theory for the electrode sheaths of electric arcs, Journal of Physics D: Applied Physics, 1993, 26(4): 634-42

[168] Lancaster J F. The physics of welding, Paris: Pergamon, 1984

[169] Haddad G N, Farmer A J D. Temperature determinations in a free-burning arc. I. Experimental techniques and results in argon, Journal of Physics D: Applied Physics, 1984, 17: 1189-96

[170] Nakashima H, Utsunomiya A, Fujii N, et al. Hazard of ultraviolet radiation emitted in gas tungsten arc welding ofaluminum alloys, Industrial Health, 2016, 54(2): 149-56

[171] Sliney D H, Benton R E, Cole H M, et al. Transmission of potentially hazardous actinic ultraviolet radiation through fabrics, Applied Industrial Hygiene, 1987, 2(1): 36-44

[172] Lombardi D A, Pannala R, Sorock G S, et al. Welding related occupational eye injuries: a narrative analysis, Injury Prevention Journal of the International Society for Child & Adolescent Injury Prevention, 2005, 11(3): 174-9

[173] Ten K T, Collins M J. A survey of symptoms and eye safety practices among welders, Clinical & Experimental Optometry, 2010, 73(3): 79-85

[174] Tenkate T D. Occupational exposure to ultraviolet radiation: a health risk assessment, Rev Environ Health, 1999, 14(4): 187-209

Acknowledgement

This work was carried out within Laboratoire Plasma et Conversion d'Energie (LAPLACE), Université Paul Sabatier, France and Tianjin Key Laboratory of Advanced Joining Technology, Tianjin University, China.

Fristly, I express my gratitude to defense committeers, who do me the honor of chairing the jury for my thesis. I would also like to express my gratitude for their interest in this study and for the attention they paid to this work.

I express my gratitude to my French supervisor Mr. Yann CRESSAULT, maitre de conférence in Université Paul Sabatier, for his acceptation of me to LAPLACE Laboratory, his great scientific experience, his wise advice, his successful explanations, as well as his encouragement. I would also like to thank my co-supervisor Mr. Philippe TEULE, professor in Université Paul Sabatier, for his expertise, his availability and his aspiration to share his knowledge. The discussions with the two supervisors allowed me to overcome many technical problems that arose during this work, but also to know more about multiple topics too, beyond plasma physics.

I also express my gratitude to Mr. Flavien Valansi, who work in LAPLACE Laboratory, because of his generous guidance in the spectroscopic diagnostics of welding arcs.

I would like to thank my Chinese supervisor, Mr. Huan LI, professor at Tianjin University. During my PhD period, Mr. LI has given me valuable practical guidance for the evolution of my research works and helped me to face the pressures from the work and life. I do not forget the moments that we got along with: he took us to visit enterprises, he shared his experience of life, he displayed his cooking skills …

I also express my sympathy to all the researchers of the group "welding arc physics" led by Mr. Huan LI: Ke YANG, Fusheng YU, Yongqiang LIU and Xiaochen ZHOU for their precious help in experiment; Jianguo Li, Ting XIANG, Yang Du, Peng Wang, Chuanguang LUO, Yuhui ZHANG, Xiaojing DONG for their kindness and supports.

I thank my friends, who support me and encourage me, with whom I spend

pleasant moments. Thanks to Bing XIAO, Peng WANG, Hao WANG, Tianli ZHANG, Dongxiao LI, Ying WANG, Yanyan FENG, Chaobo Guo, Jiajing Pan, Tong Liu…

I express my thoughts to all my family. Their love and support give me the impetus to reach the end of one of my dreams.